CONFOCAL MICROSCOPY STUDY OF COLLOIDAL SEDIMENTATION AND CRYSTALLIZATION

A Dissertation

by

RICHARD EDWARD BECKHAM

Submitted to the Office of Graduate Studies of
Texas A&M University
in partial fulfillment of the requirements for the degree of

DOCTOR OF PHILOSOPHY

May 2008

Major Subject: Chemical Engineering

CONFOCAL MICROSCOPY STUDY OF COLLOIDAL SEDIMENTATION AND CRYSTALLIZATION

A Dissertation

by

RICHARD EDWARD BECKHAM

Submitted to the Office of Graduate Studies of
Texas A&M University
in partial fulfillment of the requirements for the degree of

DOCTOR OF PHILOSOPHY

Approved by:

Chair of Committee,	Michael Bevan
Committee Members,	Zhengdong Cheng
	Kenith Meissner
	James Silas
Head of Department,	Michael Pishko

May 2008

Major Subject: Chemical Engineering

ABSTRACT

Confocal Microscopy Study of Colloidal Sedimentation and Crystallization. (May 2008)

Richard Edward Beckham, B.S., North Carolina State University;

M.S., Northeastern University

Chair of Advisory Committee: Dr. Michael Bevan

Colloidal crystallization in sedimenting systems is an incompletely understood process, where the influence of interparticle forces on the three-dimensional (3-D) microstructure remains to be fully elucidated. This dissertation outlines work that is intended to improve our knowledge of this subject by studying sedimentation equilibrium and phase behavior for electrostatically repulsive systems, as well as the interfacial crystallization of attractive depletion systems. Towards this end, several analytical and experimental tools have been developed to explore the thermodynamic behavior of these systems. For example, the experimental challenges necessitated the development and implementation of the following in this work: (1) core/shell silica particles incorporating molecular fluorophores or semiconductor nanocrystals; (2) modification of silica particle surfaces; (3) the design of specialized sedimentation cells; and (4) the development of a novel fluorescent intensity-based approach to quantifying colloidal sediments. Analysis of the experimental data required the use of the following tools: (1) location of particle centers from images; (2) deconvolution of intensity profiles

using a novel Monte Carlo-type algorithm; and (3) prediction of colloidal phase diagrams using perturbation theory.

On the basis of this work's experimental and simulation data, it is concluded that competing orientations of crystal grains may suppress crystallization at grain boundaries, resulting in a non-uniform depth of the fluid/solid transition. Also, it was demonstrated that the grain size in depletion crystals formed from quantum dot-coated silica particles can be increased by localized annealing with the confocal microscope's laser. Additional findings include the ability of the intensity-based approach to measure interparticle forces in colloidal sediments, as well as the inability to use perturbation theory to predict two-dimensional colloidal fluid/solid transitions. While significant progress has been achieved, work on 3-D imaging of colloidal depletion crystals in a refractive index-match medium is ongoing.

This work improves our understanding of 3-D colloidal crystallization at interfaces, as well as provides new tools for future research. Also, this work demonstrates a potential route for zone refining of colloidal crystals, a technique that may be important in the search for low-defect 3-D arrays that can be used as templates for photonic bandgap materials.

DEDICATION

To Mom and Dad

ACKNOWLEDGEMENTS

I would like to thank my committee chair, Dr. Bevan, and my committee members, Dr. Cheng, Dr. Silas, and Dr. Meissner for their guidance and support throughout the course of this research. Thanks also go to the other members of my research group for their invaluable assistance.

TABLE OF CONTENTS

Page

LIST OF FIGURES

FIGURE Page

LIST OF TABLES

1. INTRODUCTION

1.1 Objectives

This dissertation is concerned with the measurement of colloidal interparticle forces, and the influence of interparticle and particle-wall forces on fluid and crystal microstructure in colloidal sediments. Experimental objectives are focused on (1) measuring interparticle forces in a repulsive colloidal fluid consisting of sub-micron particles; (2) observing the microstructure of the fluid-solid transition above a non-patterned surface [Figure (Fig.) 1.1]; and (3) developing a system that will allow for the three dimensional observation of depletion crystals in equilibrium with a sedimented fluid phase. Central questions related to these objectives include: (1) how do sedimentation conditions influence the crystalline microstructure; and (2) can control over interparticle forces or the particles' thermal energy improve the microstructure? Answering these questions is important in the quest to build large, low-defect equilibrium colloidal crystals.

As part of this research, many of the tools and methods were developed or implemented from scratch. Two important methods that were implemented from scratch by following existing protocols in literature include: the synthesis of Stöber silica particles, including particles labeled with molecular fluorophores; and the use of perturbation theory to calculate colloidal phase diagrams. In both cases, many important details regarding the implementation were either omitted or glossed over in the existing literature, resulting in the expenditure of a considerable amount of time and effort. To

---

This dissertation follows the style of The Journal of Chemical Physics.

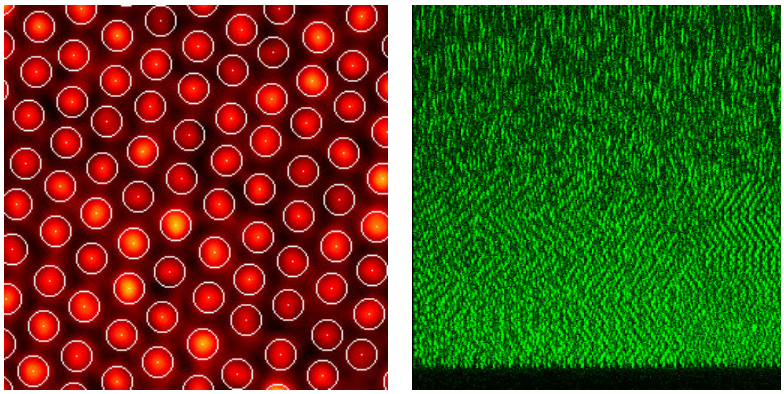

(a) (b)

FIG. 1.1. Examples of colloidal crystals. (a) Particles located through image processing in a colloidal crystal, and (b) vertical scan of a crystallizing sediment of fluorescent sub-micron silica microspheres.

the extent possible, these details are included in this dissertation as an aid to other researchers who may be interested in these methods.

This research also required the improvement of existing methods, and the development of new methods. Improved methods include: (1) location of particle centers from microscopy image data; (2) the use of different fluorophores in silica particles to improve resistance to photobleaching; (3) the functionalization of CdSe/ZnS quantum dots without the formation of clusters; (4) the replacement of ammonia with dodecylamine in Stöber synthesis; and (5) the use of an amine functionalized silane to bind poly(isobutylene) to the surface of silica particles. New methods that were developed include: (1) a Monte Carlo-type algorithm for the deconvolution of fluorescent intensity profiles that exploits knowledge of the profile's behavior to control the impact of random noise on the deconvolution; (2) the binding of quantum dots and other nanoparticles to the surface of silica particles using a peptide bond; (3) growth of large core/shell silica particles in alternative solvents under chilled conditions; (4) a

novel use of fluorescent intensity to quantify the volume fractions at different elevations in colloidal sediment; and (5) the use of a focused laser to excite colloidal particles in depletion crystals thereby locally melting and annealing the crystalline structure. It is hoped that the development of the tools and methods, in addition to the knowledge gained about crystalline microstructure in sediments, will assist in the development of a technique to reliably control the quality of colloidal crystals formed by sedimenting systems.

This dissertation is broken into five major sections: (1) image and data processing; (2) particle synthesis; (3) perturbation theory; (4) sedimentation profiles; and (5) depletion crystals. All of these sections are interconnected – the tools and methods developed in the first three sections are beneficial to the research in the last two sections. However, each section is also relatively independent. As such, each section will contain its own introduction, literature review, theory, experimental, results and discussion, and conclusions subsections. Also, this dissertation introduction section and the main conclusions section are limited, with the reader referred to the individual subsections for greater details into a particular aspect of this research.

1.2 Background and Significance

Colloidal sized components (>1 nanometer (nm)) are present in numerous industrial complex fluids including emulsions, ceramics,[1,2] pastes,[3] coatings,[4] composites,[5] foods, minerals, and pharmaceuticals,[6] but are also essential building blocks in emerging technologies based on nano-structured materials such as protein crystals,[7] magnetic storage devices,[8] chemical and biological sensors,[9] optical switches,[10] and photonics.[11]

Despite the broad range of applications employing colloidal components, current "state-of-the-art" capabilities for predicting and controlling colloidal interactions are severely limited in terms of assembling nano-structured materials and devices on substrates.

Recent work on colloidal photonic materials illustrates both the promise and difficulties associated with using colloidal "building blocks" to assemble interfacial crystals.[12-15] Because uncontrolled drying of monodisperse colloids easily produces polycrystalline structures, many studies have attempted to maximize crystalline domain size using controlled drying approaches.[11,12] Despite initially promising results, colloidal crystals prepared with drying techniques are too disordered for practical use. Alternative approaches to the drying techniques include equilibrium "self assembly" processes when particle configurations are a direct consequence of interparticle forces only. Examples of equilibrium processes that create thermodynamic colloidal crystals include manipulating colloidal forces,[13] and interactions with templates.[18-22]

While much of this research concentrates on crystallization, it is desirable to be able to analyze the fluid phase in addition to the crystalline phase for two reasons. First, all crystals must be formed from fluids; it is therefore absolutely essential to understand the fluid serving as the mother liquor to understand and control the resulting crystal. For example, the structure of the fluid immediately prior to crystallization influences the structure of the crystal (e.g. crystal plain orientation, grain size). Second, analysis of a fluid's barometric behavior allows for the determination of the interparticle forces.[14] While it may be possible to measure these forces independently,[15] the potential exists for a difference in the conditions between the sedimentation experiment and the independent

measurement (solvent evaporation, gas dissolution, etc.).

A number of different methods have been used to probe equilibrium fluid sediments. Many are suitable for analysis of fluids consisting of sub-micron particles, including physical sampling of the sediment,[16] or analysis through x-ray[17] or dynamic light scattering.[18] However, these methods fail to document the fluid's microstructure. On the other hand, the use of fluorescent scanning laser confocal microscopy has been used to document fluid microstructure though image analysis to identify particle center coordinates in three dimensions.[19] Unfortunately, this approach is restricted to large particles [e.g. 2-micron (μm)[19]] due to the slow dynamics required for accurate particle center location in the fluid phase. The use of large particles carries two principle disadvantages. First, polymer particles, such as poly(methyl methacrylate),[19] are required to achieve a suitably light buoyant density.[19,20] This material selection unfortunately limits the selection of the dispersion solvent mixture, as many otherwise suitable components (e.g., ethanol, toluene, dimethylformamide) dissolve PMMA. And second, the combination of slower dynamics due to particle size, and lower buoyant density due to material selection results in sedimentation experiments that can take weeks to equilibrate, as opposed to overnight for 700-nm silica microspheres in a refractive index-matched ethanol/toluene mixture.

In addition to generating a better understanding of the role of interparticle forces on colloidal crystallization and microstructure, this research is significant because it will introduce to the scientific community a new approach for analyzing a sedimented colloidal fluid which is based on its fluorescence intensity variation with elevation, and

is suitable for use with sub-micron colloidal microspheres.

1.3 Summary of Conclusions

In general, this research concludes that the sedimentation conditions do influence the microstructure of crystals formed in colloidal sediments. Specifically, the presence of convection currents in the sedimentation cell was observed to give rise to large crystal domains that were parallel to the cell floor when working with repulsive colloidal particles. These systems were also observed to exhibit a fluid/solid transition at a consistent depth. On the other hand, sedimentation of repulsive colloids in the absence of convection currents resulted in crystal grains that grew perpendicular to the cell floor, and the fluid region extended below the minimum observed crystallization depth at the grain boundaries – resulting in crystal grains with rounded tops.

This research also concluded that localized manipulation of the particles thermal energy can be used to increase crystal grain size. Electrostatic repulsive and depletion attractive crystals were grown using silica particles coated in CdSe/ZnS quantum dots. These crystals were then excited with the focused laser of a confocal microscope. Under excitation, the crystal lattice was observed to expand and then melt. After excitation, the melted zone recrystallized. For depletion crystals, existing grains on the boundary to the melted zone could achieve significant growth before new crystals nucleated, resulting in an increase in size of the grain bordering the melted zone. If properly controlled, this approach should be appropriate for zone refining of colloidal depletion crystals.

Work into three-dimensional (3-D) imaging of colloidal depletion crystals is ongoing. Initial attempts at forming depletion crystals from micron-sized silica particles

failed to crystallize due to excessive electrostatic repulsion, instability, or melting on observation with the confocal microscope. Recently, two-micron silica particles have been sterically stabilized in toluene with a grafted layer of poly(isobutylene), and these particles do not appear to exhibit electrostatic repulsion. This success, combined with the ability to grow large silica shells around small fluorescent cores, suggests that this work is very close to imaging depletion crystals in three dimensions – thereby improving our understanding of how attractive interparticle forces influence the crystalline microstructure.

2. PARTICLE SYNTHESIS

2.1 Introduction

The particles required for this work are highly specialized. They need to: be easily refractive index-matched with common organic solvents; be inert to these same solvents; be sufficiently dense to form a fluid and solid phase in sediments less than ninety microns deep; possess fluorescent cores and non-fluorescent shells that will allow individual particles to be distinguished in a refractive index matched medium in spite of the confocal microscope's point spread function; be amiable to labeling with a variety of molecular and nanocrystalline fluorophores that are resistant to photobleaching; accept a variety of surface functionalities; and be reasonably monodisperse. Stöber silica particles can meet all these requirements, but such highly specific particles could not be located commercially. In fact, only non-fluorescent, bare silica particles were observed to be commercially available. The result is that the particles required for this research had to be synthesized in-house. Unfortunately, the growth of high quality Stöber silica can be a tricky business – especially when additional complicating features such as core/shell anatomies or specific surface chemistries are required. Due to a lack of "institutional knowledge" in this area, combined with a body of literature that often omits or glosses over subtle but extremely important details, a considerable amount of time and effort was invested in implementing (and in some cases developing) from scratch the synthesis methods required to produce good quality, highly specialized Stöber silica particles. It is hoped that this section will not only document the synthesis work that was performed as part of this dissertation, but also provide a convenient guide

to other researchers interested in the synthesis of specialized silica particles.

This section outlines the methods needed to produce these specialized Stöber silica particles, as well as some other particles not directly related to this work, but still potentially useful to other researchers in this field. In this phase of the work, good quality (i.e. low polydispersity and few aggregates) Stöber silica particles were synthesized. Silica particles with fluorescent core/non-fluorescent shell anatomies were also prepared using a non-traditional fluorophore that was more resistant to photobleaching than the rhodamine- and fluorescein-based fluorophores commonly used in silica particle synthesis. In addition, the use of alternate reaction solvents such as acetone and dimethylformamide was explored, sometimes to good success. Further, the use of slow growth conditions, as opposed to the established fast growth conditions, was demonstrated to be an advantageous route for the growth of thick silica shells on small cores. Furthermore, the method in literature for functionalizing quantum dots for water solubility was improved to avoid the formation of undesirable clusters. Also, the use of amines in lieu of ammonia as a catalyst was demonstrated. Finally, the novel use of a peptide bond to attach quantum dots and other nanoparticles to the surface of silica particles without embedding the nanoparticles in a silica layer was developed. These advances allowed for the synthesis of the good quality, specialized particles required for the research discussed in this dissertation.

2.2 Literature Review and Theory

2.2.1 Introduction to Alkyl Orthosilicates

A broad variety of useful silica materials may be synthesized from the hydrolysis and polycondensation of alkyl orthosilicates, including thin films, dispersions of amorphous silica colloidal particles, and porous inorganic networks (gels). Alkyl orthosilicates are a class of compounds with the general structure of $(R\text{-}O\text{-})_4Si$, where R is an alkyl group. Typically, orthosilicates with alkyl groups of one to five carbons are used for synthesis of colloidal silica particles,[21] with the two carbon alkyl orthosilicate [tetraethylorthosilicate (TEOS)] occurring with particular frequency.[21-24]

2.2.2 Alkyl Orthosilicate Synthesis

The synthesis of alkyl orthosilicates is accomplished through the addition of an anhydrous normal alcohol (*n*-alcohol) to silicon tetrachloride ($SiCl_4$).[25] The reaction is executed via the drop wise addition of the alcohol to $SiCl_4$, with the total amount of alcohol added in 10% excess of the stiociometric requirement.[25] A considerable amount of gaseous hydrochloric acid (HCl) is released by the reaction, and the $SiCl_4$ must be chilled to below 0°C during the course of the procedure to control the reaction.[25]

Much of the residual HCl is removed from the alkyl orthosilicate after synthesis by sparging the reaction product with dry nitrogen (N2) gas.[25] However, the subsequent use of calcium oxide (CaO) may be required to minimize the amount of HCl dissolved in the alkyl orthosilicate.[26] Should the alkyl orthosilicate require further purification, vacuum distillation is recommended, as attempts at atmospheric pressure distillation will result in the decomposition of the orthosilicate.[25]

2.2.3 Reaction Overview

The synthesis of silica materials from alkyl orthosilicates begins with the hydrolysis of the orthosilicate to orthosilicic acid (H_4SiO_4), followed by the polycondensation into higher silicic acids ($[SiO_x(OH)_{4-2x}]_n$).[27] The reaction between water and the orthosilicate is catalyzed by either acidic or basic pH levels.[27] Under acidic levels, the hydrogen ion (H^+) attacks an oxygen in the orthosilicate, which leaves the silicon (Si) atom vulnerable to attack from a water molecule.[27] Following, a hydrogen ion from the water molecule and the alkyl group in the form of an alcohol are ejected.[27] Under basic conditions, the hydroxide ion (OH^-) attacks Si atom directly, allowing water to attack the alkyl group, thereby ejecting an alcohol and an new hydroxide ion.[23,27] The removal of the first alkyl group is considered to be the rate limiting step of the complete hydrolysis of an alkyl orthosilicate molecule due to the electron withdrawing nature of the attached hydroxide group.[23] The hydrolysis reaction is exothermic.[28]

2.2.4 Acid Reaction Specifics

The acid-catalyzed reaction is used to create silica gels,[27,29] thin films,[30] and particles.[42-45] Depending on the conditions, particles obtained from a mixture of water, an alkyl orthosilicate, and acid can be either irregularly shaped or spherical.[31] Silica gels and thin films also include significant amounts of an alcohol in the reaction mixtures.[27,29,30] Thin silica films (70 to 125 nm) are obtained from acid-catalyzed silica sols known as spin-on glasses.[30] The silica films are porous,[30] but are nevertheless useful for obtaining the properties of silica on non-silica substrates such as glass

coverslips and silicon wafers[32]. Various formulations exist, and variation of parameters such as the alcohol or alkyl orthosilicate used will influence the final properties such as film thickness and porosity.[30]

By way of example, 90 to 100 nm thick films may be obtained with a silica sol based on ethanol, TEOS, water, and hydrochloric acid.[30] The sol is prepared by adding TEOS, H2O, and HCl in a 1:7:0.04 molar ratio to ethanol.[30] The total amount of ethanol is sufficient so that the TEOS concentration is 4% SiO_2 equivalent.[30] The sol is then ripened at 60°C for 24 hours before being spin-coated onto the substrate. As a final step, the substrate and film are then annealed at 400°C.[30]

Spherical particles can be obtained by adding TEOS to a mixture of water and acetic acid at room temperature and mixing for 30 minutes,[33] using suitable molar percentages.[31] Two to three μm diameter particles are obtained from a TEOS to acetic acid to water molar ratio of 1:4:4,[34] but the particles are polydisperse unless base-catalyzed particles (discussed below) are used as seeds.[33] Larger particles (up to six microns) have been obtained through the use of surfactants, but polydispersity remains an issue.[35] Acid-catalyzed silica particles or shells are able to incorporate some dopants that are not incorporated by base-catalyzed particles, such as erbium ions.[33] The density of acid-catalyzed silica particles have been measured at 2.14 grams/cc.[34]

2.2.5 Base (Stöber) Reaction Specifics

The classic work on silica particles grown by the base-catalyzed hydrolysis and condensation of alkyl orthosilicates was published by Stöber et al.,[21] and particles grown by this method will be referred to as Stöber silica in this dissertation. Stöber used

ammonia as the catalyst, and described the formation of 50-nm to 2-μm spherical particles.[21] The principle advantage of Stöber silica over acid-catalyzed silica particles is that the Stöber process produces monodisperse particles.[21] The alcohols investigated as solvents were methanol, ethanol, *n*-propanol, and *n*-butanol, and the alkyl orthosilicates were tetramethyl orthosilicate, tetraethyl orthosilicate, tetra-*n*-propyl orthosilicate, tetra-*n*-butyl orthosilicate, and tetra-*n*-pentyl orthosilicate.[21] The size varied with reactant concentrations, as well as the selection of the alcohol and orthosilicate.[21] The refractive index of Stöber silica particles has been measured at 1.45.[24]

The reactions were carried out in batch under constant stirring and at room temperature.[21] The alkyl orthosilicates were vacuum distilled before each experiment.[21] Depending on the base concentration required, ammonia was introduced to the batch either as a saturated alcohol solution (prepared by sparging dry nitrogen gas through the alcohol), or as a 14.2 molar (M) ammonium hydroxide solution.[21] The selected reaction time was typically 120 minutes, but Stöber reports that some samples reached their final size in fifteen minutes.[21]

It was observed that using methanol as the solvent produced the fastest reaction and the smallest particles.[21] Conversely, *n*-butanol yielded the slowest reaction and the largest particles.[21] The level of monodispersity decreased with the higher alcohols, but good particles were obtained from a one-to-one mixture of methanol and *n*-butanol.[21] Similar results were also obtained for the alkyl orthosilicates, where the fastest reaction and smallest particles were generated by tetramethyl orthosilicate, while the slowest

reaction (twenty-four hours) and largest particles (2 μm) were generated from tetra-*n*-pentyl orthosilicate.[21] Again, polydispersity increased with particle size, but reasonable results were obtained from tetra-*n*-pentyl orthosilicate in a one-to-three mixture of methanol and *n*-propanol.[21] Particle size also varied with water and ammonia concentration, but was not significantly influenced by the amount of alkyl orthosilicate.[21] Using ethanol as the solvent, particles were limited to less than 1 μm for TEOS, but 1.5 μm sized particles could be obtained using tetra-*n*-pentyl orthosilicate.[21] The tetra-*n*-pentyl orthosilicate would tend to phase separate at elevated concentrations.[21] Particle sizes for the same experimental conditions tended to vary within 30%.[21]

Bogush et al. performed an in-depth study of Stöber synthesis for the ethanol/TEOS/ammonia/water system to determine the effects of reactant concentration on final particle size.[22] The reactions were carried out in batch at room temperature and under constant mixing (the mixer speed did not appear to alter the final particle size).[22] The TEOS was vacuum distilled before use.[22] The ethanol was anhydrous, but it was neither described as denatured nor 200 proof.[22] The reported reactant concentrations were calculated assuming no volume change on mixing, and ranged from 0.1 to 0.5 moles per liter (M) for TEOS, 0.5 to 17.0 M for water, and 0.5 to 3.0 M for the ammonia.[22] The batch reaction volumes were 100 mL to four L (the batch volume did not appear to alter the final particle size).[22] The reaction time ranged from three to eight hours.[22] Under this range of conditions, particles from less than 50 nm to approximately 800 nm were obtained.[22] The solid density of the particles was measured at 2.04 to 2.10 gm/cc,[22] close to the value of 2.03 obtained by others.[24] But due to the porous nature of

the particles, the bulk particle density was estimated at 1.78 to 1.86 gm/cc.[22] The empirical relationship between reactant concentration and final particle diameter (d) in nm for the range of conditions tested was reported as[22]

$$d = A[H_2O]^2 \exp\left(-B[H_2O]^{1/2}\right) \tag{2.1}$$

$$A = [TEOS]^{1/2}\left(82 + 151[NH_3] + 1200[NH_3]^2 - 366[NH_3]^3\right) \tag{2.2}$$

$$B = 1.05 + 0.523[NH_3] - 0.128[NH_3]^2 \tag{2.3}$$

The maximum particle size was obtained using a water concentration of seven molar.[22] The reaction time for intermediate conditions at room temperature was approximately three hours, and decreased with increased water concentrations.[22] However, several hours were sometimes required when synthesizing the smaller particles.[22] The final particle size increased with a reduction in the reaction temperature.[22]

The distillation of the TEOS was found to be an essential step to ensure the production of monodisperse particles.[22] The standard deviation of the polydispersity varied between fifteen percent for smaller particles to less than five percent for larger particles.[22] Attempts at the larger sizes carried the risk of secondary nucleation in the seeded growth experiments (resulting in a bimodal particle size distribution) or polydisperse samples in the batch experiments.[22] Higher ammonia concentrations (two to three molar) also tended to result in polydisperse samples, as well as flocculation of the sample.[22] Others have also noted that high ammonia concentrations destroy stability.[24]

The exact mechanism of Stöber silica particle formation has been a topic of debate.[28] It is known that in the presence of hydroxide ions, the alkyl orthosilicate reacts with water to silicic acid that, under appropriate conditions, ultimately polymerizes and condenses to form amorphous Stöber silica particles.[28] However, it is not immediately clear if the silicic acid and its higher derivatives directly diffuse to the growing particle surface, or if the silicic acid nucleates into sub-particles that then diffuse to the particle surface and aggregate due to van der Waals forces.[22,28,36] Giesche investigated the mechanism, and concluded that both paths were likely present, with the nucleation-aggregation path dominating in the initial phases of the reaction, and the monomer addition path increasing in prominence as the particle growth approaches completion.[28] These findings are consistent with work by other researchers who observed only $Si(OEt)_3(OH)$ as an intermediate, and noted the rough surface of Stöber silica particles.[36]

In the study, Giesche focused on the kinetics of the TEOS/ethanol/ammonia/water system using light scattering, TEM and gas adsorption. As with Stober et al.[21] and Bogush et al.,[22] Giesche vacuum distilled the TEOS prior to use.[28] Unlike the others, however, the batch contents were stirred for only the first fifteen second.[28] To stop particle growth at desired points in the reaction, the silica was end-capped using trimethylchlorosilate.[28] The concentrations ranged from 0.1 to 0.4 M for TEOS, 0.8 to 4.2 M for NH_3, and 3.0 to 13.0 for H_2O.[28] The reaction temperature varied from 20°C to 60°C.[28]

The maximum size observed at 20°C was 700 nm.[28] Particle size increased with higher levels of NH_3 and lower temperatures.[28] The maximum particle size was

obtained from an 8 M water concentration, but the only concentrations investigated were 3, 8, and 13 M.[28] The particles were porous with a pore size of approximately 0.3 nm, and exhibited a slow release of ammonia over time. The level of porosity was estimated at 25 to 30%.[28]

During the reaction, the monomer and dimer forms of silicic acid were the predominant intermediates, representing 70-90% and 10-25% respectively of the silicic acid present.[28] The trimer and higher silicic acids represented <2% and <1%, respectively.[28] The first-order hydrolysis of TEOS was determined to be the rate-limiting step.[28] Interestingly, an induction period prior to particle formation was observed that varied inversely with reaction rate.[28] Also, increases in ionic strength enlarge the final particle size, but have no effect on the reaction rate.[28] Giesche notes SAXS data obtained by others that hint at a silica nuclei critical size of about 1 nm, and theoretical calculations that point a critical size of 1-2 nm.[28] It is postulated that colloidal stability and aggregation rate determine the final particle size.[28]

It should be commented that while the above experiments were performed in batch, good quality Stöber silica has been produced in a microfluidic reactor. It is worth noting that although the TEOS was not vacuum distilled in this particular study, monodisperse particles were still obtained in some cases.[37]

Finally, it is possible to use non-silica particles, such as gold or polystyrene, as seeds in Stöber synthesis if the non-silica particles are first coated with a layer of poly(vinylpyrrolidone).[38]

2.2.6 Large Stöber Silica

A significant amount of effort has been invested in exceeding the 700-800 nm particle diameter limit encountered in the ethanol/TEOS/ammonia/water system. One strategy has already been mentioned: the use of alternate alkyl orthosilicates or alcohols.[21] However, some researchers were unable to obtain particles in excess of one micrometer using alternate alcohols.[39] To other strategies are to chill the reaction mixture,[40] or increase the ionic strength.[41] In one study, 1.87 μm Stöber was obtained by carrying out the synthesis at -20°C.[40]

Bogush et al. conducted semi-batch seeded growth experiments.[22] Routine additions of TEOS and water (in a one-to-two molar ratio) to the batch system were used to grow particles larger than 800 nm.[22] As much as two times the original amount of TEOS would be added once every eight hours, for a total of up to ten additions.[22] The reaction temperature used for the seeded growth was also varied, ranging from room temperature to 55ºC.[22]

Similar to the semi-batch addition of TEOS, Giesche implemented a procedure based on the continuous injection of TEOS into a dispersion of seed particles to obtain a final particle size of 3.6 μm with a high degree of monodispersity and smooth surfaces.[26] In addition to vacuum distilling the TEOS, Giesche also treated the TEOS with CaO to remove any residual HCl and avoid unnecessarily increasing the ionic strength of the reaction mixture as more and more TEOS is added.[26] To avoid contamination of the TEOS by water and ammonia during the continuous injection, the TEOS is added through free-falling drops, and the inlet is blanketed with a continuous stream of dry

air.[26] The shell growth was conducted at 40°C using 17.5 nm Stöber silica seeds. Secondary nucleation was observed if the TEOS was metered in too quickly.[26] Also, there existed the potential for silicic acid inhomogeneities if the ammonia or temperature was too high.[26] Recommendations for the continuous growth phase include limiting the ammonia concentration to 0.1 to 1.0 molar, and the maximum silicon dioxide equivalent to 1 molar (0.5 to 0.8 preferred).[26] The maximum growth rate should be 40 nm per hour.[26]

Particle sizes obtained from the Stöber method have also been enhanced by the use of surfactants such as sodium dodecylsulfate (SDS)[42,43] and cetyl trimethyl ammonium bromide (CTAB).[44] In one example, reactant concentrations that normally result in 350 nm particles yielded 0.5 to 1.0 μm particles in the presence of seven to fourteen millimolar SDS.[42] In another study, 0.25 mass percent SDS generated 1.2 μm particles.[42,43] Further, CTAB at various concentrations has been used to produce good quality particles in excess of 1 μm by the Stöber method; in addition to hollow shells, hollow shells filled with smaller particles, and irregular particles.[44] Due to the rough surface of particles obtained from SDS, it has been proposed that the mechanism follows the aggregation model.[42] The large sizes obtained by surfactant addition are believed to be due to accelerated nucleation due to surfactant templating[43] and greater nuclei aggregation due to the increase in ionic strength (provided the surfactant is ionic).[44] In these cited surfactant Stöber studies, the TEOS appears to have been used without purification.[54-56]

2.2.7 Reverse Emulsion Silica

In the studies present thus far for both the acid and base catalyzed reactions, the formation of the particles relied on either homogeneous nucleation of silica, or the use of seed particles, followed by growth of a silica shell. But it is also possible to obtain particles through the use of reverse emulsions where microscopic water droplets are dispersed in an oil phase, and act as templates for particle growth.[51,57-61] Typically, surfactants are used to stabilize the water droplets in the oil phase, and perhaps the TEOS in the water droplets.[45-47] The reaction can be either base[46] or acid[45] catalyzed. Large sizes (one to forty micrometers) are readily obtainable,[39,45,46,48] but the results are almost invariably polydisperse.[39,45,48] Depending on the conditions, a variety of morphologies are generated, including hollow shells.[47]

2.2.8 Incorporation of Molecular Fluorophores

There exist two approaches to labeling Stöber silica particles with fluorescent molecular fluorophores. The first approach utilizes a positive cationic fluorophore such as dichloro tris(1,10-phenanathroline)ruthenium(II) hydrate that will adsorb to the native negative charge on silica, and can thereby be incorporated into the silica matrix as the particle is growing.[49] The second approach covalently binds the dye to a silane, and the silane/dye molecule can then be added to existing particles to form a fluorescent layer, or added during particle synthesis to form fluorescent particles or fluorescent shells.[24,50] In two specific applications of this approach, (3-aminopropyl) triethoxysilane (APES) was mixed with fluorescein isothiocyanate (FITC)[24] or rhodamine isothiocyanate (RITC).[50] In both applications, the thiocyanate reacts with the amine group on the silane.[24,50]

Typically, anhydrous ethanol is the solvent, and the thiocyanate dye is allowed to react with APES under a nitrogen blanket for twelve hours.[24] It has been observed that the thiocyanate dye will not incorporate into the silica matrix if not first reacted with APES.[24] Both the ruthenium and thiocyanate labeled particles have been imaged in confocal scanning laser microscopy (CSLM).[49,50]

2.2.9 Surface Functionalization

It is possible to expand the range of applications of Stöber silica particles through functionalization of the particle surface. While a variety of modifications are possible, they all rely on forming covalent bonds with the –OH groups on the particle surface. One modification has already been mentioned: the coating of the particles with a molecular fluorescent fluorophore. This section will address another common modification: imparting a certain degree of hydrophobicity to the particles, thereby allowing them to easily disperse into a variety of polar and non-polar organic solvents. This is an important application as non-polar solvents such as toluene will destabilize untreated Stöber silica particles.[51] Depending on the solvents and desired particle interactions, modification of the silica surface can take three forms: esterification with 1-octadecanol, reaction with a variety of silanes, or grafting of long polymer chains.

2.2.9.1 Octadecanol

The first method to be discussed is the coating of the particle surface with 1-octadecanol (also known as stearyl alcohol), where the alcohol group esterifies with the –OH group on the particle surface.[52] Silica particles treated in this manner are exceedingly hydrophobic, and will readily disperse in organic solvents such as

chloroform and toluene.[52] Initially, the particles are dispersed in a greater than 96% solution of ethanol.[52] After any water in the system has been distilled off, solid 1-octadecanol is added and melted/dissolved.[52] Following, the ethanol is boiled off and the particles esterified with the 1-octadecanol at 180-200ºC under a nitrogen blanket for two hours.[52] The remaining 1-octadecanol is then dissolved in an organic solvent such as chloroform, and the particles separated and further cleaned.[52] The 1-octadecanol coating is approximately two nanometers thick.[53]

2.2.9.2 Silanes

There exist a variety of silanes that have been used to coat silica particles. Silanes have the structure $R_{4-n}SiX_n$, where R is the non-hydrolyzable functional group that will impart the desired properties, and X is an alkyl oxide that can be hydrolyzed into an alcohol (similar to the hydrolyzation of the alkyl oxides on an alkyl orthosilicates), thus leaving the silicon atom available to bond with the particle's silica matrix.[54] APES, mentioned above for covalent bonding of molecular fluorophores to silica, will produce a positive surface charge (the native charge on silica is negative) if the amine group is left unreacted.[55] Coating silica particles with γ-methacryloxypropyltrimethoxysilane (TPM) will also provide a charged surface, but the particles will disperse in both non-polar solvents such as toluene, as well as weakly polar solvents such as tetrahydrofuran that are too polar for 1-octadecanol coated particles.[51,53,54] Finally, silanes such as octadecyltrimethoxysilane (OTMS) will attach octadecyl chains to the particle surface, as did the esterification of 1-octadecanol.[56] When dispersed in organic solvents, it has been determined that silane-coated silica

particles will not swell or shrink, and the silanes remain bound to the particle surface.[51] To ensure the stability of the silica particles, silanization may need to be carried out under ultrasonication or in the presence of a non-ionic surfactant such as pluronic.[56]

Philipse et al. describe in detail a method for coating silica particles with TPM.[54] First, the silane is added to the particles in ethanol, water, and ammonia.[54] Next, the silane is allowed to react for thirty minutes.[54] Following, the ethanol content is increased to greater than 96% and the water distilled off over two hours.[54] The particles are then separated from the ammonia and unreacted silane by sedimentation and redispersion in ethanol.[54] To ensure particle stability, it is recommended that forty to one hundred nanometer-sized particle not be centrifuged above 3000 to 4000 revolutions per minute (rpm) during the sedimentation step.[54] The volume requiring centrifugation may be reduced through vacuum distillation at room temperature.[54]

2.2.9.3 Polymer Grafting

Coating silica particles with 1-octadecanol or simple silanes will allow for particles to be dispersed in non-polar solvents and, depending on the functional groups, can provide charge stability. However, to achieve steric stability, polymer chains must be grafted to the silica surface. There exist three strategies to accomplish this task using silanes. The first strategy is to grow a polymer chain on the silica surface by first coating the silica particles with a silane whose functional group has a double-bonded carbon at the end [e.g., vinyltrimethoxysilane (H_2C=$CHSi(OMe)_3$) or methacryloxypropyltrimethoxysilane (H_2C=$CMeCO_2(CH_2)_3Si(OMe)_3$)], dispersing the particles in an organic solvent, and then initiating polymerization of a monomer such as

methylmethacrylate (MMA) or dimethyl terminated silicones.[57] The second approach is to react an epoxy-terminated silane [(3-glycidoxypropyl) trimethoxysilane] with a carboxyl-terminal polymer (12-hydroxy stearic acid), and then mix the silanized polymer with a dispersion of silica particles.[53,58] The third technique is to initiate polymerization of a monomer or monomers such as MMA or styrene and sec-butyl lithium, add a silane such as 3-mercaptopropyltrimethoxysilane or methyltrichlorosilane to the living polymer, and then add the silanized polymer to silica particles.[59,60]

It is also possible to graft polymer chains onto the silica surface without the use of silanes. One method is to bind poly(isobutylene) (PIB) to silica.[61] The thickness of the stabilizing layer will depend on the molecular weight of the initial polymer, ranging from four to five nanometers for PIB with a molecular weight of 1,300, to thirty to fifty nanometers for PIB with a molecular weight of 13,000.[53] Particles with steric stabilizing layers of PIB have been observed to be more stable in organic solvents than particles with only a coating of 1-octadecanol, with the stability increasing with the thickness of the stabilizing layer.[53]

To stabilize silica particle, the PIB must be modified to chemically react with the silica matrix.[62] The first step is to convert the PIB to poly(isobutenyl) succinic anhydride (PSA) by reacting the PIB with maleic anhydride.[62] The maleic anhydride is added to the PIB in a 2:1 molar ratio, and the reaction is carried out at 235°C under a nitrogen blanket for nine hours.[62] The resulting product is golden in color.[62] The PSA is then dissolved in heptanes, passed through a 0.8 mm filter, and vacuum distilled at 140°C to drive off any the heptanes and any remaining maleic anhydride.[62] The next

step is to attach an amine to the succinic groups on the PSA.[62] Tetraethylenepentamine (TEPA) and PSA are mixed together in a 1:1 molar ratio, using toluene as the solvent.[62] The mixture is then refluxed to drive the reaction and remove water, which is a reaction byproduct.[62] The mixture is then vacuum distilled at 190°C for five hours to remove the toluene and unreacted TEPA, leaving only the modified PIB.[62]

To bind the modified PIB to silica, it is first dissolved either in toluene[62] or tetrahydrofuran,[63] and then mixed with the silica particles dispersed in anhydrous ethanol.[62,63] To ensure the stability of both the particles and the dissolved modified PIB, the polymer needs to be limited to 0.5 to 1.0% w/v in the solvent and the ethanol to less than 15% in the mixture when using toluene;[62] and polymer needs to be limited to less than 0.5% w/v in the solvent and the ethanol to less than 35% v/v in the mixture when using tetrahydrofuran.[63] From this point, the ethanol (and tetrahydrofuran if present) is distilled off, with the difference in volume being made up for by the addition of toluene.[62,63] The PIB-coated silica particles are then removed from the excess modified PIB by repeated sedimentation and redispersion in toluene.[63] Particles modified in this manner have been observed to be uncharged and sterically stable in toluene.[51,63]

2.2.10 Incorporation of Nanoparticles

Two methods have been identified in literature for coating silica particles with fluorescent semiconductor nanocrystals known as quantum dots, thereby provided an alternative to organic fluorophores which have a lower quantum yield and are more susceptible to photobleaching.[64] The first method is based on coating the silica particles with 3-aminopropyltrimethoxysilane (APMS), coating the quantum dots with PVP to

stabilize them in alcohols and render them susceptible to a silica coating, allowing the quantum dots to adsorb onto the APMS coated silica, and finally encasing the quantum dot layer with a silica shell.[65] This method can also be used to embed gold nanoparticles.[65] The method begins with either 5 g/L of quantum dots in chloroform or 0.1 g/L of gold nanoparticles in water.[65] The quantum dots or gold particles are then dispersed into either a butanol (for dots) or water (for gold) solution of 27.1 grams of PVP-10 per liter.[65] The quantity of nanoparticles added should be sufficient for sixty PVP molecules per square nanometer of nanoparticles surface.[65] The PVP is then allowed to adsorb for twenty-four hours.[65] The PVP-coated nanoparticles are then mixed with 0.5 g/L of APMS-coated silica particles in ethanol such that there are enough nanoparticles for 2.5 monolayers on the silica.[65] After adsorption, the silica is then centrifuged to separate out the excess nanoparticles, and a silica shell is then grown on the particles using TEOS and ammonia.[65]

An alternate method is to first coat the quantum dots with 5-amino-1-pentanol (AP) and APMS, and then grow a silica shell onto silica particles in the presence of hydroxypropyl cellulose (HPC) and the modified quantum dots, thereby embedding both the HPC and quantum dots in the shell.[66] The quantum dots are modified by first drying quantum dots precipitated from butanol/hexane, and then redispersing 135 mg in 1000 mg of anhydrous ethanol and reacting them with 150 mg of APMS and 60 mg of AP under a nitrogen blanket for 30 minutes at 40°C.[66] 10 μL of the modified quantum dots in ethanol are then mixed with 30 mg of silca particles and 16 mg of HCP in 10 mL of ethanol.[66] 50 μL of water, 50 μL of 28 wt% ammonia in water, and 0.15 mL of TEOS

are then added to grow a silica shell at 75°C for 4 hours.[66]

2.2.11 Functionalization of Nanoparticles

It is possible to functionalize both CdSe-ZnS quantum dots and gold nanoparticles with carboxylic acid groups. This functionalization is accomplished with either mercaptoacetic acid (MAA)[67] or dihydrolipoic acid (DHLA).[68] The MAA is inexpensive, but offers only one sulfur atom per molecule for bonding.[67] On the other hand, DHLA is more costly than MAA, but offers two sulfur atoms per molecule for bonding.[69] Without any additional treatment (such as the adsorption of PVP), it is possible to grow a silica shell from TEOS directly onto nanoparticles coated with either MAA[30] or DHLA.

The carboxylic acid functionalization of gold nanoparticles may be accomplished by one of two methods. The first method is the aqueous reduction of $HAuCl_4$ by sodium borohydride ($NaBH_4$) in the presence of DHLA.[70] As the gold nanoparticles are formed, they are coated and stabilized by the DHLA.[70] The second method begins with the aqueous reduction of $KAuCl_4$ and stabilization of the subsequent gold nanoparticles by sodium citrate.[61] The aqueous dispersion of citrate-stabilized gold nanoparticles are then mixed with MAA in a 500:1 volume ratio, and the MAA is allowed to adsorb onto the gold nanoparticles for four days under constant stirring at room temperature.[61]

The functionalization of quantum dots by MAA begins with a dispersion of CdSe-ZnS dots in chloroform.[67,71,72] MAA is then added directly to the dispersion, and reacted for two hours.[67,72] In some cases, the mixture is also sonicated at 80°C.[71] The functionalized quantum dots are then purified either by crashing them with methanol and

resuspending them in ethanol,[71] or extracting them in an aqueous phase followed by centrifugation and resuspension.[72]

2.2.12 Incorporation of Quantum Dots into Polystyrene Particles

In addition to silica particles, it is also possible to embed quantum dots into polystyrene particles.[73] First, the polystyrene particles are dispersed either in propanol or butanol.[73] Next, a dispersion of quantum dots in chloroform is added to the polystyrene particles in the alcohol.[73] The chloroform swells the polystyrene, and the quantum dots diffuse into the outer layers of the particles.[73] The level of penetration of the quantum dots into the polystyrene particles depends on both the degree of swelling and the level of crosslinking present in the particles.[73] Some crosslinked particles may require the addition of as much as 60% v/v chloroform to the alcohol to achieve sufficient swelling for quantum dot infusion.[73]

It is also possible to add the chloroform/quantum dot dispersion to styrene before the polystyrene particles are formed through emulsion polymerization.[74] However, the quantum dots segregate within polystyrene particles synthesized in this manner.[74]

2.3 Procedures

2.3.1 Materials and Miscellaneous Equipment Overview

The CdSe-ZnS quantum dots were obtained from or synthesized with the assistance of Dr. Kenith Meissner and his research group. Poly(isobutylene) and F-108 pluronic were supplied as an industrial sample from BASF. Succinimidyl 6-(*N*-(7-nitrobenz-2-oxa-1,3-diazol-4-yl)amino) hexanoate (NBD-X SE) was obtained from Invitrogen. 200 proof ethanol was purchased from Aaper Alcohol. All other reagents

were purchased from research chemical supply companies such as Fisher Scientific and Sigma-Alrich. With the exception of organic solvents used for washing, the chemicals were reagent grade and used without further purification, unless otherwise noted below in the procedures.

Particles were sized using a ZetaPALS dynamic light scattering instrument by Brookaven Instruments Corportation. Confocal images were captured using a LSM 5 Pascal scanner attached to an Axiovert 200M MAT microscopy equipped with a Plan-APOCHROMAT 100x/1,4 oil immersion objective, all by Zeiss.

2.3.2 Alkyl Orthosilicates Synthesis and Purification

Reagent-grade TEOS was obtained from laboratory chemical vendors. Tetrapentyl orthosilicate was synthesized from reagent-grade materials by mixing *n*-pentanol with silicon tetrachloride according to the procedure described in literature.[25] Specifically, a bath of 50/50 v/v commercially available ethylene glycol and water was continuously cooled by a Julabo F 25 chiller/heater through insulated, flexible polyvinyl chloride (PVC) tubing and a copper coil to approximately -10°C. The temperature was monitored using a mercury thermometer. This bath was placed on a Fisher Scientific Isotemp stirring plate in a fume hood, and in the bath was positioned a 3-necked, 1000-mL round bottom flask with a Teflon stirring rod. One of the side necks was used to inject dry nitrogen gas through a Pasteur pipette from flexible PVC tubing connected to an adjustable pressure regulator and a compressed gas cylinder. The annular region between the pipette and neck was sealed using a silicone rubber stopper, and the tip of the pipette was positioned so that nitrogen gas would sparge through the contents of the

flask without interfering with the magnetic stir bar. Attached to the middle neck was a reflux condenser chilled by cold water with the gas-phase effluent directed to a beaker of water by a flexible PVC tube. The remaining neck contained a second silicone rubber stopper through which was passed a section of small diameter Teflon tubing. The tubing was connected to a plastic syringe and a New Era Pump Systems syringe pump contained the desired normal alcohol, and the end was positioned such that it would be above any contents of the flask.

To begin the synthesis, the flask and condenser were first flushed with dry nitrogen gas through the Pasteur pipette to remove any water vapor that may have been present. Next, while maintaining the flow of nitrogen, the silicone rubber stopper with the Teflon tubing was temporarily removed and the desired amount of silicon tetrachloride was introduced to the flask using a plastic syringe and long stainless steel septum needle (both previously flushed with nitrogen). At this point, stirring began at a speed just sufficient to induce vortexing of the liquid. After allowing the silicon tetrachloride to chill for about fifteen minutes, the *n*-pentanol was slowly (drop wise) metered into the flask. The rate was adjusted qualitatively so that the bubbling due to HCl production was not excessive. After the addition of the *n*-pentanol was complete, the sparging of the nitrogen gas through the flask contents was continued under stirred and chilled conditions from another hour to further reduce the amount of HCl remaining dissolved in the product.

Initially, reagent-grade TEOS was used as received. Later, however, all alkyl orthosilicates – whether synthesized or purchased – were purified by treatment with

laboratory-grade quick lime (CaO), followed by vacuum distillation in the presence of calcium carbonate ($CaCO_3$) boiling chips. First, the desired amount of the alkyl orthosilicate was placed in a beaker, and then enough CaO was added to create a turbid dispersion. After allowing the majority of the CaO to settle for a few minutes, the supernatant was transferred to a boiling flask containing approximately ten to twenty marble boiling chips. While it was attempted to retain a majority of the CaO in the beaker, some carry-over into the boiling flask was acceptable as any such CaO would remain in the distillation bottoms. A Teflon-coated magnetic stirring bar would be added to the boiling flask too, as its aggregation was observed to disturb the boiling chips and thereby help prevent bumping of the alkyl orthosilicate.

The boiling flask was next placed on a Fisher Scientific Isotemp stirring hot plate, and connected to the condensation arm and collection flask. The collection flask, in turn, was connected by flexible tubing to the vent of a vacuum oven. To conduct the distillation, the oven and the distillation system would be evacuated, and the stirrer and heater turned on. The temperature setting of the heater would be incrementally adjusted until gentle boiling of alkyl orthosilicate was observed. After completion of the distillation, the vacuum would be broken using dry nitrogen gas to minimize the potential for fire or explosion. The purified alkyl orthosilicate would then be stored under refrigeration and a nitrogen blanket to avoid moisture contamination.

2.3.3 Standard Stöber Reaction

A variety of containers were used as batch reactors for the synthesis of Stöber silica particles, including four-milliliter Teflon-capped glass vials, twenty- and forty-

milliliter Volatile Organic Analytes (VOA) environmental sample vial, and fifty- and 500-milliliter round flasks. The contents of the reactors were fluidized either through the use of a Barnstead/Lab-Line Lab Rotator shaker (four milliliter glass vials), or appropriately-sized Teflon-coated magnetic stirring bars and a Fisher Scientific Isotemp stirring plates (VOA vials and flasks). For most reactions, this fluidization was continuous. On a few occasions however, the contents of a glass vial would be mixed for only about fifteen seconds at the beginning of the reaction. All reactors were sealed using a Teflon-lined cap, silicone rubber stopper, or parafilm. All glassware was pre-cleaned by soaking in a 50/50 v/v mix of one molar potassium hydroxide (KOH) in water and isopropanol for at least one hour. The glassware was then thoroughly rinsed with deionized (DI) water, and backfilled with a 90/10 v/v mixture of DI water and an alcohol (either methanol or denatured ethanol) for storage. Immediately before use, the glassware would be rinsed again with DI water, followed by an alcohol (again, either methanol or denatured ethanol), and then dried with a stream of pressurized air.

To conduct a Stöber synthesis reaction, DI water, the desired solvent (typically a normal alcohol, acetone, or mixture of these solvents), and the desired base (aqueous ammonia or an amine) would be combined in the reactor. If the experiment was a fluorescent, seeded growth, or surfactant experiment; the fluorophore, seeds, or surfactant would be dispersed in the desired solvent to form a stock solution, and a portion of that stock solution added to the reactor at this time, too. The total synthesis volume was typically about one half of the reactor volume to allow for dilution of the contents after the reaction was complete. Alkyl orthosilicates were purified as described

above. In the beginning, DI water, the solvent, and the desired base would be used as supplied. Later, the DI water and the solvent were filtered through Whatman Anotop 25 0.02 μm filters. A majority of the reactions were conducted at room temperature. For chilled or heated experiments, a bath of 50/50 v/v ethylene glycol and water was either chilled or heated using a Julabo F 25 chiller/heater through insulated, flexible PVC tubing and a copper coil. The bath was placed on a Fisher Scientific Isotemp stirring plate to allow for agitation of the batch reactor contents with a magnetic stirring bar. The ethylene glycol was circulated around the bath container and copper coil using a Labortechnik IKA RW 16 Basic variable speed stirrer and Teflon impeller. The bath temperature was monitored using a K-type thermocouple and Omega DP460 readout.

The reaction would be initiated with the addition of the alkyl orthosilicate, with the goal to accomplish the addition in a single step. As such, if the quantity of the alkyl orthosilicate was one milliliter or less, it could be added with a single injection from a pipette, and was used at full strength. If the required quantity exceeded one milliliter, it would be diluted by at least fifty percent with the desired solvent in a beaker, and then poured into the reactor. The initial volume of the desired solvent added to the reactor would be reduced by the amount used to dilute the alkyl orthosilicate. The reaction time was varied based on the reaction conditions. Fast reactions such as those of the methanol/TEOS or ethanol/TEOS systems at room temperature would be allowed to react for two to four hours. Slower reactions, such as those conducted at chilled temperatures, would usually be allowed to react for at least twenty-four hours. Subsequent alkyl orthosilicate additions for shell growth were based on an assumed

reaction time of two hours. Normally, these additions would be one quarter of the initial alkyl orthosilicate volume, and would be added every half hour after the first two hours.

After the reaction was considered complete, the contents would be diluted to fill the remaining half of the reactor volume with an alcohol. This action reduced the ionic strength of the mixture, thereby increasing the stability of the synthesized particles. For reaction mixtures of unusually high ionic strength, synthesis reactions of particular importance, or particles in which a considerable amount of time or effort had been invested; the reaction mixture would be transferred to a larger container and diluted with a sufficient amount of an alcohol to reduce the ionic strength to below twenty millimolar. In either case, the particles were then separated by gravity sedimentation. Methanol was the preferred dilutent due to its inexpensive price compared to other alcohols, as well as its lower density that sped the sedimentation process. However, other anhydrous alcohols were also used if methanol was in limited supply, or if a subsequent step would require the use of another alcohol (such as *n*-butanol for the quantum dot coatings discussed below). After at least two cycles of sedimentation and redispersion, the particles would be stored in alcohol.

2.3.4 Octadecanol Coating

To accomplish the coating of Stober silica particles with 1-octadecanol, the procedure in literature[52] was followed. The particles, whether synthesized or purchased from a commercial vendor, were sedimented and redistributed at least three times in 200-proof ethanol to remove a majority of the water. Whenever possible, gravity sedimentation was used. However, small particles (less than 300-nm) would often

necessitate the use of the centrifuge to accomplish the sedimentation in a timely manner. Next, the particles were transferred to the reaction vessel – usually a 100-mL conical bottomed flask – and further diluted with 200-proof ethanol to about sixty milliliters. The exact dilution ration was not considered critical, provided it was at least ten times as dilute as either the synthesis or commercial stock of particles. Next, enough solid 1-octadecanol pellets were added to the reactor to bring the total volume up to about 100 mL. While some of the 1-octadecanol likely dissolved into the ethanol, a majority of the pellets remained undissolved at room temperature. A small Teflon-coated stirring bar was usually added to the reactor at this time.

The reaction vessel was then placed in a silicone oil bath on a Fisher Scientific Isotemp stirring hot plate and the oil heated to about 75ºC. The oil bath temperature was monitored using a K-type thermocouple and Omega DP460 readout. Before the heating began, a gentle stream of dry nitrogen gas was directed into the reactor head space using a Pasteur pipette connected to a nitrogen cylinder and adjustable pressure regulator by flexible PVC tubing. As the ethanol warmed, the remaining 1-octadecanol pellets would dissolve. At this point, the tip of the Pasteur pipette would be lowered to the bottom of the reactor to sparge the entire contents of the reactor. By using the nitrogen gas to remove the ethanol, bumping was avoided without the use of boiling chips that would potentially contaminate the sample with calcium carbonate particulates. The evaporative cooling due to ethanol removal by the nitrogen gas lowered the temperature of the oil bath, so the amount of ethanol removal could be monitored by observing both the oil bath temperature and the remaining volume in the reactor. After the oil bath reached

about 85ºC, it was felt that bumping would no longer be an issue as a sufficient amount of ethanol had been removed from the molten 1-octadecanol. At this point, the Pasteur pipette was raised up into the head space of the reactor. Nitrogen flow was continued until bubbling was no longer observed in the reactor contents, at which point the Pasteur pipette was removed and the top of the reactor sealed with a silicone rubber stopper.

The oil bath was then increased to a temperature of about 200ºC, and maintained at this point for at least two hours. Afterwards, the contents were allow to cool to either the boiling point of ethanol or chloroform (depending on the solvent that was going to be used to extract the 1-octadecanol); after which, the solvent was then added. In some cases, crystals of 1-octadecanol would form on cooling in spite of the presence of a solvent. When this happened, the solvent was extracted and placed in a larger container, the remaining crystals dissolved in fresh solvent, and the new solution also transferred to the large container. Separation of the particles from the unreacted 1-octadecanol was accomplished through repeated cycles of sedimentation and redispersion in the solvent. As before, gravity sedimentation was used whenever the particle diameter was sufficient to allow for timely completion of the sedimentation process. The purified 1-octadecanol coated particles were then stored in either anhydrous, 200-proof ethanol, toluene, or chloroform.

2.3.5 Silane Coating

Two silanes were used to coat silica particles: APMS for amine functionality and OTMS for hydrophobic properties similar to 1-octadecanol coated particles. In both cases, the procedures were the same. To coat commercial silica particles, they were first

cleaned by a 10% (v/v) boiling mixture of nitric acid and water for ten minutes; followed by sedimentation and redispersion into DI water, and subsequent soaking for at least one hour to leach out the nitric acid that may have diffused into the particles' pours. Synthesized silica particles did not require cleaning in this manner. To remove a majority of the water and other alcohols present in the dispersion, the particles were sedimented and redisbursed in an anhydrous alcohol three times. Initially, 200-proof ethanol was used, but later *n*-butanol was preferred for its ability to support hydrophobic particles.[75] As an example of the procedure, particles would be disbursed in twenty-seven milliliters of butanol in a clean forty-milliliter VOA vial. To this vial, 15 mL of triethylamine would be added to act as a catalyst for the silane hydration reaction. Next, 75 mL of the silane would be added to three milliliters of butanol. The VOA vial containing the particles was then place in a Branson 1510 ultrasound bath, and while under ultrasound, the silane in the amine was added to the particles. The VOA vial was then sealed with a Teflon-lined cap, and the sonication continued for at least eight hours. Afterwards, the particles were allowed to react with the silane for another sixteen hours. Finally, the particles were separated from the unreacted silane by three rounds of sedimentation and redispersion in butanol.

2.3.6 Modification of Molecular Fluorophores

Three molecular fluorophores were used to dope Stöber silica: dichloro tris(1,10-phenanathroline)ruthenium(II) hydrate, rhodamine isothiocyanate, and NBD-X SE. The ruthenium salt was used without modification, as the positive charge of the ruthenium cation was sufficient for incorporation into the growing silica matrix.[49] On the other

hand, the other two fluorophores required binding to a silane to allow for incorporation into the silica matrix.[24] Both rhodamine isothiocyanate and NBD-X SE are amine-reactive,[50,76] and the procedure described here follows those reported in literature for amine-reactive dyes.[24,50] To begin, about two milliliters of 200-proof ethanol were added to a four-milliliter glass vial with a Teflon-lined cap. Next, the desired fluorophore was added to the system. Due to the limited quantities of fluorophore involved, determination of the amount to be added was somewhat qualitative: about one-half to one millimeter of dry fluorophore would be collected in the tip of a Pasteur pipette, and dispersed in the two milliliters of ethanol. After flushing the fluorophore from the pipette tip; the glass vial would be topped with dry nitrogen, capped, and then shaken or sonicated to dissolve any remaining dye solids. Following, about 0.2 mL of APES would be added to the mixture, and the vial again topped with dry nitrogen and sealed. Finally, the vial would be wrapped in aluminum foil and left to react at room temperature for twenty-four hours. The modified fluorophore was stored under refrigeration.

2.3.7 Nanoparticle Synthesis

Gold nanoparticles were synthesized through the reduction of $KAuCl_4$ by sodium citrate.[77] Twenty milliliters of one millimolar KAuCl4 in DI water were heated to 90 to 100ºC, at which point two milliliters of 1% sodium citrate dehydrate were added to the system.[77] The mixture was allowed to react for one hour, and then allowed to cool.[77] The particles were stored at room temperature.[77]

CdSe/ZnS quantum dots were synthesized as described in literature.[78,79]

2.3.8 Bawendi Quantum Dot Labeling

Stöber silica particles were coated with a layer of silica doped with CdSe quantum dots following the hydroxypropyl cellulose-based procedure described in literature.[66] To prepare the dots, 0.675 milligrams of CdSe quantum dots in 0.135 milliliters of chloroform were added to a ten milliliter reaction vial and dried under vacuum. Five milliliters of 200-proof ethanol containing 0.3 milligrams of AP and a Teflon-coated stirring rod were then added, the vial topped with dry nitrogen, and a rubber septum added. Following, 0.75 milligrams of APMS were added to the vial through the septum, the system sonicated to disperse the dried quantum dots, and the contents reacted at 40 ºC for at least twenty-four hours under constant mixing. After the reaction was completed, the remaining solids in the mixture were allowed to sediment. If necessary, the mixture was centrifuged to reveal a non-turbid, deeply colored supernatant. The coating of the particles was accomplished by first distributing about two milligrams of the particles in a mixture of 200 milliliters of ethanol, one milliliter of water, one milliliter of 29% aqueous ammonia, and 320 milligrams of hydroxylpropyl cellulose. Following, 0.125 milliliters of the non-turbid modified quantum dot supernatant and 1.875 milliliters of TEOS were added to the particle mixture. After twenty-four hours of reaction at room temperature under constant mixing, the particles were separated by sedimentation.

2.3.9 Nanoparticle Functionalization

Citrate-stabilized gold nanoparticles were funtionalized with MAA as described in literature.[61] Initially, CdSe-ZnS quantum dots were also functionalized with MAA

following the literature method.[67] Later, a modified procedure was used. Quantum dots in chloroform or toluene (five grams per liter) were mixed with *n*-butanol in a 1:1 v/v ratio. To this mixture, sufficient MAA was added to result in a one molar concentration. The reaction was allowed to proceed for at least two hours at room temperature. Afterward, the quantum dots would be extracted using a 0.5 molar aqueous ammonia solution, or the chloroform removed by sparging the mixture with dry nitrogen. Functionalization of the quantum dots with DHLA followed along similar lines, with the only significant exception being that the DHLA was diluted with toluene.

DHLA can be obtained directly from laboratory chemical vendors, or it can be synthesized by reduction of lipoic acid.[68] Due to the relative expense of DHLA compaired to lipoic acid, the synthesis route is justifiable. To begin the synthesis, 0.5 grams of lipoic acid (a yellow solid) were dissolved in ten milliliters of a 0.25 molar aqueous solution of sodium bicarbonate, resulting in a yellow solution. The solution was then chilled to about 3ºC using the same setup described above for the production of chilled Stöber silica. To this chilled solution, 100 milligrams of solid $NaBH_4$ were slowly added to reduce the lipoic acid to DHLA. Significant foaming resulted on addition of the reducing again, and the amount of foaming that can be handled by the experimental setup defined the rate at which $NaBH_4$ was added. The resulting clear solution was allowed to continue reacting at 3ºC for another two to four hours. Afterwards, the DHLA was extracted with an equal volume of toluene. The toluene/DHLA mixture was separated from the aqueous phase, and treated with anhydrous magnesium sulfate to remove any residual water. The magnesium sulfate was

then separated by sedimentation. The DHLA/toluene mixture was then capped with dry nitrogen and stored under refrigeration.

2.3.10 Peptide Bond Nanoparticle Labeling

Amine functional groups will react with carboxylic acid functional groups to from the peptide bond.[80] Thus, it should be possible to coat silica particles with nanoparticles if one is functionalized with an amine, and the other is functionalized with a carboxylic acid. In this work, the coating processes began with silica particles that had been functionalized with an amine using APMS. These silica particles were then coated with MAA functionalized gold nanoparticles, MAA functionalized quantum dots, or DHLA functionalized quantum dots. To accomplish the coating, a dilute solution of the amine functionalized silica particles was slowly added to a solution of the acid functionalized nanoparticles under constant stirring. Initially, the solvent used for both solutions was DI water, but later *n*-butanol was selected. The coated particles were separated from the remaining free nanoparticles by gravity sedimentation.

A silica shell was grown on silica particles coated with MAA and DHLA functionalized quantum dots by dispersing the particles in ethanol containing 0.5 molar ammonium hydroxide and seven molar water. TEOS was then added to a concentration of 0.1 molar to initiate the reaction. Afterward, the quantum dot-silica particles were separated by sedimentation from the reaction mixture and any smaller particles resulting from secondary nucleation.

2.3.11 Embedding Polystyrene Particles with Quantum Dots

Polystyrene latex particles were embedded with CdSe-ZnS quantum dots

following the literature method of dispersing the particles in butanol, and then swelling them with chloroform.[73] Typically, the non-crosslinked polystyrene particles in butanol would be mixed with ten to twenty percent (v/v) chloroform containing about five grams of CdSe-ZnS quantum dots per liter. The quantum dots would be allowed to diffuse into the latex particles for several days. Next, the particles were separated from the remaining free quantum dots by sedimentation. Initially, the particles were dispersed in water. Later, however, the particles were redispersed and sedimented at least three times in butanol to allow for the removal of chloroform and associated deswelling of the particles. Next, the particles were sedimentated and redispersed in ethanol two or three times to remove the butanol before dispersion in water.

2.4 Results and Discussion

The synthesis of Stöber silica has been described as "conceptually simple but experimentally tricky."[81] It is a straightforward matter to mix ethanol, ammonia, water, and TEOS at room temperature and obtain a white precipitate of silica particles. The challenge resides in obtaining a product that might be described as "good" Stöber silica particles. Given that the intended use of the particles described in this work is that of a model system observed through fluorescent confocal laser scanning microscopy (CLSM), a "good" batch of particles would be one where the particles are well formed spheres, exhibit a low degree of polydispersity, are mostly free of fused doublets and clusters, and have a small fluorescent core that allows the particles to be distinguishable in a refractive index-matched media in spite of the convoluting effects of the confocal microscope's point spread function. These criteria are qualitative in nature, and it is not

always possible to define exact quantitative limits that will separate "good" particles from the rest. Certainly, if the extreme limits were obtained – perfectly spherical shape, uniform size down to below the diffraction limit of an electron microscope, zero fused doublets or clusters in the entire batch, and a bright fluorescent core that is smaller than one quarter of the excitation laser's wavelength – the particles would be considered ideal. But, unfortunately, such a degree of perfection is not obtainable. Rather, more practical limits are set. For the purpose of this work, a "good" product batch consists of particles that, when viewed under both an optical scope and fluorescent CLSM in a fluorescent media using a 100X oil-immersion objective, do not exhibit any noticeable lumps or other shape imperfections, nor any degree of polydispersity. In addition, the batch should be cluster-free, with less than one percent of the particles existing as fused doublets. Finally, for the work presented herein, the fluorescent core should be approximately one half the particle diameter or less.

Before proceeding, these two words of caution are offered to anyone attempting Stöber synthesis. First, great care should be taken when relying on the particle size and polydispersity measurements obtained by dynamic light scattering (DLS). In general, the size data appeared to be accurate to only one or two significant figures. Also, there were a number of occasions in which the light scattering measurements reported a monodisperse system that, on visual inspection, was observed to be clearly polydisperse, and vice-versa. (Note that this discrepancy is the reason that a DLS measurement of polydispersity is not used in the specification of acceptable particles in this work.) Furthermore, there were times when a sample consisted almost entirely of clusters, and

DLS interpreted those clusters as large, monodisperse, single particles. It is outside the scope of this dissertation to explore DLS and the implications of some of the assumptions used in calculating the size and polydispersity values reported by the DLS software. Rather, please note that like any other measurement technique, the reported data can be wrong. Whenever possible, DLS results should be confirmed by visual or fluorescent CLSM observations.

The second word of caution deals with trusting the results of Stöber synthesis procedures reported in literature. Given the high standard required of the particles produced for this work, many procedures reported as satisfactory in literature yielded a product was unacceptable. As an example, silica particles labeled with quantum dots by a particular method may be more than adequate for their stated application of fluorescent imaging of veins in mice. But an inability to coat such particles with a silica shell, or a propensity to form clusters would render such particles entirely inappropriate for use as a model system in a fluorescent CLSM sedimentation experiment. In short, it is important to consider that the author of a published synthesis procedure may not have insisted on a level of quality in the final product that was sufficiently high to make the method usable without modification. The specific difficulties of the methods attempted, as well as the results of procedural modifications, will be discussed in greater detail below.

2.4.1 Sol-Gel, Acid Particles, and Spin-On Glass

Silica gels were obtained by following acid-catalyzed TEOS hydrolysis recipes reported in literature,[29] and inadvertently one time when conducted a heated Stöber silica reaction. It was attempted to use these gels as a thermal insulator for sedimentation

cells, but the volume change and cracking on drying in the absence of supercritical drying was too great to allow for their practical use. Still, the formation of the gels was an interesting an inexpensive exercise. The gels exhibited an intriguing resonance when their vessels were struck with the palm of the hand, and when fully dried formed a rigid, glass-like material. An extensive discussion of the potential uses of these silica gels may be found in literature.[27] In addition to gels, silica particles formed by the acid-catalyzed hydrolysis of TEOS were also formed. Consistent with the reports in literature,[31,33-35] large particles (greater than two microns) were obtained, but the dispersions were exceedingly polydisperse and unstable.

Finally, thin films were generated on microscope coverslips using spin-on glass based on HCl, ethanol, and TEOS. The layer thickness obtained from a recipe found in literature[30] was too thin to be measured in the confocal microscope, but could be readily observed if the spin-on glass mixture was doped with a dye such as dichloro tris(1,10-phenanathroline)ruthenium(II) hydrate or rhodamine 6G. Both dyes appeared to be fast, as there was no evidence of the dyes leaching out of the spin-on glass layer when exposed to water or solvents, even if the dyes were used in excessive concentrations. The spin-on glass layer did appear to be porous, as it was unable to protect a layer of PMMA from attack by toluene. Attempts at obtaining a thick layer (> 500 nm) of silica were unsuccessful, and the spin-on glass would invariable crack during the annealing step after the third or forth layer.

2.4.2 Regular Stöber Silica Synthesis

The work on particle synthesis began by focusing on producing Stöber silica

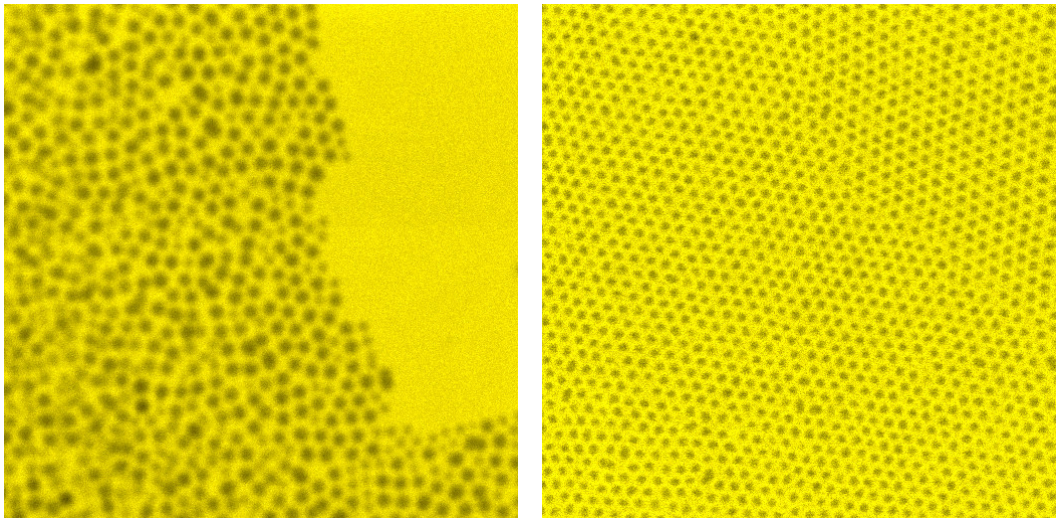

(a) (b)

Fig. 2.1. Effects of distilling TEOS. (a) Silica particles synthesized using TEOS as supplied, and (b) silica particles synthesized using vacuum distilled TEOS.

particles from the ethanol/TEOS/ammonia/water system. Initially, the ethanol used as the solvent was anhydrous denatured alcohol, the TEOS and ammonia were used as supplied, and the water was simply DI water. As seen in Fig. 2.1(a), the results from single TEOS dose experiments were visibly polydisperse. As noted in the literature [22], the vacuum distillation of the alkyl orthosilicate was found to be a necessary step to obtain monodisperse samples such as those shown in Fig. 2.1(b). In addition, use of 200-proof anhydrous ethanol (non-denatured), filtering of the DI water through a twenty-nanometer membrane, and treatment of the alkyl orthosilicate with CaO also improved the quality of the final product. Use of the sizing equations presented in literature[22] [Equations (Eqs.) (2.1) - (2.3)] provided a reasonable estimate of the product size, but rarely predicted the size with a high degree of accuracy.

One reference in literature noted that the maximum ammonia concentration was

two moles per liter, with a maximum size of around 800 nm for the ethanol/TEOS system.[22] While this concentration was capable of producing well-shaped particles with no noticeable polydispersity, it was observed to be too high from a particle stability viewpoint as the product tended to include a signification amount of clusters and fused doublets. Experience indicated that the upper limit on the ammonia concentration should be one molar, resulting in particles of 500 nanometers or less for the ethanol/TEOS system. The concentrations of seven molar water and 0.17 molar TEOS suggested by literature[22] yielded good results. Variation of the water concentration was not explored, as this aspect had already been investigated by others.[22] Attempts to increase the TEOS concentration did yield larger particles as expected, but tended to compromise the stability of the system – especially if the particles were to be later used as seeds in shell growth experiments. Because the TEOS had been treated with CaO, it is not expected that the observed instability was the result of an increase in ionic strength due to a larger TEOS dose. Rather, the decrease in stability is likely due to an increase in particle number density, which in turn increases the probability of particle collisions, and thus the number of collisions resulting in fused doublets or clusters.

During the initial synthesis experiments, the reaction mixture was diluted with a large quantity of DI water after the reaction was complete. This step was intended to lower the ionic strength of the dispersion, and thus increase the stability of the particles as they were sedimented to remove them from the reaction solvent and byproducts. Invariably, the products of these experiments contained a bimodal size distribution with the larger particles typically being close to the size estimated from calculations. On the

other hand, the smaller particles were frequently barely visible in an optical microscope. This occurrence was of great concern, as it took several gravity sedimentation and redispersion cycles to clear out a majority of the smaller particles.

Given the size disparity between the two modes, the different sizes had to be the result of two separation nucleation events. As the larger particles tended to approximate the calculated size, it seemed probable that the secondary nucleation event occurred late in the reaction. Otherwise, the smaller particles would have grown at the expense of the larger particle, preventing the larger particles from reaching the calculated size. As a second nucleation event happening in isolation seemed unlikely for the given reactant concentrations, it was hypothesized that the addition of the dilution water at the end of the reaction precipitated the second event. Perhaps the addition of water in such an excess accelerated the reaction rate of any remaining TEOS, or maybe the change in solvent composition induced the aggregation of previously free sub-nuclei. Whatever the mechanism, using methanol or another anhydrous alcohol for the dilution step instead of DI water resolved the problem.

2.4.3 Addition of Molecular Fluorophores

Three molecular fluorophores were tried for the synthesis of fluorescent Stöber silica particles. One fluorophore, dichloro tris(1,10-phenanathroline)ruthenium(II) hydrate, was used without modification and did result in decent particles. The difficultly encountered with using this particular fluorophore relates to the chloride anions released by it, and the associated rise in ionic strength. This increase in ionic strength was found to compromise the stability of the system if the growth of a subsequent non-fluorescent

shell on the fluorescent particles was attempted. Normally, sedimentation and redispersion of the cores would be sufficient. But because of the ionic strength due to the chloride ions, significant dilution was required to ensure the stability of the cores as they sedimented. Unfortunately, the desired size of the cores was 400-nm or less. With the amount of dilution required, the resulting diluted volume was too great to allow for the gravity sedimentation of such small cores in a timely manner. Centrifugation was also ruled out as this process invariably resulted in fused clusters. Dialysis was attempted with DI water, but the resulting dispersion had too high of a water concentration for the growth of a subsequent shell. Finally, dialysis with alcohol was considered to be cost prohibitive. Overall, the use of this ruthenium dye was found to be appropriate for large (600-nm or larger) fluorescent silica particles, but the complications associated with removal of the chloride ion prevented its use in the 400-nm and smaller fluorescent cores.

The two other dyes, rhodamine isothiocyanate and NBD-X SE (Fig. 2.2), were both reacted with APES prior to use, and injected along with the TEOS when growing fluorescent silica cores. In fluorescent CLSM experiments, the NBD-X SE particles outperformed the rhodamine isothiocyanate particles. The NBD-X SE particles appeared brighter and more resistant to photobleaching. In addition, the NBD-X SE particles benefited from a shorter excitation wavelength, perhaps increasing the resolution of the data. From a particle synthesis point of view, no significant difference was observed between the two dyes, with the presence of the APES dominating the synthesis results. The inclusion of APES resulted in particle sizes that deviated from the

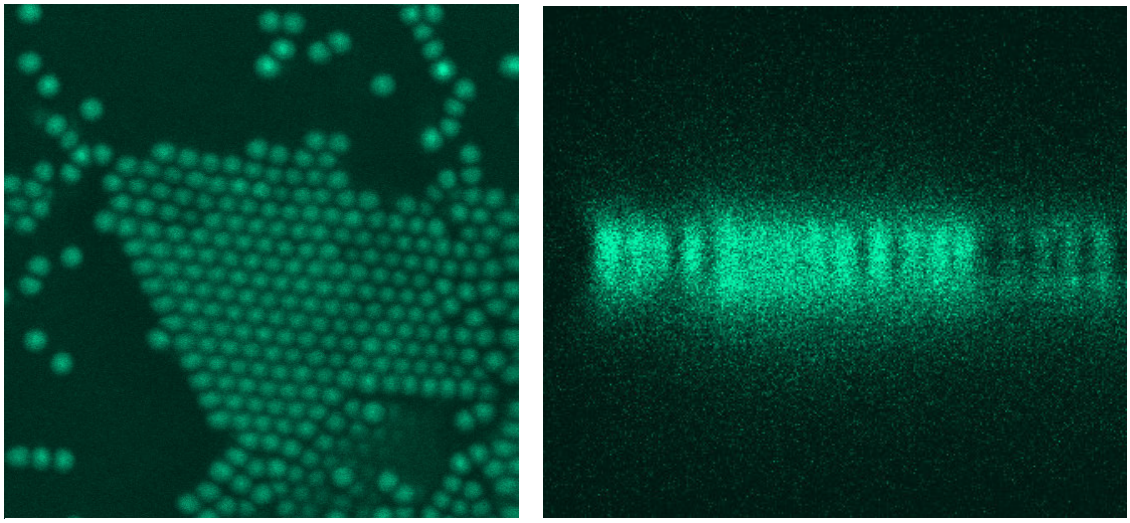

(a) (b)

FIG. 2.2. NBD-X SE labeled silica particles. Imaged (a) horizontally and (b) vertically using a confocal microscope in fluorescence mode.

calculated sizes for particles grown in the absence of a silane. Also, attempts at larger particles (> 500 nm) resulted in what can best be described as a mess. While larger particles grown without silane, but otherwise under identical conditions and reactant concentrations, may have demonstrated a propensity to form more clusters than desired, the results still tended to be monodisperse provided the ammonia concentration was less than two molar. On the other hand, attempts at large fluorescent particles resulted in a dispersion consisting entirely of clusters of particles with a wide distribution of sizes.

Fortunately, it was possible to obtain good quality particles that were less than 500 nm in diameter, and were suitable for the growth of subsequent shells. The observed sizes did deviate from the calculated sizes more than the batches of particles synthesized without a silane present, but it was possible to develop a recipe that would consistently yield cores close to a desired size. Approximately 220-nm fluorescent cores

may be grown at room temperature using 16.8 milliliters of 200-proof ethanol, 2.1 milliliters of DI water, 0.45 milliliters of 29% aqueous ammonia, 0.5 milliliters of 10% v/v APES in ethanol and NBD-X SE, and 0.5 milliliters of TEOS. Variations in size up to about 450 nm may be accomplished by increasing the amount of ammonia added.

2.4.4 Shell Growth

Non-fluorescent silica shells were grown on APES-based fluorescent silica cores. The shell growth occurred at room temperature in an ethanol/TEOS system through the batch addition of TEOS to the original reaction mixture used to grow the cores. No dilution, cleaning, or other reagent addition was involved between the formation of the cores and the growth of the shells. Shell growth was begun two to four hours after the core growth reaction was initiated. In general, it was possible to add a volume of TEOS equal to the initial TEOS dose every two to four hours. Higher addition rates resulted in secondary nucleation. The best results were obtained by dividing the initial TEOS dose into four equal volumes, and adding these doses every thirty minutes. It is believed that by dividing the TEOS addition into smaller, more frequent doses, the shock to the system from the TEOS doses was less which in turn lowered the chances for a secondary nucleation event.

The upper particle size limit for shell growth by this method appeared to be about twice the original core size. The upper time limit for shell growth by this method was approximately twenty-four hours. Attempting to conduct the shell growth over longer periods of time tended to result in an unacceptable number of fused doublets and clusters for a system with an initial ammonia concentration of one molar. While consistently

dosing a synthesis batch with TEOS every thirty minutes over the course of twenty-four hours was experimentally intense, this approach yielded the best particles synthesized as part of this work. Four hours after the last TEOS addition, the system would be diluted with an anhydrous alcohol as previously described to reduce the ionic strength of the mixture while the particles gravity sedimented. Particles produced in this manner were observed by visual microscopy and DLS to be exceptionally monodisperse. The particles were also well shaped, and largely free of fused doublets.

In addition to using batch additions of TEOS, continuous injection of TEOS was attempted as a means to grow shells on particles. The TEOS was diluted with ethanol, and metered into the reacting dispersion using a plastic syringe, syringe pump, and Teflon tubing. The outlet of the Teflon tubing was positioned above the dispersion so that the TEOS/ethanol mixture would drip into the system. Initial experiments allowed the outlet to be exposed to the reactor headspace, and the results were disappointing. It seems probable that the poor results were due to secondary nucleation in the TEOS/ethanol mixture before it contacted the reacting dispersion, most likely due to contamination from the water and ammonia vapor in the reactor headspace. Subsequent trials attempted to duplicate the continuous-inject setup described in literature,[26] but the rate at which the ammonia was stripped from the reactor by a the air used to blanket the TEOS injection outlet was unacceptably high.

2.4.5 Use of Amines as the Catalyst

Amines tend to have a significantly lower vapor pressure than ammonia. So to reduce the potential for both contamination of the TEOS droplet and stripping of the

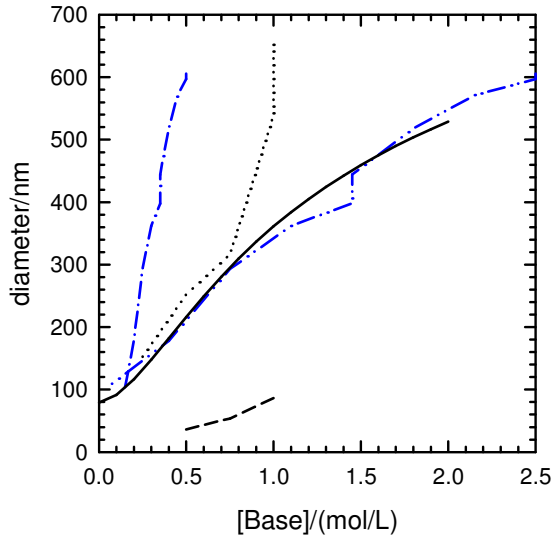

FIG. 2.3. Particle size as a function of solvent and base type. Plots shown are: observed ethanol/dodecylamine (blue dash-dot line), adjusted ethanol/dodecylamine (blue dash-dot-dot line), observed methanol/ammonia (black dashed line), observed ethanol/ammonia (black dotted line), and theoretical ethanol/ammonia (black solid line).

base from the reacting dispersion, the use of amines in lieu of ammonia as the reaction catalyst was explored. Three amines were explored: triethylamine, dibutylamine, and dodecylamine, which have pKa values of 10.75, 11.25, and 10.63, respectively.[82] These values are greater than the pKa of ammonia, which is 9.25, and as a result lower concentrations of amines are required to achieve the same pH value. Dodecylamine, with lowest pKa value of the three amines explored, yielded the most promising results. In addition, as seen in Fig. 2.3, it is possible to convert the dodecylamine concentrations to equivalent ammonia concentrations using an empirical linear relationship of $[NH_3]_{effective}$ equals seven times [Dodecylamine] minus one, thereby allowing use of existing particle size calculations developed for ammonia. Time did not allow for the development of a continuous injection technique using dodecylamine.

2.4.6 Use of Different Alkyl Orthosilicates

In an attempt to obtain particles larger than one micron, the use of tetrapentyl orthosilicate was attempted. Unfortunately, success at duplicating Stöber's results was not achieved. As other methods (discussed below) were successful at achieving particles larger than one micron, this approach was not further pursued.

2.4.7 Use of Different Solvents

A number of different solvents and solvent mixtures were used for Stöber synthesis. These solvents and mixtures included: methanol, ethanol, isopropanol, *n*-propanol, *n*-butanol, *n*-pentanol, DMF, acetone, mixtures of methanol and *n*-propanol, mixtures of methanol and *n*-butanol, and mixtures of ethanol and acetone. Methanol yielded good particles that were, as seen in Table 2.1, considerably smaller than particles produced using ethanol as the solvent. A mixture of 10:6 v/v ethanol to acetone also produced good quality particles that were larger than those observed for ethanol alone. The water needed for the hydrolysis reaction was found to be immiscible in *n*- pentanol. No reaction was observed in DMF. Isopropanol, *n*-propanol, *n*-butanol, and

Table 2.1. Comparison of silica particle diameters measured by DLS, obtained when using methanol or ethanol as the solvent. The reactions were carried out at room temperature with 7M water and 0.10M vacuum distilled TEOS.

$[NH_3]$/(mol/L)	diameter/nm for MeOH	diameter/nm for EtOH
0.25	(non-detect)	150
0.50	34	250
0.75	54	320
1.00	86	540

acetone did produce larger particles than observed in equivalent systems of ethanol, but each was plagued by clustering of the particles, and buildup along the walls of the container. The ethanol-acetone also demonstrated these tendencies, but to a lesser degree, and these negative side effects could be avoided by halting the reaction through dilution after two hours. Mixtures of methanol with *n*-propanol or *n*-butanol exhibited not clear advantage over the ethanol or ethanol-acetone systems.

2.4.8 Use of Chilled Temperatures

Chilling the Stöber reaction mixture to -10ºC and below also resulted in larger particles. The ethanol system did tend to display the clustering and sidewall particle buildup problems encountered with the use of higher alcohols are room temperature. Fortunately, the ethanol-acetone system performed well under chilled conditions, and was capable of producing particles in excess of 1.5 μm with a single dose of TEOS. This success allowed for a novel method to produce large particles with small fluorescent cores (Fig. 2.4). Rather than repeatedly dosing a relatively high number fraction system with TEOS at room or elevated temperatures to grow large particles, it was possible to produce large particles from a single dose of TEOS under chilled conditions using a relatively low number fraction system of fluorescent cores as the particle seeds. The advantage of this approach is that the lower number fraction reduces the chances of the particle collisions and formation of fused doublets and clusters. The use of a single dose of TEOS to the cores also makes this approach easier to execute. The potential disadvantage is that the particles appeared less well-shaped than those grown by repeated doses of TEOS. While the particle quality was sufficient for the

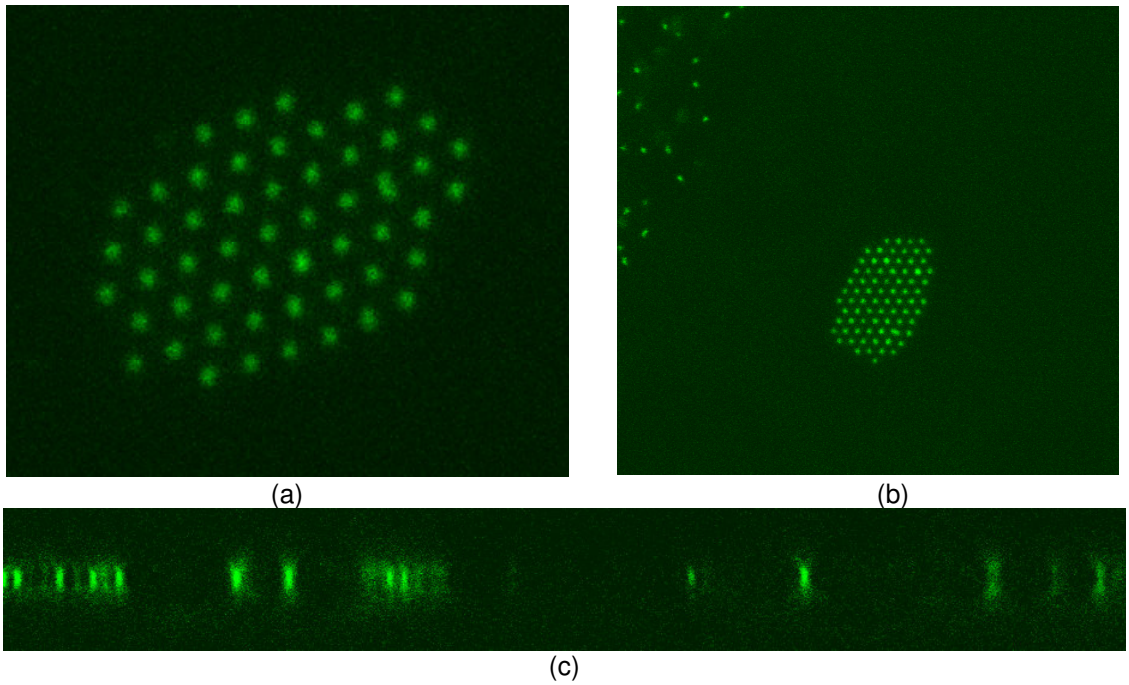

FIG. 2.4. Core-shell particles synthesized under chilled conditions. (a) Colloidal crystal of 400 nm fluorescent silica cores grown to 1.1 μm using the chilled ethanol/acetone system, (b) another crystal grown from the same particle, and (c) vertical scan of particles showing the effects of the confocal microscope's point spread function.

research described in this work, other researchers duplicating these efforts should consider if this reduction in quality is an issue for their applications.

2.4.9 Use of Surfactants

Three surfactants were investigated: SDS, pluronic F108, and CTAB. Particles one micron and larger were obtained by each, but only CTAB was free from stability issues. SDS exhibited the greatest stability issues, perhaps due to the increase in ionic strength associated with the SDS addition. Consistently, the particles grown in the presence of SDS were polydisperse and tended to form clusters. Sonication of the SDS reaction mixture helped resolve the issue of clusters, but not the issue of polydispersity. F108 did form large, monodisperse particles initially free of doublets and clusters.

However, stability was lost on dilution of the reaction mixture. It may be that some residual F108 stabilized the particles in the reaction mixture, and that stability was lost on dilution of the remaining F108. In addition, it is conceivable that the F108 was also incorporated into the amorphous silica matrix, as has been observed for hydrdoxylpropyl cellulose[83], thereby reducing the native silica charge density that would have otherwise stabilized the particles. Whatever the exact cause of the loss of stability, F108 did show some potential, but it was not fully explored as similar results had been obtained by the chilled method discussed above.

Towards the end of the research, CTAB was also tried with good success. The exact recipe consisted of 0.5 mL of a 0.04 molar aqueous solution of CTAB, 0.5 mL of a 1.25 wt% aqueous solution of ammonia, 0.9 mL of DI water, 2.0 mL of 200-proof ethanol, and 0.3 mL of TEOS.[44] The literature describing this method called for the reaction mixture to be mixed only in the first fifteen seconds of the reaction. This brief mixing action did result in good particles. Interestingly though, on repeating the experiment under continuous mixing, the problems of multiple clusters and particle buildup on the sidewalls were observed. These are the same problems that are mentioned above for particles grown under continuous mixing in higher alcohols and in chilled ethanol.

2.4.10 Particle Functionalization

2.4.10.1 Octadecanol

Particles were coated with 1-octadecanol by the method described in literature.[52] The method works well, and the resulting particles were readily dispersible in non-polar

organic solvents such as toluene and chloroform. The biggest challenge to using this method resides in the separation of the particles from the excess 1-octadecanol. To fully dissolve the remaining 1-octadecanol, a considerable amount of ethanol or chloroform was required, resulting in considerable volume that required gravity sedimentation or centrifugation for separation of the particles. This method is recommended if a large quantity of particles (milliliters of particle stock) needs to be made hydrophobic. But for smaller batches of particles, use of a hydrophobic silane such as OTMS is encouraged.

2.4.10.2 Silanes

Coating the particles with either APMS or OTMS did prove tricky at first, but good results were eventually obtained. The challenging aspect resides in avoiding particle clusters as the silanes are coating the particles' surface. To succeed in silanizing the particles, a few considerations need to be addressed. First, the solvent needs to be anhydrous. 200-proof ethanol worked well, but *n*-butanol is recommended as it has been observed to easily support both hydrophilic and hydrophobic particles (an important consideration when coating hydrophilic silica particles with a silane that will impart hydrophobic properties). Second, it is essential to sonicate the sample for the first eight hours of silanization. Failure to do so invariably led to particle clusters. Third, the particles must be separated from the unreacted silane by gravity sedimentation only. Attempts at centrifugation, even at very low speeds, consistently resulted in aggregates that could not be subsequently broken up. Subsequent rinse steps can be accomplished through centrifugation at low speeds, but this course of action is not recommended.

2.4.10.3 Poly(isobutylene)

Attempts at coating silica particles with poly(isobutylene) are ongoing. Particles that have been subjected to the literature method[62,63] will readily disperse in toluene, but they display extensive electrostatic repulsion rather than the reported uncharged interactions.[53] Recently, the procedure was modified. Rather than reacting the modified poly(isobutylene) with tetraethylpentamine, followed by the reaction with bare silica particles; the silica particles were functionalized with APMS, and then reacted with the modified poly(isobutylene). The idea is that the succinimidyl groups on the modified poly(isobutylene) will react with the amine groups on the silane bound to the silica particles, thereby avoiding the need to get the free ends of the tetraethylpentamines to react with the silica surface. Initial results are good – the particles are stabile in toluene, but do not display the long-range repulsion observed in the previous batch.

2.4.11 Nanoparticle Functionalization

Initially, CdSe-ZnS quantum dots were functionalized by the literature method of adding MAA to a dispersion of quantum dots in chloroform.[67] Observations of the product both dispersed in water and bound to silica particles (discussed in greater detail below) by fluorescent CLSM revealed that the functionalization process resulted in aggregation of the quantum dots. The cause of the aggregation appeared to be the attempted formation of water-soluble quantum dots through reaction with the MAA while the dots were dispersed in chloroform, as upon addition of the MAA, the clear dispersion immediately turned turbid. Due to the hydrophobic nature of these particular quantum dots, redispersion in a hydrophilic solvent was not an option. To circumvent

the difficulties associated with converting a hydrophobic particle into a hydrophilic particle in the same solvent, the quantum dots dispersed in chloroform were diluted with an equal volume of *n*-butanol. This action was sufficient to avoid aggregation of the quantum dots during the reaction with the MAA, as indicated by the absence of turbidity throughout the reaction. Similar difficulties were encountered when functionalizing quantum dots in chloroform with DHLA dissolved in toluene, but dilution with *n*-butanol resolved these difficulties, too.

2.4.12 Labeling of Silica Particles with Nanoparticles

2.4.12.1 Bawendi Method

Labeling silica particles with quantum dots was first attempted by the hydroxylpropyl cellulose method described in literature.[66] While functionalizing the quantum dots, it appeared that a significant number of the dots remained aggregated even after the reaction with APES in ethanol. Still, a sufficient number were present in the supernatant after centrifugation to allow use of this method. The incorporation of the functionalized quantum dots into a silica shell around existing particles in the presence of hydroxylpropyl cellulose was also successful as indicated by imaging in fluorescent CLSM, but the particles proved unsatisfactory for this work. Specifically, the particles were unstable and aggregated on gravity sedimentation. Also, attempts to grow a subsequent non-fluorescent silica shell were unsuccessful. It was suspected that these difficulties arose from the use of hydroxypropyl cellulose.

2.4.12.2 Peptide Bond

To avoid the use of hydroxypropyl cellulose, an alternate method to bind

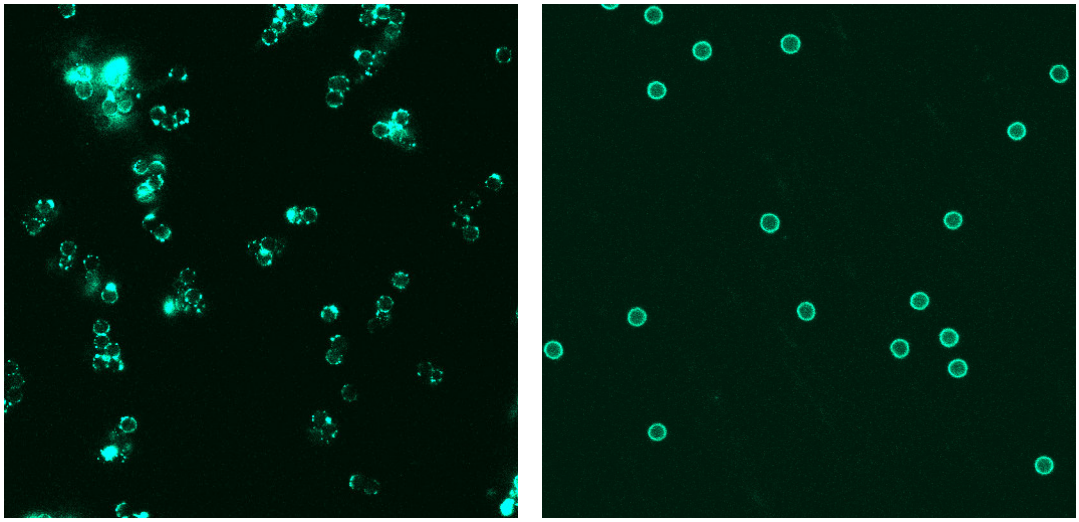

(a) (b)

FIG. 2.5. Binding of quantum dots to silica particles. Comparison of silica particles labeled with quantum dots functionalized with MAA (a) by the literature method, resulting in quantum dot clusters; and (b) by the improved method using butanol that results in a stable dispersion during the functionalization process.

quantum dots to silica was explored. At first, MAA functionalized quantum dots were included in the silica reaction mixture during shell growth. But this approach failed, most likely due to the quantum dots acting as nuclei for new particles – thereby pointing to the need to first bind the quantum dots to the silica surface before initiating the shell growth. As carboxylic acid groups will react with amine groups to form the peptide with APMS. The quantum dots were observed to bond with the silica particles. As discussed above, initial results reveals clusters of quantum dots bound to the silica [Fig. 2.5(a)]. But the modification to the MAA functionalization procedure resolved this problem [Fig. 2.5(b)]. The fluorescence of the MAA coated silica was exceptionally bright compared to that of molecular fluorophore-doped silica particles, and sediments of the coated particles were intensely colored. These quantum dot/silica particles were successfully coated with a nonfluorescent silica shell [Fig. 2.6(a)], but the MAA coated

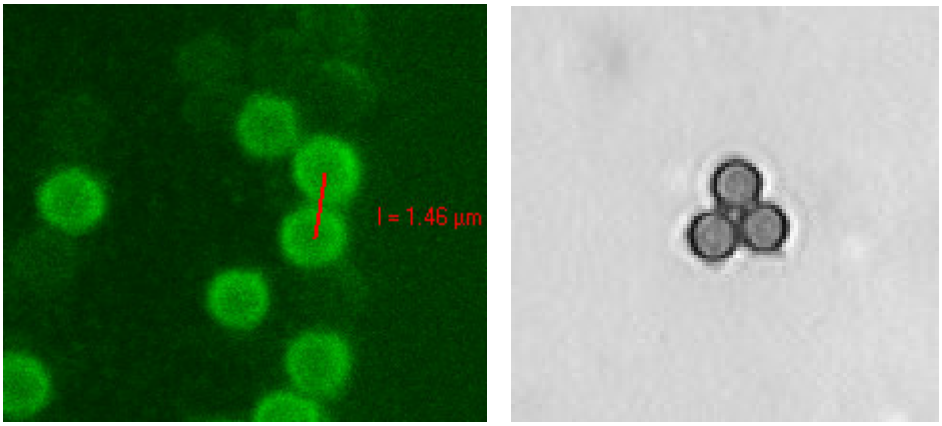

(a) (b)

FIG. 2.6. Shell growth on quantum dot labeled silica particle, and binding of gold particles to silica particles. (a) 1.1 µm silica coated with MAA functionalized quantum dots, followed by a non-fluorescent silica shell; and (b) silica particles coated with MAA functionalized gold nanoparticles, as indicated by the dark perimeters.

dots had a tendency to wash off before the shell was applies, which resulted in limited secondary nucleation during shell growth. To more tightly bond the quantum dots to the silica particles, DHLA – that has two sulfur atoms per molecule available for bonding to the quantum dot surface, as opposed to the one sulfur atom of MAA – was used to functionalize the quantum dots. DHLA coated quantum dots were not observed to dissociate from amine functionalized silica. Recently, non-fluorescent silica shells have been grown on silica particles coated with DHLA functionalized quantum dots.

Gold nanoparticles about twenty nanometers in size and functionalized with MAA by the method in literature[61] have also successfully coated amine functionalized silica [Fig. 2.6(b)]. As with the first attempts at coating silica with MAA and DHLA coated quantum dots, clusters of gold nanoparticles are attached to the surface of the silica particles. Further refinement of the method should result in a uniform coating of gold nanoparticles.

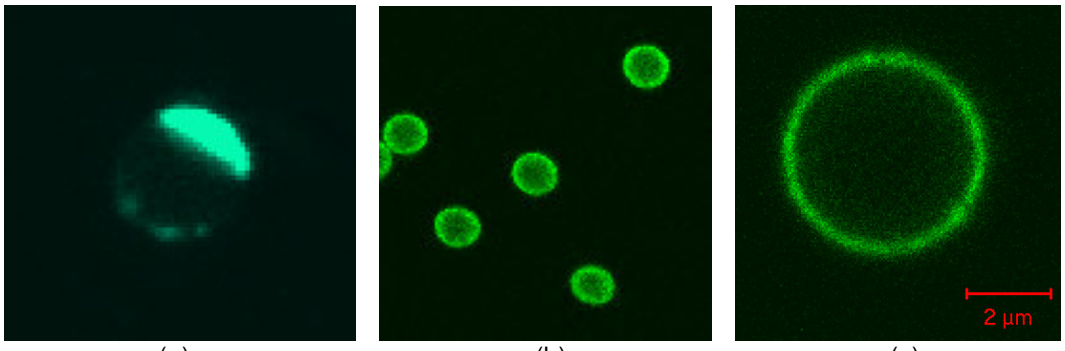

(a) (b) (c)

FIG. 2.7. Labeling of polystyrene particles with quantum dots. (a) Polystyrene particle labeled with quantum dots according to the literature method and then added to water, resulting in a cap of dots; (b) polystyrene particles labeled with quantum dots and then unswollen before addition to water, resulting in a uniform layer of dots; and (c) close-up scan of the same.

2.4.13 Labeling of Polystyrene Particles with Quantum Dots

Embedding quantum dots into the outer boundaries of polystyrene particles according to the methods described in literature[73] were successful. However, the dots were observed to segregate into caps on dispersion of the polystyrene particles in water [Fig. 2.7(a)]. It was hypothesized that the hydrophobic quantum dots were still able to diffuse within the swollen polystyrene, and as a result, aggregated when exposed to water. To avoid this result, it was attempted to unswell the polystyrene particles by repeated sedimentation and redispersion in fresh butanol – the idea being that the chloroform present in the polystyrene and causing the particles to swell would leach out, thereby unswelling the particles and locking the quantum dots into place. This approach has consistently yielded good results [Figures (Figs.) 2.7(b) and 2.7(c)]. These quantum dot-labeled polystyrene particles were then successfully used for aqueous fluorescent total internal reflection microscopy.[64]

2.5 Summary

The particles required for the research described in this dissertation have been successfully synthesis. These include 700-nm to 800-nm Stöber silica particles with 400-nm fluorescent cores, 1.5-μm particles with 700-nm fluorescent cores, and non-fluorescent silica particles coated with a non-dissociating layer of CdSe-ZnS quantum dots. Synthesis of these particles has been achieved through both the successful implementation of procedures documented in literature (e.g., Stöber synthesis of particles, inclusion of molecular fluorophores, growth of silica shells at room temperature, and DHLA functionalization of quantum dots), as well as the development of novel approaches (e.g., combining chilled growth and alternative solvents with fluorescent seeds to achieve large particles with small cores in a single step, and the peptide binding of nanoparticles to the surface of silica particles). While attempts at very large (three to four microns) monodisperse Stöber silica particles were not successful, a great deal of progress has been made in pursuit of this goal, especially in the use of amines as a replacement for ammonia in the Stöber reaction. It is hoped that the experiences documented in this section will assist other researchers who may choose to pursue the fabrication of large Stöber silica particles.

2.5.1 Practical Observations

In the course of this research, it was observed that the vacuum distillation of the alkyl orthosilicate was absolutely essential to obtain good quality particles from Stöber synthesis. Treating the alkyl orthosilicate with CaO before the distillation and using a non-denatured alcohol as the reaction solvent also appeared to have improved the results.

It is difficult to say if filtering the DI water through a 0.02-micron filter had any effect. But as this is a simple step to implement, it is also recommended. The use of amine-reactive molecular fluorophores, especially NBD-X SE, in conjunction with APES produces silica particles suitable for use in fluorescent CLSM.

Shells may be grown on cores produced from amine-reactive molecular fluorophores either through multiple additions of the alkyl orthosilicate at room temperature, or with a single addition in an ethanol-acetone system under chilled conditions. Particles grown through multiple shells will be well shaped and exceedingly monodisperse, but there will be the possibility of forming too many fused doublets. Additions should not exceed the initial alkyl orthosilicate volume every two to four hours. Shell growth experiments by this method should be limited to twenty-four hours for an ammonia concentration of one molar, and with this time limit it will be hard to achieve particle diameters larger than twice the original core diameter. Significantly larger shells can be grown without a risk of numerous fused doublets by the chilled ethanol-acetone method, but there may be a modest reduction in the quality of the particles' shape and monodispersity.

The TEOS-ethanol system is useful for producing particles that are 100 nm to about 500 or 600 nm in diameter. The ammonia concentration should be limited to one molar or less. Modest gains in size can be achieve through shell growth by batch alkyl orthosilicate additions; but larger particles should be produced using the ethanol-acetone system, chilled synthesis, or by the addition of CTAB. Larger particles can be obtained using other solvents or surfactants. However, particle stability can be an issue for these

systems. Methanol is a suitable solvent if particles smaller than those obtained from ethanol are desired. It the concentration is reduced, dedecylamine is an acceptable substitute for ammonia in Stöber synthesis. After the reaction is complete, the dispersion should be diluted with an anhydrous alcohol such as methanol to ensure the stability of the particles during sedimentation. Whenever possible, gravity sedimentation is preferable to centrifugation.

It is possible to functionalize the surface of silica particles with silanes, but particle stability can be an issue. It is best to sonicate the particles for the first eight hours of silanization. *N*-butanol is a recommended solvent, as it has been observed to support both hydrophobic and hydrophilic particles. As with silica particle synthesis, it is best to avoid centrifugation during the cleaning steps if at all possible.

Nanoparticles such as gold particles and CdSe-ZnS quantum dots can be bound to silica particles through the peptide bond if the nanoparticles are functionalized with MAA or DHLA, and the silica particles are functionalized with APMS. It is possible to coat nanoparticles functionalized with carboxylic acid with a silica shell without further preparation, even if the nanoparticles have been bound to a silica particles.

2.5.2 General Observations and Future Work

As noted in the literature review and theory section, the mechanism of Stöber synthesis remains unclear.[28] It was outside the scope of this work to conduct experiments aimed at elucidating the mechanism. Still, the lack of a clear understanding of the mechanism made it difficult to develop the methods necessary to synthesis the particles needed for the remainder of this work. More specifically, in the absence of an

established mechanism, it was hard to predict the effects a change in conditions would have on the final result, making it challenging to proceed in an intelligent manner. For example, it has been established that chilling the Stöber reaction results in larger particles.[40] But are the larger particles a result of slowing the hydrolysis reaction to a greater degree than the diffusion rate of the sub-nuclei (assuming the nucleation-aggregation model holds)? Or is it that chilled temperatures lower the solubility of the silicic acid produced, thereby inducing earlier particle nucleation (assuming the monomer addition model holds)? Without knowing the correct mechanism, it was not possible to predict if the best course of action for growing large particles would be to try slowing the reaction rate (perhaps by using TPOS instead of TEOS), or to try altering the solubility of the silicic acid intermediary (perhaps by changing the reaction solvent). As such, further research into the exact mechanism of particle formation in the Stöber reaction would be of great benefit to researchers concerned with producing large, high quality silica particles.

It should be noted that there remains one area that appears to not have been addressed in the literature: the effects of solvent quality. The use of different solvents was discussed, but the observed effects were attributed to changes in the reaction rate.[21] While that suggested cause may be true, it hard to keep from wondering how different solvents also impact the solubility and nucleation point of the silicic acid intermediary; and (if they exist) the stability, nucleation point, and diffusion rate of the sub-nuclei. Given the importance of the particle nucleation event in Stöber synthesis, it seems reasonable to expect the effects of the solvents on the intermediates to be at least as

important as the solvents' effects on the hydrolysis reaction rate.

In spite of the ambiguity surrounding the Stöber reaction mechanism, a number of generalizations about Stöber synthesis can be drawn from both the literature review and personal experience:

- Increasing the ionic strength through the use of salts, ionic surfactants, or by increasing the base catalyst will result in larger particles, but can also compromise stability;
- Increasing the reaction rate though the use of lower alkyl orthosilicates, or by heating the reaction mixture will reduce the particle size (increasing the catalyst base concentration is an exception to this generalization, but this exception might be explained by an increase in ionic strength);
- Conversely, decreasing the reaction rate by chilling the reaction or using higher alkyl orthosilicates will increase the particle size;
- The addition of surfactants, both ionic and non-ionic, increases the particle size; and
- Altering the solvents from lower to higher alcohols increases the particle size.

Important work also remains on a more practical level. In the immediate future, the method for grafting poly(isobutylene) onto the silica surface needs to be perfected if the work into refractive index-matched depletion crystals (discussed later) is to progress. While the literature provides a detailed explanation for modifying the poly(isobutylene), some important details regarding the actual grafting step have been omitted (such as reaction time or temperature). And as previously stated, the observation of electrostatic repulsion between the modified particles indicates that the current procedure as practiced

was deficient. A recent modification to the procedure has produced some promising results, but the apparent lack of electrostatic interactions has yet to be confirmed.

Also, the issue of clustering and particle buildup on the reactor sidewalls when performing Stöber synthesis under chilled conditions or with higher alcohols needs to be resolved. Previously, it had been assumed that the clustering and buildup occurred because of some inherent characteristic of the higher alcohols and chilled ethanol that destabilized the particles. But the recent experiment with CTAB (mentioned above) that involved only fifteen seconds of agitation points to the rapid mixing of large particles as the likely culprit. Recent experiments with acetone at room temperature and under chilled conditions support this conclusion. As such, growth of large silica particles in higher alcohols or with chilled ethanol may prove to be a perfectly suitable path if the experiments are performed properly.

Finally, the use of amines in lieu of ammonia holds great potential. One immediate benefit is the ability to maintain a constant concentration of the stock base used for the Stöber reactions – something not possible with aqueous ammonia solutions. Due to the loss of ammonia vapors every time the stock ammonia solution bottle is opened, it is impossible to know the exact concentration of ammonia in a reaction mixture without first performing a time-consuming titration. While the associated errors in predicted particle sizes are small when using a new bottle of ammonia solution, the errors can be quite large as the contents of the stock bottle are consumed. Amines also appear to offer significant advantages over ammonia when growing shells on particles by continuous injection. Having a much lower vapor pressure than ammonia (e.g.,

dodecylamine is a solid at room temperature and atmospheric pressure, whereas ammonia is a gas), it is unlikely that amines will be stripped from a reactor by the continuous flow of air used to blanket the alkyl orthosilicate drops. In fact, it may even be possible to completely do away with the continuous air blanket. Finally, quantum dots embedded in base-catalyzed sol-gels are not as susceptible to attack from amines as they are from ammonia.[84] As such, it may be a better approach to use amines to catalyze the synthesis of silica particles that are going to be coated with quantum dots, as well as to catalyze the growth of any subsequent silica shells. In spite of these potential advantages, it is not entirely clear if amines will behave as consistently as ammonia when other factors are altered, such a solvent selection or water concentration. Extensive research into the use of amines to catalyze the synthesis of silica particles would be a valuable addition to the science of Stöber silica.

3. IMAGE AND DATA PROCESSING

3.1 Introduction

The quantification of colloidal microscopy images frequently requires the accurate location of particle centers. At other points in this research, fluorescent intensity data as a function of sedimentation depth which has been convoluted by the microscope's point spread function (Fig. 3.1) needs to be fit to theoretical profiles. Convolution of the theoretical profiles is one option, but it can be computationally expensive. This section first looks at an algorithm used by others to locate particle centers by first convoluting the image with a Gaussian function to average out the effects of random noise, and then identifies particle centers based on local intensity maxima.[85] The data presented will demonstrate that this approach, originally developed for particles with an approximate Gaussian intensity profile,[85] is unsuitable for use with confocal

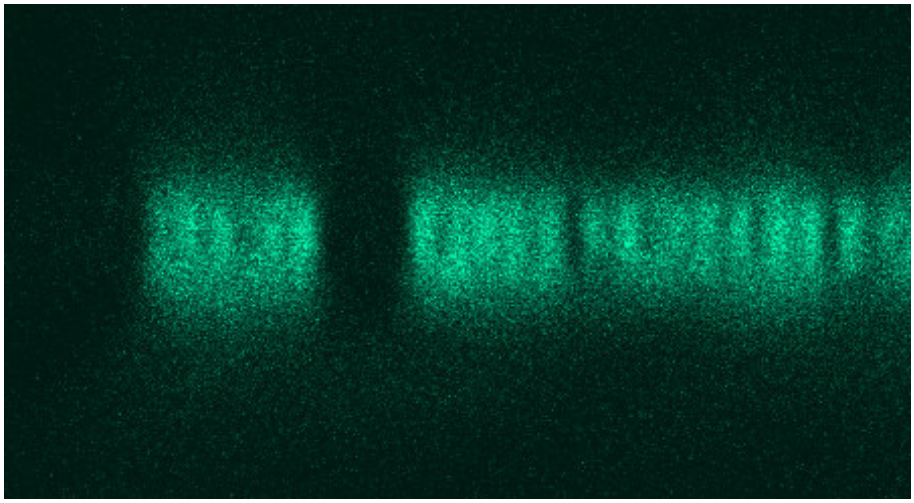

FIG. 3.1. Vertical scan of immobilized fluorescent core silica particles, illustrating the effects of the confocal microscope's point spread function.

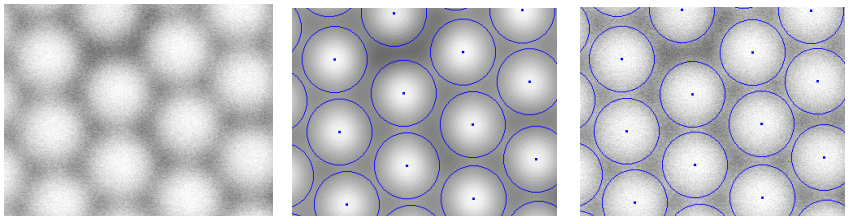

(a) (b) (c)

FIG. 3.2. Image processing of CSLM data. (a) Raw fluorescent image from CSLM, (b) particles located after low-pass noise filter, and (c) improved centers by localized RMS error calculation using pattern and raw image.

images where the particle intensity profile in non-Gaussian. As part of this research, a different approach based to the local root mean squared error between the image and a pattern of the particles' intensity profile is developed and tested (Fig. 3.2). It should be noted that recently a paper was published that proposed a very similar approach.[86] The work described herein had been developed prior to the publication of this other paper, and without knowledge of the work performed by this other research team. It is encouraging to see that other researchers have independently reached the same conclusion about the best approach to processing confocal microscopy images.

This section also details a novel approach to the deconvolution of data. Random noise added to a convoluted data set poses significant complications to performing a deconvolution.[87] Traditional deconvolution algorithms suppress the influence of noise on the deconvolution by seeking a continuous solution that dampens out discontinuities, including those cause by random noise.[87] While this approach reduces the effects of the convolution and is generally appropriate for restoration of images;[87] this research has observed these methods to affect an incomplete deconvolution, resulting in a failure to accurately reproduce curve shapes in test data sets. Such a failure is a substantial

concern for this research, as the curve shape strongly influences the measured parameters when fitting theory to the data. The novel deconvolution approach presented in this section uses a Monte Carlo-like algorithm that relies on *a prior* knowledge of the system behavior (e.g., sediment density will decrease with increased height) to suppress the expression of the random noise in the deconvoluted curve. This new approach allows for the recovery of the curve shape in the data set. Future use of this deconvolution algorithm should substantially improve the computational time required to analyze the sediment intensity profiles discussed in Section 5.

3.2 Literature Review

The determination of colloidal particle coordinates from images collected by microscopy is an important step in the quantification of experimental data. In the literature, there are two approaches to this task that are commonly encountered. The first, and perhaps the more commonly used, approach is to dampen the signal noise and then identify particle centers by the localized intensity maxima.[85] The second approach involves the use of a pattern that describes the appearance of the particles.[86,88] This pattern is then compared to the image by either directly mapping the pattern onto the image,[88] or by deconvoluting the image with the pattern.[86]

The 1996 paper by Crocker and Grier details the method of using a particle's intensity maximum to locate its center coordinates.[85] The method as described by this paper was developed for images captured by transmission optical microscopy.[85] The first step is to even out any large scale intensity variations in the image.[85] This step is accomplished by the following equation[85]

$$A2(x,y) = A1(x,y) - \frac{1}{(2w+1)^2} \sum_{i,j=-w}^{w} A1(x+i, y+j) \tag{3.1}$$

where *A1* is the original image matrix, *A2* is the normalized image matrix, and w is a constant that is greater than the particle size in pixels. The next step is to minimize the effects of random image noise on the length scale of one pixel by convoluting the image with a Gaussian function[85]

$$A3(x,y) = \frac{1}{B} \sum_{i,j=-w}^{w} A2(x+i, y+j) \exp\left(-\frac{i^2 + j^2}{4\lambda^2} \right) \tag{3.2}$$

where *A3* is the convoluted image, *B* is a constant of normalization, and λ controls the range of the Gaussian function and is adjusted based on the degree on random noise present in the image. The Gaussian convolution can be broken apart to improve processing time[85]

$$A3(x,y) = \frac{1}{B} \sum_{j=-w}^{w} \exp\left(-\frac{j^2}{4\lambda^2} \right) \sum_{i=-w}^{w} \exp\left(-\frac{i^2}{4\lambda^2} \right) A2(x+i, y+j) \tag{3.3}$$

Ideally, the effects of the random noise are dampened out by the convolution, leaving the particle centers as the only localized maxima.[85] The convoluted image is then scanned to locate these localized maxima.[85] Finally, the center locations are resolved to sub-pixel precision by an intensity moment analysis about each located center.[85]

This approach has been successfully implemented in the analysis of colloidal particles observed through transmission optical microscopy.[85] It is straightforward to expand Eqs. (3.1) - (3.3) to three dimensions.[86] However, when analyzing three

dimensional image stacks collected by fluorescent confocal laser scanning microscopy (CLSM), some researchers have preferred to locate two dimensional centers in the horizontal image slices, and then match the resulting vertical center columns to the particles' point spread function by root mean squared (RMS) error minimization.[89]

It should be noted that Equation (Eq.) (3.2) is a specific form of the correlation function[88]

$$X(x,y) = \sum_{i=-n}^{n} \sum_{j=-m}^{m} I(x+i, j+m)\{K(i,j)\} \tag{3.4}$$

where I is the image of interest, K is the kernel being compared to the image, and X is the correlation matrix. In theory, X will be maximized at regions where K best correlates to I.[88] Also, the intensity moment analysis is a specific implementation of the centroid analysis:[88]

$$C_x = \sum_{i=-n}^{n} \sum_{j=-m}^{m} x_i \cdot I(i,j) \Big/ \sum_{i=-n}^{n} \sum_{j=-m}^{m} I(i,j) \tag{3.5}$$

where i and j define the region over which the analysis is being performed, x is the x-coordinate of the pixel $I(i, j)$, and C is the coordinate of the moment.

The second general approach to identifying particle centers involves the use of a pattern that describes the image of a single particle.[88] The difference between the pattern and the image is then calculated, and particle centers are considered to be located at the coordinates where the least difference between the pattern and the image exist.[88] One

method of comparing the pattern, or kernel, and the image is by the sum-absolute difference method:[88]

$$SAD(x,y) = \sum_{i=-n}^{n} \sum_{j=-m}^{m} [I(x+i, y+j) - K(i,j)] \tag{3.6}$$

where *SAD* is the sum-absolute difference matrix.

In a recent paper (electronically published on September 26, 2007), the authors considered the observed image to be a convolution between the particle pattern and the particle coordinates. To find the particle coordinates, a chi-square hypersurface (χ^2) is calculated[86]

$$\chi^2(x,y,z) = \sum_{i=-n}^{n} \sum_{j=-m}^{m} \sum_{k=-l}^{l} \frac{[K(i,j,k) - I(x+i, y+j, z+k)]^2}{\sigma(i,j,k)^2} \tag{3.7}$$

where σ is a constant. Minimum values of χ^2 represent the best fit between the pattern and the image – thereby locating the particle centers. A careful inspection of this equation will show it to be functionally equivalent to calculating the RMS error between the pattern and different locations of the image.[86]

Finally, it should be commented that a number of image restoration algorithms have been developed to remove the convoluting effects of the microscope's point spread function from the observed image.[87] The methods tend to be iterative in nature, as a direct deconvolution of the latent image from the point spread function by Fourier transforms is prohibited by image noise.[87]

3.3 Theory

To understand image processing as it relates to the CLSM data collected for this

dissertation, it is important to have some knowledge of convolutions and Fourier transforms. Images and profiles (*I*) collected by CLSM can be described as convolutions of the latent image (*L*) and the microscope's point spread function (*PSF*), plus a random noise signal (*n*)

$$I_{x,y,z} = L_{x,y,z} \otimes PSF_{i,j,k} + n_{x,y,z} \tag{3.8}$$

where $\otimes$ denotes a discrete convolution[87]

$$L_{x,y,z} \otimes PSF_{i,j,k} = \sum_i \sum_j \sum_k L_{x-i,y-j,z-k} \cdot PSF_{i,j,k} \tag{3.9}$$

Likewise, the latent image can be considered a convolution of the particle centers (*D*) and the particles' latent pattern (*P*)[87]

$$L_{x,y,z} = D_{x,y,z} \otimes P_{i',j',k'} \tag{3.10}$$

$$I_{x,y,z} = D_{x,y,z} \otimes P_{i',j',k'} \otimes PSF_{i,j,k} + n_{x,y,z} \tag{3.11}$$

The latent pattern convoluted by the point spread function, in turn, can be replaced by an experimentally observed pattern or kernel (*K*)[86]

$$I_{x,y,z} = D_{x,y,z} \otimes K_{i'',j'',k''} + n_{x,y,z} \tag{3.12}$$

According to the convolution theory, a convolution may be accomplished by transforming both the latent image and the point spread function into Fourier space, multiplying the two matrixes entry-by-entry, and then transforming the result back into real space.[87] In the same manner, a deconvolution may be accomplished – provided that the transformed convoluted matrix is divided, rather than multiplied, by the transformed point spread function.[87] In practice, however, deconvolution by this route is prohibited

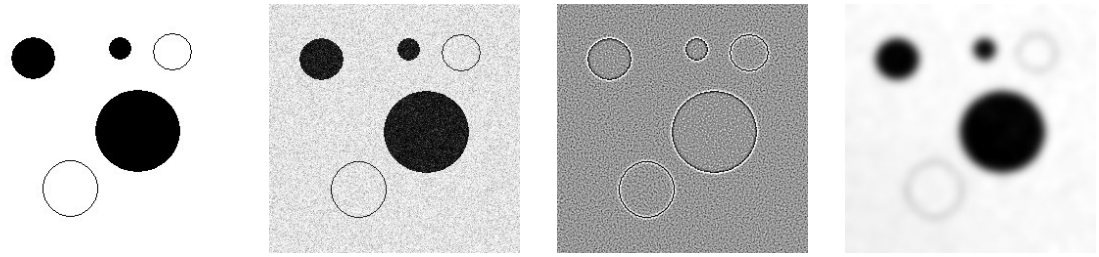

(a) (b) (c) (d)

FIG. 3.3. Image processing using Fourier transforms. (a) Original image, (b) image after the addition of random noise, (c) high pass filter applied to noisy image, demonstrating edge detection, and (d) low pass filter applied to noisy image, demonstrating noise suppression.

by the presence of random noise in the observed image.[87] This fact is because the deconvolution will significantly enhance any random noise present, thereby resulting in an unusable image.[87]

Although Fourier transforms cannot be used to deconvolution observed images, it does not mean that the transform is without use in image processing.[90] The effect of the Fourier transform is to reproduce the image with sin and cosine waves of various wavelengths, where the output values are the coefficients of the various waves.[91] Because the image has been recreated by the constructive and destructive interference of waves with differing wavelengths, it is possible to filter out different feature sizes in the image by setting the coefficients of the waves with corresponding wavelengths to zero.[90] For example, as shown in Fig. 3.3, to identify edges in an image, a high-pass filter is applied, where only the coefficients of the high frequency waves are retained.[90] The result, after transforming the filtered data set back it to real space, is an image in which only the features that can be replicated with high frequency waves (i.e. features exhibiting a sudden change, such as the edge of an object).[90] Likewise, a low-pass filter in Fourier space will remove sharp features, such as random noise, while retaining the

larger structures.[90]

The Fourier transform ($\mathcal{F}$) and inverse Fourier transform ($\mathcal{F}^{-1}$) are calculated accordingly[91,92]

$$F(k) = \int_{-\infty}^{\infty} f(x) e^{-2\pi i k x} dx \tag{3.13}$$

$$f(x) = \int_{-\infty}^{\infty} F(k) e^{2\pi i k x} dk \tag{3.14}$$

Recast to accommodate digital data, the discrete Fourier transform (DFT) and inverse discrete Fourier transform (DFT^{-1}) are[90,91]

$$F_k = \frac{1}{\sqrt{N}} \sum_{x=0}^{N-1} f_x e^{-2\pi i k x / N} \tag{3.15}$$

$$f_x = \frac{1}{\sqrt{N}} \sum_{k=0}^{N-1} F_k e^{2\pi i k x / N} \tag{3.16}$$

Provided the image dimensions are in powers of two, substantial savings in computational time can be realized by implementing the DFT and DFT^{-1} using the fast Fourier transform (FFT) and inverse fast Fourier transform (FFT^{-1}) algorithms.[93] The FFT and FFT^{-1} algorithms are complex.[93] Fortunately, these algorithms have already been coded in major programming languages, such as FORTRAN, and these codes are freely available in literature.[93]

3.4 Experimental

Center location and deconvolution codes were initially prepared using the

programming feature in MathCAD. Although the calculations performed by MathCAD were considerably slower that equivalent calculations performed in FORTRAN, the graphical interface in MathCAD greatly eased the development of the image processing algorithms. After the algorithms had reached a functioning level in MathCAD, they were coded in FORTRAN for more extensive testing and implementation.

Whenever possible, synthetic data sets that closely replicated real data were prepared for the testing of the different data processing codes. This approach allowed for the absolute measurement of the performance of the algorithms, which was not considered possible when using real data alone. In each case, the algorithms were first tested using synthetic data sets without noise to gauge the appropriateness of the general approach. The algorithms were then tested using the same data sets with the addition of random noise.

The particle center location codes were first tested using one dimensional particle profiles that corresponded to profiles observed in transmission optical microscopy and fluorescent CLSM. Next, the codes were evaluated using three dimensional particle profiles. The particle center location codes were judged on their ability to accurately identify particle centers. The deconvolution codes were tested first with convolutions of simple, one dimensional shapes and curves, and then with convolutions of ideal particle density profiles as calculated by theory. As the deconvolution code was required only for the analysis of one dimensional density profiles, subsequent testing with three dimensional data sets was not attempted. The deconvolution codes were judged on their ability to accurately reproduce the shape of the latent density profiles.

In addition to the use of synthetic data sets, the codes were also tested using real data sets. The difficulty associated with using real data sets is that the "correct answer" is not known. As such, the evaluations using real data sets are more qualitative in nature than the evaluations using synthetic data sets. Particle center location codes were judged on their ability to identify locations that appeared to be the correct centers when marked on the images. Similarly, the deconvolution codes were judged on their ability to produce a latent density profile that appeared believable and corresponded well to a theoretical curve that had be previously convoluted and fit to experimental data set.

3.5 Results and Discussion

3.5.1 Center Location

The initial work into locating particle centers began with implementation of the Gaussian convolution/intensity maxima algorithm described in the literature review section of this paper. As the algorithm had been originally developed for transmission optical microscopy [Fig. 3.4(a)], control images with a Gaussian intensity profile were simulated. In the analysis, 10,000 one dimensional Gaussian particles with a radius of eight units were simulated, onto which random noise with a twenty percent standard deviation was superimposed [Fig. 3.4(b)]. After convoluting the synthetic images with a Gaussian function, the local maxima was observed to indicate the correct particle center 97.98% of the time. The Gaussian convolution/intensity maxima algorithm was also tested on one dimensional particles with broad intensity profiles such as those observed in fluorescent CLSM [Fig. 3.4(c)]. Again, 10,000 particles with a radius of eight units were simulated, onto which random noise with a standard deviation of twenty percent

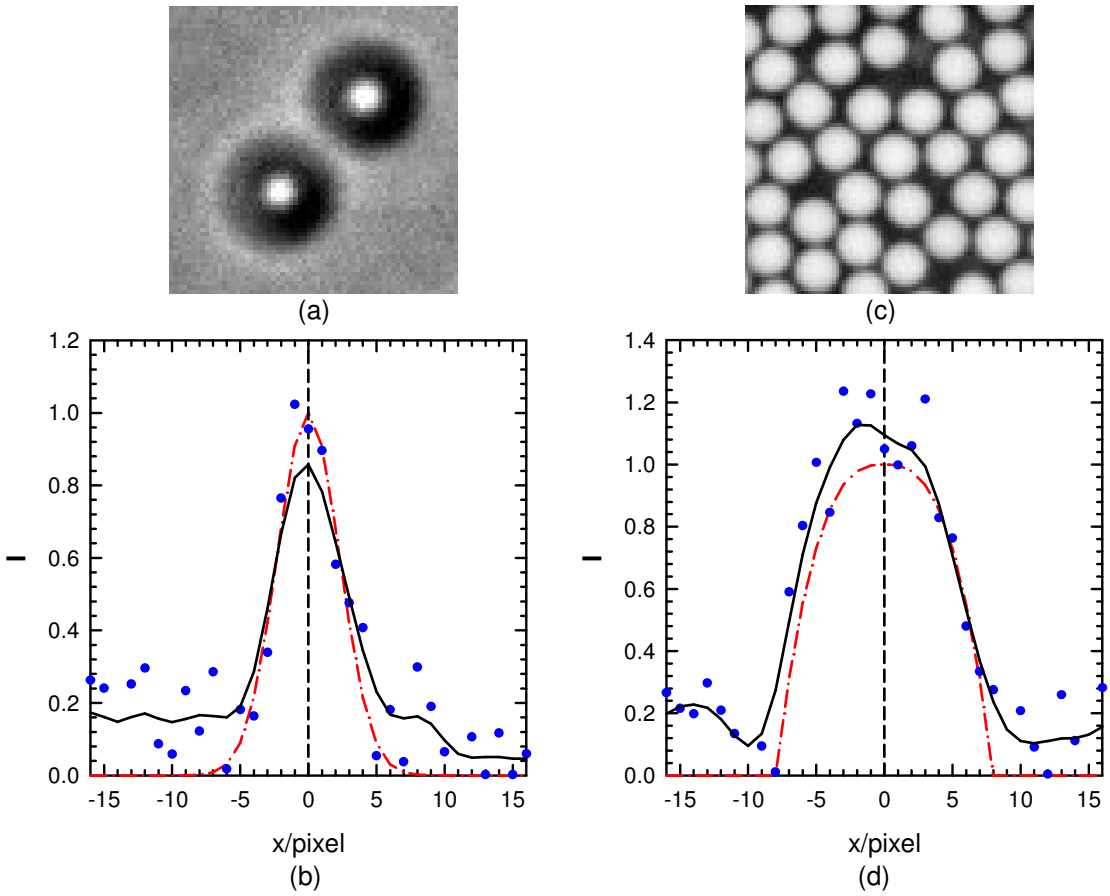

FIG. 3.4. 1-D particle profiles used to test image processing approaches. (a) Transmission optical microscopy image of two colloidal particles, (b) 1-D synthetic image of a Gaussian particle (red, dash-dot line) onto which random noise is added (blue dots) and a Gaussian convolution is applied (black, solid line), (c) confocal microscopy image of fluorescent colloidal particles, and (d) 1-D synthetic image of a fluorescent particle (red, dash-dot line) onto which random noise is added (blue dots) and a Gaussian convolution is applied (black, solid line).

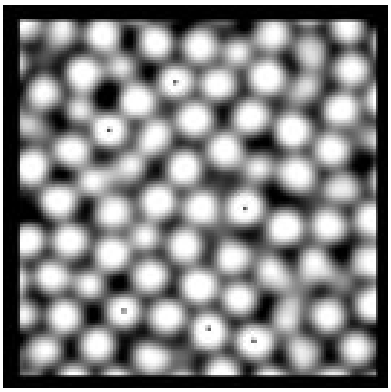

FIG. 3.5. Failure of the Gaussian convolution approach. One slice of a 3-D fluorescent confocal image stage after convolution, marking centers as located by the Gaussian convolution approach. For the six centers that occur in this particular slice, visual inspection suggests that five may be incorrect.

was added [Fig. 3.4(d)]. In this case, the algorithm correctly located the particle centers only 30.12% of the time. Furthermore, when the algorithm was applied to three dimensional image stacks collected by fluorescent CLSM, the located centers appeared incorrect (Fig. 3.5).

The failure of the Gaussian convolution/intensity maxima approach to accurately locate centers in fluorescent CLSM images, along with its success in locating centers in transmission optical microscopy, may be understood by considering the nature of convolutions in general. The random noise on the length scale of one pixel results in many localized maxima that are not related to the particle centers, thereby presenting a significant problem to an intensity maxima-based approach to locating particle centers. To deal with this problem, this particular approach employs a convolution to smooth out the random noise. At first inspection, this approach appears to work because a convolution is simply a weighted average. But more is going on than simply averaging out the noise.

Recalling Eq. (3.4), convoluting an image of particles results in a new image that is the correlation surface between the particles and the convoluting pattern. As a result of this correlation calculation, two things happen when the Gaussian convolution is applied to an image of particles with Gaussian profiles: (1) the noise is dampened out; and (2) the particle profiles are retained. But the correlation between the particle profiles and the convoluting function is lost when the routine is applied to an image of particles whose profiles differ from the Gaussian function. In this case, both the random noise and the particle profiles are dampened. Further, the broad profiles exhibited by the

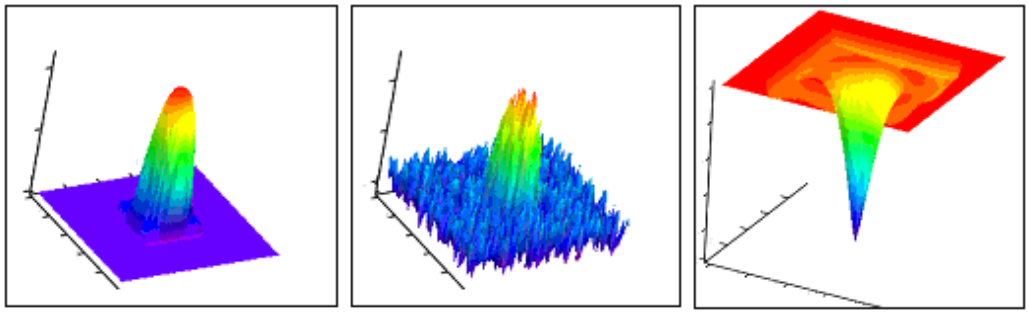

(a) (b) (c)

FIG. 3.6. 2-D particle profiles used to test RMS error image processing approach. (a) 2-D synthetic confocal particle, (b) same with the addition of random noise, and (c) RMS error surface for noisy particle and ideal pattern.

particles enhance the probability that the noise at a location other than a particle center will result in a spike too large to be fully dampened out by the convolution – thus resulting in the location of an incorrect center.

Because of these results, an alternate approach was sought to locate center in fluorescent CLSM images. One option would have been to convolute the images with a kernel that replicated the observed broad particle profiles. But the approach would no longer allow the convoluting function to be broken up, as was the case with the Gaussian function [Eq. (3.3)]. With the computational speed advantages of the Gaussian convolution/intensity maxima method lost, it was felt that a better tactic would be to simply calculate the local RMS error between the kernel and the image

$$RMS(x,y,z)=\sqrt{\frac{\sum_{i=-n}^{n}\sum_{j=-m}^{m}\sum_{k=-l}^{l}[I(x+i,y+j)-K(i,j)]^2}{(2n+1)(2m+1)(2l+l)}} \tag{3.17}$$

Points of lowest RMS error would then be considered the particle centers. As can be seen in the two dimensional example in Fig. 3.6, the effect of the RMS calculation is to

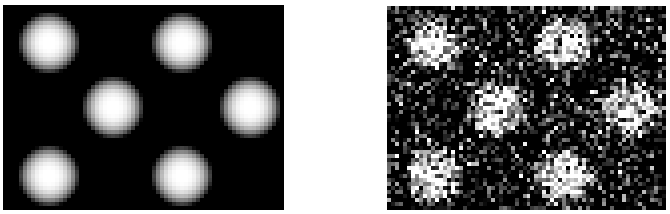

(a) (b)

FIG. 3.7. 3-D particle profiles used to test RMS error image processing approach. (a) 3-D synthetic particles and (b) same with random noise.

transform the broad, noisy surface into a smooth surface with a sharp minima located at the particle centers.

The RMS error method was applied to the same 10,000 one dimensional particles with broad profiles and twenty percent standard deviation noise, and the correct particle centers were located 99.69% of the time, as compared to 30.12% of the time for the Gaussian convolution/intensity maxima approach. The RMS error method was then applied to 398 three dimensional broad-profile particles with a radius of eight voxels and noise of forty percent standard deviation (Fig. 3.7), and the particle centers were located 100% of the time. Interestingly, increasing the dimensions of the system improves the performance of the RMS error approach, as there are a greater number of data points to compare with the pattern. Application of the RMS error approach to real data yielded results that appeared correct [Fig. 3.8(a)]. Further, by adjustment of the kernel to match the complete particle appearance, the method could discriminate between particle centers and anomalous bright regions cause by constructive interference in transmission optical microscopy [Figs. 3.8(b) and 3.8(c)].

Because of the expense associated with calculating the RMS error surface or volume, it was considered desirable to avoid performing the calculation over the entire

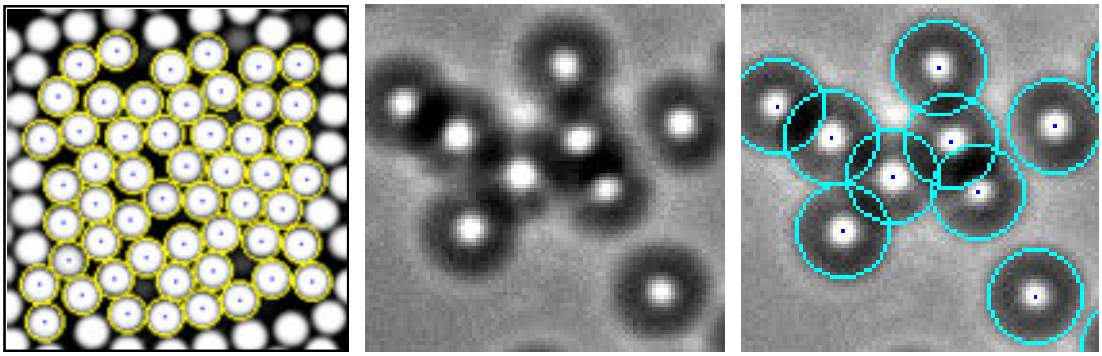

(a) (b) (c)

FIG. 3.8. RMS error image processing approach applied to actual data. (a) Centers located in a 2-D confocal image using RMS error minimization, (b) transmission optical microscopy image of colloidal particles with anomalous bright spots not associated with particle centers, and (c) centers correcting located with RMS error minimization by including dark rings in the intensity pattern.

data set. A more efficient approach would be to limit the RMS error calculations to regions close to likely centers. One obvious method would be to use the computationally efficient Gaussian convolution/intensity maxima approach to locate approximate center locations, and then to refine the locations using RMS error calculations. Another tactic would be to use a low-pass filter in Fourier space to deal with the random noise. The two methods were compared by generating radial distribution functions from the same crystalline image data, and then comparing the distribution function peak widths. The low-pass filter was observed to generate more narrow peaks than the Gaussian convolution, thereby indicating that the low-pass filter did the best job of locating particle centers. This result is likely due to the fact that the sine and cosine waves used in the Fourier transform better approximated the broad particle intensity profiles. However, both methods performed sufficiently well for use in determining particle centers. The deciding factor comes down to computational time. The number of calculations required to implement the Gaussian convolution increases

with particle size. On the other hand, the number of calculations required for the low-pass filter is constant – only the cutoff point of the filter varies with particle size. The Gaussian convolution and the low-pass filter were roughly equivalent when applied to two dimensional images of particles with radii of about ten to twenty pixels. For smaller particles, the Gaussian convolution was fastest. And for larger particles, the low-pass filter was more efficient.

3.5.2 Profile Deconvolution

As was noted in the theory section, the images collected by fluorescent CLSM are a convolution of the latent image and the microscope's point spread function, onto which random is added. The convolution of the image by the point spread function can represent a significant problem when analyzing fluorescent CLSM data of colloidal systems, as it can potentially smear or blur together the images of the individual particles. This resulting overlap of the images can then result in errors in the measured particle locations.[86]

For reasons that will be discussed in Section 5, two types of fluorescent CLSM images were collected for the research presented in this dissertation: two dimensional horizontal scans, and two dimensional vertical scans. The horizontal scans were used to quantify particle-particle separations. In this case, it was possible to control the impact of the convolution by the point spread function through the use of fluorescent core/non-fluorescent shell particles. The vertical scans were used to quantify the variation in particle volume fraction with elevation in colloidal sediments, thereby allowing the determination of interparticle forces through the fitting of theoretical sedimentation

profiles to the observed profiles. Unfortunately, the use of core/shell particles was not sufficient to alleviate the difficulties caused by the point spread function in this application. Two additional options to address the convolution included: (1) the convolution and subsequent fit of a theoretical profiles to the measured data; and (2) the deconvolution of the observed profiles. For the work addressed in Section 5, the first option was selected as its implementation was the most expedient. But because the convolution of the theoretical profiles is computationally expensive, work has continued to identify an appropriate method for deconvoluting the observed profiles.

As previously stated, the presence of noise in the observed images prevents the use of Fourier transforms for deconvolution. However, a number of iterative algorithms have been developed to address the deconvolution of noisy image data. The initial attempts at deconvoluting the sedimentation profiles utilized some of these algorithms, but the results were unacceptable. The problem is that the algorithms have been developed to sharpen microscope images,[87] were an exact recovery of the latent image is not required. As such, the algorithms deal with the issue of noise by seeking solutions that avoid sudden spikes or discontinuities. The results are images that are only partially deconvoluted. While this tactic is able to yield significantly improved images,[87] the incomplete deconvolutions were observed to fail to exactly reproduce the shape of trial sedimentation profiles. This failure is a significant problem because, as will be fully explained in Section 5, the shape of the sedimentation profiles directly impacts the theoretical interparticle forces that are inferred from the profiles.

During the course of this work, it quickly became apparent that a strategy other

than the avoidance of discontinuities would be required to control the impact of noise on the deconvoluted profiles. Fortunately, another piece of information about the profiles is known that will allow the influence of random noise to be minimized: throughout the entire profile, the particle volume fraction (and thus average fluorescent intensity) will be decreasing with increasing elevation. A second useful fact is that the area under the latent curve will be the area under the convoluted curve divided by the area under the point spread function. This fact will permit the exclusion of numerous potential latent curves without the need for expensive calculations. The proposed algorithm follows a Monte Carlo-type approach, where the values in the bins of the latent profile are randomly shuffled around in packets of a fixed amount to: (1) minimize the RMS error between the observed profile and the convoluted latent profile; and (2) produce a latent profile that decreases with increasing elevation.

First, the area under the latent curve (A_{latent}) is determined by dividing the area under the convoluted curve by the area under the point spread function

$$A_{latent} = \sum_{i=0}^{z} I_i \Bigg/ \sum_{j=0}^{p} PSF_j \tag{3.18}$$

where z is the maximum bin of the convoluted profile, and p is the maximum bin of the point spread function. This total area is then evenly distributed throughout the range of the latent profile (bin *L1* to *L2*)

$$L_k = \frac{A_{Latent}}{L2 - L1 + 1} \tag{3.19}$$

where k = bin *L1* to *L2*. All bins of the latent profile outside of the range *L1* to *L2* are set

to zero. Next, the latent profile is convoluted (*LC*) and the total initial RMS error (RMS_0) is calculated

$$LC_i = \sum_{j=0}^{p} L_{i+j-peak} \cdot PSF_j \tag{3.20}$$

$$RMS_0 = \sqrt{\frac{\sum_{i=0}^{z} [I_i - LC_i]^2}{z+1}} \tag{3.21}$$

where peak is the bin corresponding to the maximum value in the point spread function. Following, the iteration steps begin. The index *k* cycles through all bins from *L1* to *L2*. For each advancement in *k*, a second index value (*k2*) is randomly selected between *L1* and *L2*. If *k2* = *k1*, the selection is discarded and *k* advances to its next value. If *k2* does not equal *k1*, then a relatively small constant (step) is subtracted from the latent profile at *k*, and added to the latent profile at *k2*

$$L_k = L_k - step \tag{3.22}$$

$$L_{k2} = L_{k2} + step \tag{3.23}$$

Because only two bins in the latent curve are being altered, it is not necessary to convolute the entire latent curve again. Rather, the previously calculated convoluted latent curve is altered directly

$$LC_{k+j-peak} = LC_{k+j-peak} - step \cdot PSF_j \tag{3.24}$$

$$LC_{k2+j-peak} = LC_{k2+j-peak} + step \cdot PSF_j \tag{3.25}$$

where *j* = 0 to *p*. These four changes are rejected if:

(1) $L_k < 0$;

(2) $L_k/L_{k+1} < 0.999$;

(3) $L_{k2-1}/L_{k2} < 0.999$, provided *k2* does not equal *l1*; and

(4) the RMS error is increased.

Otherwise, the changes are accepted. It is worth noting that the computational time can be reduced by first checking conditions 1 – 3 before recalculating the RMS error. Also, the code was unable to converge if it was rigidly required that $L_k > L_{k+1}$ and $L_{k2-1} > L_{k2}$. By allowing the ratios to be slightly less than unity in conditions 2 and 3, the code was able to converge on acceptable solutions while minimizing the effects of random noise on the deconvolution.

Fig. 3.9 provides the point spread function used in the following tests. To test the algorithm, a synthetic sedimentation profile was created. Shown in Fig. 3.10, the simulated profile begins at bin 441, decays to a solid/fluid transition at bin 1014, and then further decays to non-detect levels by bin 2228. The equations used to generate this profile will be provided in Section 5. For now, the only important consideration is that this theoretical profile is consistent with profiles that may be observed in experiments. The theoretical profile was then convoluted using the point spread function. As with the theoretical profile, this point spread function is consistent with those observed in fluorescent CLSM data. A realistic level of random noise was then added to the convoluted curve. For this trial, the lower end of the latent profile range was set to the known start of the theoretical profile: bin 441. The latent profile determined by the algorithm is satisfactory. It does tend to assume a stepwise, discontinuous form.

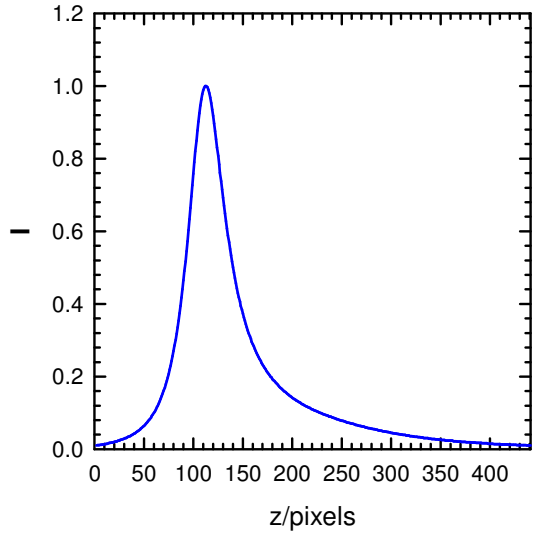

FIG. 3.9. 1-D vertical intensity point spread function measured by fluorescent CLSM.

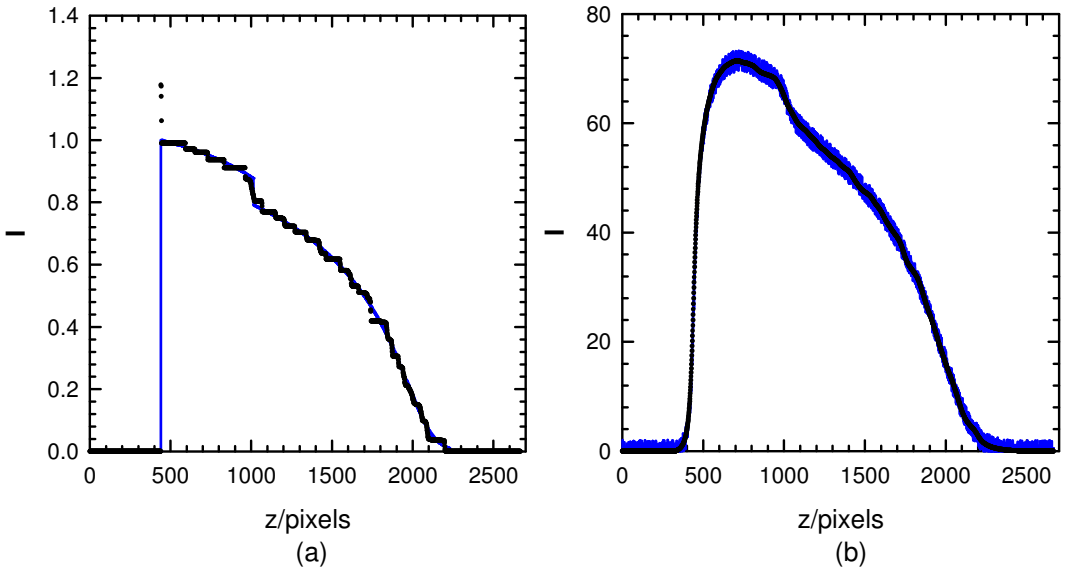

FIG. 3.10. Theoretical profiles used to test the deconvolution approach. (a) theoretical intensity profile (blue line) and deconvoluted latent profile (black line); and (b) convoluted theoretical profile with the addition of random noise (blue line) and convoluted latent profile fit to the convoluted theoretical profile (black line)

Nevertheless, it successfully reproduces the shape of the theoretical profile, including the location of the solid/fluid transition. Overall, the algorithm is successful in suppressing the effects of the random noise added to the convoluted profile without compromising the shape of the deconvoluted latent profile. The stepwise, discontinuous form is not considered a problem, as the deconvoluted latent profile remains suitable for the fitting of theoretical profiles.

Next, the ability of the algorithm to detect the start of the latent curve was investigated by beginning the latent profile range at bin 200 and bin 600 in two differentdeconvolutions (Figs. 3.11 and 3.12). The theoretical and convoluted profiles remained unchanged from the first deconvolution mentioned above. For the deconvolution that began at bin 200, from the convoluted theoretical profile and the convoluted latent profile it can be easily seen that the range for the latent profile begins on the incorrect bin. Also, because the area under the latent profile is defined, beginning the latent profile on a bin that is too low or too high results in the rest of the curve either undershooting or overshooting the correct profile, thereby further increasing the total RMS error. As a result, it is possible to easily identify the correct starting bin by varying this bin to minimize the total RMS error.

With the algorithm working with simulated data, it was then tested on actual experimental data collected from a sedimentation experiments (again, the source of these data will be discussed in detail in Section 5). Because the true latent profile behind the convoluted data is unknown, the theoretical curve that had been previously fit to the data by convolution and RMS error minimization. The starting bin was varied, and bin 624

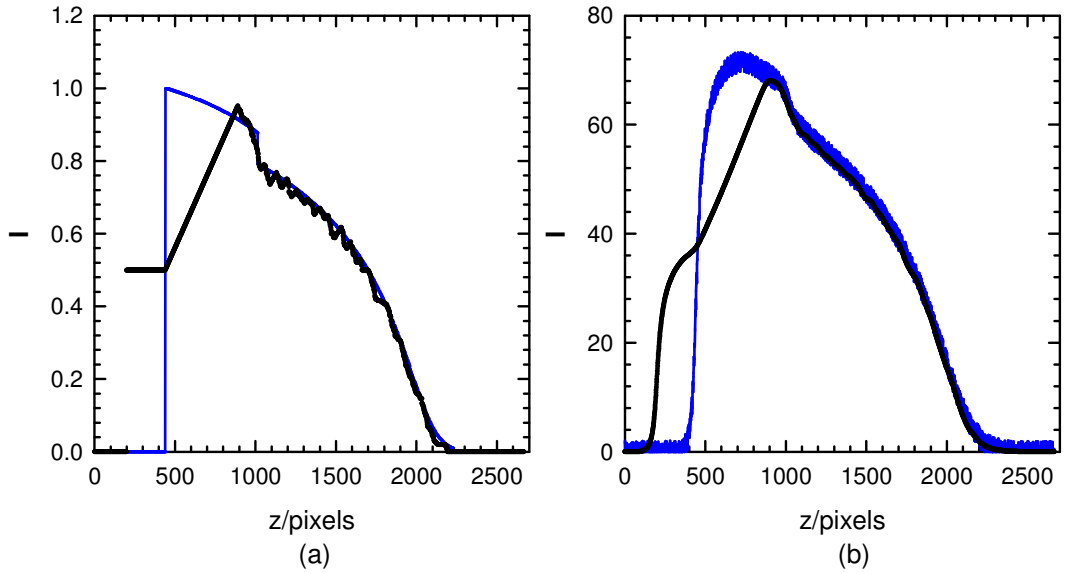

FIG. 3.11. Deconvolution approach: starting bin too low. (a) Theoretical intensity profile (blue line) and deconvoluted latent profile beginning on bin 200 (black line), and (b) convoluted theoretical profile with the addition of random noise (blue line) and convoluted latent profile fit to the convoluted theoretical profile (black line).

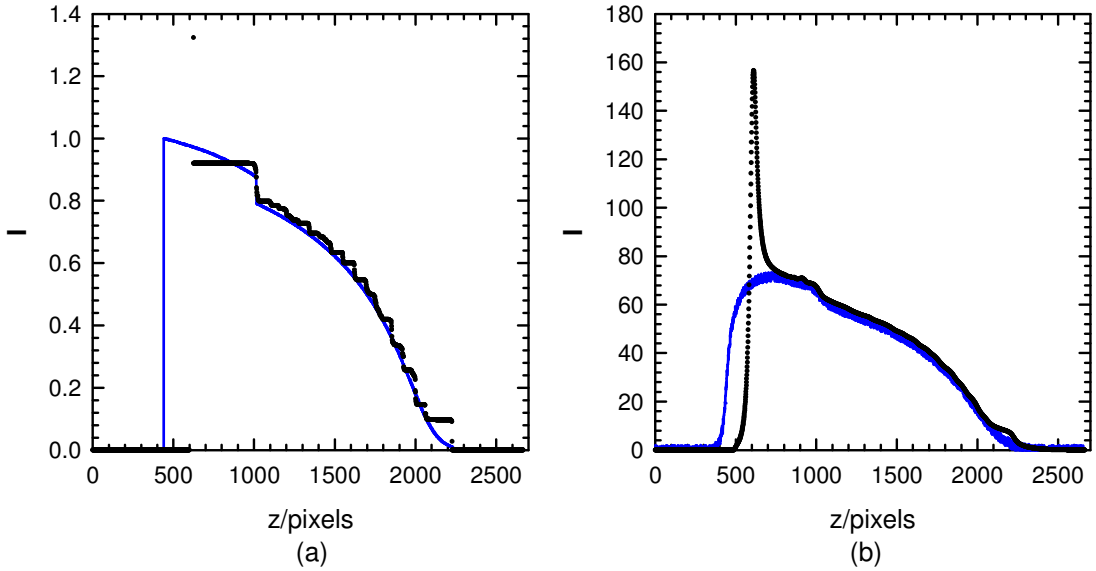

FIG. 3.12. Deconvolution approach: starting bin too high. (a) Theoretical intensity profile (blue line) and deconvoluted latent profile beginning on bin 600 (black line), and (b) convoluted theoretical profile with the addition of random noise (blue line) and convoluted latent profile fit to the convoluted theoretical profile (black line).

was identified as the starting value that minimized the total RMS error (Fig. 3.13). This starting bin corresponds to the bottom of the sedimentation cell in the experiment, and it closely matches the starting bin of 626 determined by fit of the theoretical profile to the data. Looking at the results for this starting bin (Fig. 3.14), it can be seen that the convoluted latent curve matches the experimental data. Further, the algorithm successfully suppresses the effects of random noise, as it did with the synthesized profiles. For the most part, the latent profile matches the theoretical profile. The discrepancies that exist are due to the lack of a sharp solid/fluid transition point in the latent curve. As a sharp transition was not observed in the experimental images, this lack of a sharp transition in the latent curve is considered correct. Otherwise, the latent curve closely matches the shape of the theoretical profile.

3.6 Summary

When locating particle centers, it is best to calculate a localized RMS error between a pattern of the particles' appearance and the image. Particle centers will be located by local minima in the RMS error data set. Computational time can frequently be reduced by first locating candidate centers using a less accurate method, such as a low pass filter in Fourier space. Also, the novel approach to deconvoluting data sets that has been presented in this section successfully reproduces the latent curve shape, and locates the start of the profile.

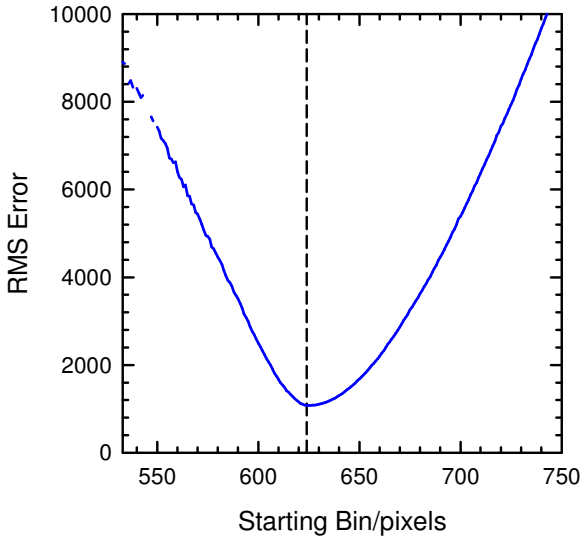

FIG. 3.13. Determination of the correct starting bin. Total RMS error between the convoluted latent curve and data as a function of latent curve starting bin, with the minimum error at bin 624 marked.

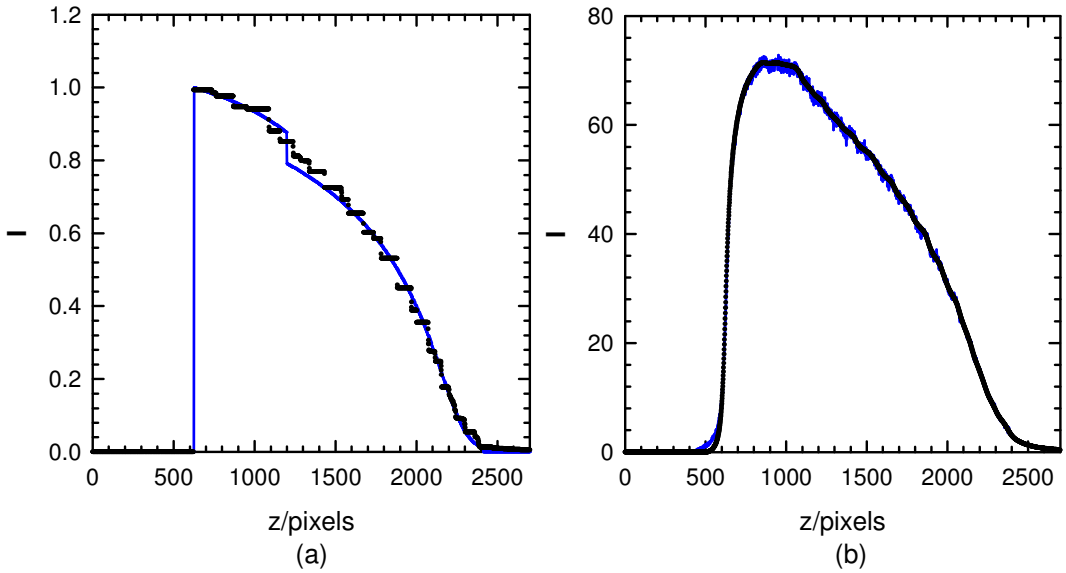

FIG. 3.14. Deconvolution results based on lowest RMS error starting bin. (a) Theoretical intensity profile previously fit to the data (blue line) and deconvoluted latent profile (black line), and (b) convoluted theoretical profile with the addition of random noise (blue line) and convoluted latent profile fit to the convoluted theoretical profile (black line).

4. PERTURBATION THEORY

4.1 Introduction

Due to its computational speed, it is convenient to use perturbation theory to plan experiments and to perform the initial analysis on experimental data. For example, in Section 5, the repulsive potential form of perturbation theory is fit to experimental data, and the parameters are then used to define the conditions for computationally expensive Monte Carlo experiments. As will be shown in the next subsection, there exists a body of literature covering the use of perturbation theory to calculate colloidal fluid/solid equilibrium in three-dimensional systems, and fluid properties in two-dimensional (2-D) systems. Unfortunately, the literature that was reviewed omitted some important details – most notably the equations used to calculate the Helmholtz free energy for some of the reference states – that made the implementation of perturbation theory from scratch particularly challenging.

To a large extent, this section is intended to be a practical guide for the implementation of perturbation theory. In addition to presenting the theory as described in literature, the issue of the reference state Helmholtz free energy is discussed. Specifically, this section demonstrates that it is satisfactory to derive this free energy from integration of the Fundamental Equation with the appropriate hard sphere or hard disk equation of state. Also, this section will explore some of the assumptions embedded in perturbation theory, and how those assumptions may lead to inaccuracies in the calculations. Finally, this section will cover the difficulty of applying perturbation theory to 2-D fluid/solid equilibrium.

Please note that this section addresses only the practical aspects of implementing perturbation theory for the purposes of predicted phase diagrams. Specifically, it presents the needed equations and data, and discusses successful strategies for importing these facets into a software package such as MathCAD. As the form of the equations for interparticle potentials do not immediately influence the practical aspects of the perturbation theory calculations, a detailed discussion of these forces has been avoided in this section. Such details are addressed in the later sections of this dissertation.

4.2 Literature Review and Theory

Perturbation theory has been used to predict the phase behavior of both repulsive and attractive colloidal systems, where the perturbed reference state is that of the hard sphere system.[94] While the predicted behaviors may not be as accurate as those obtained from other methods such as Monte Carlo simulations, the calculations are observed to be considerably faster. When applied to repulsive systems, such as those encountered in electrostatic stabilized colloidal dispersions, the perturbation theory takes the form of an effective diameter that is then applied to existing hard sphere equations.[94] When applied to systems with an attractive component to the interparticle potential, such as entropic depletion colloidal dispersions, the Barker-Henderson theory is used to calculate the Helmholtz free energy of the system.[94] The Helmholtz free energy is then used to determine the Gibbs free energy and the osmotic pressure, which in turn determine the phase behavior.[94]

4.2.1 Hard Sphere Reference State

In the review of perturbation theories, it is best to begin the discussion with the

reference state. In the hard sphere reference state, the interparticle potential (u_{HS}) as a function of particle-particle separation (r) is assumed to be infinite at contact, and zero at all other separations[95]

$$u_{HS}(r)/kT = \infty \text{ if } r \le d_p; \tag{4.1}$$

$$u_{HS}(r)/kT = 0 \text{ otherwise} \tag{4.2}$$

where d_p is the particle diameter. The important quantities for this reference state are the osmotic pressures, radial distribution functions, and Helmholtz free energies of the fluid and solid phases.[95] It is important to keep in mind that hard sphere systems do not exhibit a gas-liquid phase transition.[95] The osmotic pressure, $\Pi(\phi)$, for hard spheres depends only on the colloid volume fraction, ϕ, and is given in terms of the compressibility factor, $Z(\phi)$, as[94]

$$\Pi(\phi) = \rho kTZ(\phi) \tag{4.3}$$

$$\rho = N/V \tag{4.4}$$

$$\phi = V_p \rho \tag{4.5}$$

$$V_P = \frac{4}{3}\pi\left(\frac{d_P}{2}\right)^3 \tag{4.6}$$

where ρ is the number density of the particles, k is the Boltzmann constant, T is the absolute temperature, N is the total number of particles, V is the system volume, and V_p the particle volume. The hard sphere fluid compressibility factor, $Z_F(\phi)$, for concentrations from infinite dilution up to the freezing transition, ϕ_f=0.494, is given by[96]

$$Z_F(\phi) = \left(1 + \phi + \phi^2 - \phi^3\right) \cdot (1-\phi)^{-3} \tag{4.7}$$

and the hard sphere, face centered cubic solid compressibility factor, $Z_S(\phi)$, for concentrations from the melting transition, ϕ_m=0.545, up to close packing at ϕ_{cp}=0.74 is given by[97]

$$Z_S = 2.6 + 0.13\beta + 0.18\beta^2 - 1.1\beta^3 + 2.8\beta^4 - 2.9\beta^5 + 1.1\beta^6 + (12 - 3\beta)/\beta \quad (4.8)$$

where β=4(1-ϕ/ϕ_{cp}).

A paper by Gast et al.[95] does an excellent job outlining the equations needed for applying perturbation theory to three-dimensional systems. The radial distribution function of a hard sphere fluid [$g_{F,HS}(r,\phi)$] may be calculated using the Percus-Yevich equation[95]

$$g_{F,HS}(R,\phi) = \sum_{j=1}^{\infty} H\left(\frac{r}{2} - j\right) g_j(R,\phi) \quad (4.9)$$

$$\frac{R}{2} g_j(R,\phi) = \frac{(-12\phi)^{j-1}}{(j-1)!} \sum_{t=0}^{2} \lim_{t \to t_i} \frac{d^{j-1}}{dt^{j-1}} \left\{ (t - t_i)^j t \left(\frac{L(t,\phi)}{S(t,\phi)} \right)^j \exp\left[t\left(\frac{R}{2} - j \right) \right] \right\} \quad (4.10)$$

$$S(t,\phi) = (1-\phi)^2 t^3 + 6\phi(1-\phi)t^2 + 18\phi^2 t - 12\phi(1+2\phi) \quad (4.11)$$

$$L(t,\phi) = \left(1 + \frac{\phi}{2}\right) t + 1 + 2\phi \quad (4.12)$$

where H is the Heavyside function, R is distance in particle diameters, and t_i represents the zeros of $S(t,\phi)$. For more accurate results, the Percus-Yevich equation needs to be modified to be consistent with the virial theorem by the Verlet-Weis equations[98]

$$g_{F,HS-Corrected}(R,\phi) = g_{F,HS}[R_w(R,\phi), \phi_w(\phi)] + \delta g_1(R,\phi) \quad (4.13)$$

$$R_w(R,\phi) = \frac{R \cdot d_p}{d_w(\phi)} \tag{4.14}$$

$$d_w(\phi) = \sqrt[3]{\frac{d_p}{\phi}\phi_w(\phi)} \tag{4.15}$$

$$\phi_w(\phi) = \phi - \frac{\phi^2}{16} \tag{4.16}$$

$$\delta g_1(R,\phi) = 0 \text{ if } R < 1 \tag{4.17}$$

$$\delta g_1(R,\phi) = \left\{ \begin{array}{l} \left[\frac{A_w(\phi)}{R \cdot d_p}\right] \cdot e^{-\mu_w(\phi)\cdot\left(R\cdot d_p - d_p\right)} \\ \cdot \cos\left[\mu_w(\phi)\cdot\left(R\cdot d_p - d_p\right)\right] \end{array} \right\} \text{ otherwise} \tag{4.18}$$

$$\mu_w(\phi) = \frac{24 \cdot A_w(\phi)}{\phi_w(\phi)\cdot g_{HS,L}[1,\phi_w(\phi)]} \tag{4.19}$$

$$A_w(\phi) = \frac{3}{4} d_p \frac{\phi_w(\phi)^2 \cdot \left[1 - 0.7117\phi_w(\phi) - 0.114\phi_w(\phi)^2\right]}{[1-\phi_w(\phi)]^4} \tag{4.20}$$

where d_p is the particle diameter.

To calculate the hard sphere solid radial distribution function [$g_{S,HS}(R,\phi)$], the Kincaid and Weis equation is used[95]

$$g_{S,HS}(R,\phi) =$$

$$\left\{ \begin{array}{l} \frac{1}{R}\cdot\exp\left[-\left(w_1(\phi)^2\right)\cdot\left(R - R_1(\phi)\right)^2 - \left(w_2(\phi)^4\right)\cdot\left(R - R_1(\phi)\right)^4\right] \\ + \left(\frac{w_0[\phi]}{24\cdot\phi\cdot\sqrt{\pi}}\right)\cdot\sum_{i=2}^{20}\left[\left(\frac{n_i}{R\cdot R_i(\phi,i)}\right)\cdot\exp\left[-\left(w_0(\phi)^2\right)\cdot\left(R - R_i(\phi)\right)^2\right]\right] \end{array} \right\} \tag{4.21}$$

$$w_0(\phi) = \frac{1 - 10.5896(\phi_{cp} - \phi)^{2.543}}{[0.694(\phi_{cp} - \phi)]^{1.072}} \tag{4.22}$$

$$w_1(\phi) = \left[\frac{1.5523}{(\phi_{cp} - \phi)}\right] - 2.0303 \cdot \exp[5.8331(\phi_{cp} - \phi)] + 74.8732(\phi_{cp} - \phi)^2 \tag{4.23}$$

$$w_2(\phi) = \frac{0.95596 - 5.8550(\phi_{cp} - \phi) + 39.7466(\phi_{cp} - \phi)^2 - 109.6264(\phi_{cp} - \phi)^3}{\phi_{cp} - \phi} \tag{4.24}$$

$$R_i(\phi) = \frac{\sqrt{i}}{\left(\frac{\phi}{\phi_{cp}}\right)^{1/3}} \tag{4.25}$$

where n_i is the coordination number. The first twenty-one values (i = 0 to 20) of n_i are: 0, 12, 6, 24, 12, 24, 8, 48, 6, 36, 24, 24, 24, 72, 0, 48, 12, 48, 30, 72, and 24.[99] Also, $R_1(\phi)$ is not calculated from the formula for $R_i(\phi)$, but interpolated from the R_1 values of 0.94375, 0.98281, 1.00771, 1.0207, 1.0183, 1.0135, 1.0073, and 1.0026 for ϕ values of 0.52, 0.54, 0.56518, 0.6171, 0.65, 0.68, 0.71, and 0.73.[99] To force the Kincaid and Weis equation to conform to the virial theorem, the following correction is applied[95]

$$g_{S,HS-Corrected}(R,\phi) = 0 \text{ if } R < 1 \tag{4.26}$$

$$g_{S,HS-Corrected}(R,\phi) = A_k(\phi) \cdot g_{S,HS} \text{ otherwise} \tag{4.27}$$

$$A_k(\phi) = \frac{g_1(\phi)}{g_{S,HS}(1,\phi)} \tag{4.28}$$

$$g_1(\phi) = \frac{Z_S(\phi) - 1}{4 \cdot \phi} \tag{4.29}$$

In addition to these methods, the reference state radial distribution functions can

be estimated from NVT Monte Carlo simulation data.

The Helmholtz free energy for hard spheres (A_{HS}) is frequently broken up into its ideal gas component (A_{IG}) and an excess component (A_{EX})[100]

$$A_{HS} = A_{IG} + A_{EX} \tag{4.30}$$

The excess component for the fluid phase is[100]

$$\frac{A_{F,EX}}{NkT} = -\ln\left(\frac{\Pi}{\rho kT}\right) + \frac{(3-2\phi)}{(1-\phi)^2} - 3 \tag{4.31}$$

The Helmholtz free energy for the ideal gas, as well as for the hard sphere solid will be discussed in the next section, as expressions for these values did not appear to be explicitly stated in the literature reviewed.

4.2.2 Hard Disk Reference State

The interparticle potential for the 2-D hard disk reference state is the same as for the 3-D hard sphere system. But the loss of a dimension does result in some structural changes to the equations describing the thermodynamics of the system. As with hard spheres, the osmotic pressure, $\Pi(y)$, for hard disks depends only on the colloid area fraction, y, and is given in terms of the compressibility factor, $Z(y)$, as[101]

$$\Pi(y) = \rho_{HD} kTZ(y) \tag{4.32}$$

$$\rho_{HD} = N/A \tag{4.33}$$

$$y = A_P \rho_{HD} \tag{4.34}$$

$$A_P = \frac{\pi \cdot d_P^2}{4} \tag{4.35}$$

where ρ_{HD} is the number density of the particles, A is the system area, and A_P is the area

per particle or disk. The hard disk fluid compressibility factor, $Z_F(y)$, for concentrations from infinite dilution up to the freezing transition is given by either[101]

$$Z_F(y) = \frac{1}{(1-y)^2} + \frac{0.128y^2}{(1-y)^2} - \frac{0.043y^4}{(1-y)^3} \tag{4.36}$$

or[102]

$$Z_F(y) = \frac{\sum_{n=0}^{6} D_n y^n}{(1-y)^2} \tag{4.37}$$

where $D_0 = 1$, $D_1 = 0$, $D_2 = 0.128018$, $D_3 = 0.0018188$, $D_4 = -0.72553$, $D_5 = 2.52783$, and $D_6 = -2.4945$. The hard disk, face centered cubic solid compressibility factor, $Z_S(y)$, for concentrations from the melting transition up to close packing, $\rho_{HD,CP}$, is given by[102]

$$Z_S(y) = \frac{2}{\alpha(y)} + 1.90 + 0.67\alpha(y) \tag{4.38}$$

$$\alpha(y) = \frac{\rho_{HD,CP} - \rho_{HD}(y)}{\rho_{HD}(y)} \tag{4.39}$$

$$\rho_{HD,CP} = \frac{2}{d_P^2\sqrt{3}} \tag{4.40}$$

$$\rho_{HD}(y) = y/A_P \tag{4.41}$$

The close packed area fraction limit (y_{CP}) can be shown from geometric considerations to be 0.907.[103,104] However, there exists debate over the correct hard disk melting (y_m) and freezing (y_f) area fractions, with respective values of 0.686 and 0.723,[103] or 0.693 and 0.716[104] being reported. As a result, there will be some uncertainty as to the proper values to use when implementing perturbation theory with

the hard disk system as the reference state. Even so, it should be noted that selection of either the melting or freezing value will fix the value of the other, as a criterion for phase coexistence is equal osmotic pressures.[105]

4.2.3 Perturbing the Hard Sphere State

It is a straightforward matter to apply repulsive forces to perturbation theory. The interparticle force is first decomposed into the hard sphere component and the repulsive component (u_R):[94]

$$u(r) = u_{HS}(r) + u_R(r) \tag{4.42}$$

Next, the repulsive component is integrated to determine the effective particle diameter (d_{eff}):[94]

$$d_{eff} = d_p + \int_{d_p}^{\infty} \left[1 - \exp\left(\frac{-u_R(r)}{kT} \right) \right] dr \tag{4.43}$$

which is used to calculate the effective volume fraction (ϕ_{eff}):[94]

$$\phi_{eff} = \phi \left(\frac{d_{eff}}{d_p} \right)^3 \tag{4.44}$$

The effective volume fraction is the applied directly into the hard sphere equations of state.[94]

Application of attractive potentials is a more complicated matter, requiring calculation of the Helmholtz free energy from the Barker-Henderson theory[106]

$$\frac{A}{NkT} = \frac{A_{HS}}{NkT} + \frac{\rho}{2kT}\int u_A(r) g_{HS}(r) 4\pi r^2 dr$$
$$-\frac{\rho}{(2kT)^2}\int [u_A(r)]^2 \left(\frac{\partial \rho}{\partial \Pi}\right)_{HS} g_{HS}(r) 4\pi r^2 dr \qquad (4.45)$$
$$+ O\left[(kT)^{-3}\right] + \ldots$$

where u_A is the attractive component of the interparticle potential, g_{HS} is the hard sphere radial distribution function, $(\partial\rho/\partial\Pi)_{HS}$ is the hard sphere macroscopic compressibility, and $O[(kT)^{-3}] + \ldots$ represents the higher order terms of $(kT)^{-1}$. The repulsive portion of the interparticle potential is accounted for by calculating the parameters at the effective volume fraction as defined by Eq. (4.43). This expression was originally derived from a series expansion of the hard sphere configuration integral about the perturbed potential.[106] The macroscopic compressibility may be calculated from the appropriate hard sphere compressibility factor[95]

$$\left(\frac{\partial \rho}{\partial \Pi}\right)_{HS} = \left\{kT\left[Z_{HS} + \phi\left(\frac{\partial Z_{HS}}{\partial \phi}\right)\right]\right\}^{-1} \qquad (4.46)$$

With the Helmholtz free energy in hand, it is now possible to calculate the Gibbs free energy (G) and osmotic pressure of the attractive system[95]

$$\frac{G}{kT} = \frac{\partial}{\partial \rho}\left(\frac{\rho A}{kT}\right) \qquad (4.47)$$

$$\frac{\Pi}{kT} = \frac{\rho G}{kT} - \frac{\rho A}{kT} \qquad (4.48)$$

Phase coexistence, included gas-liquid coexistence, will occur when the Gibbs free energies and the osmotic pressures of two different volume fractions are equal.[105]

4.3 Results and Discussion

4.3.1 General Considerations

A number of general items need to be considered before proceeding to a detailed description of the actual implementation of perturbation theory for the calculation of colloidal phase diagrams. First and foremost, the issue of the Helmholtz free energy of the hard sphere reference state needs to be resolved. The literature reviewed made frequent reference to the hard sphere Helmholtz free energy, but appeared to not provide an expression or reference for its calculation. At most, the literature would note the equations of state used in the free energy calculations.[95] Review of thermodynamic texts also appeared to not provide explicit expressions for either the hard sphere or ideal gas Helmholtz free energy. Rather, only the classical relationships were stated. But the difficulty with the classical relationships is that they contain inherent assumptions that may or may not preclude the use of a given free energy expression in the perturbation theory calculations. As the hard sphere Helmholtz free energy is critical to the use of perturbation theory in attractive systems, this lack of specificity represents a significant hurdle to the researcher new to the field.

To resolve this dilemma, the exact Helmholtz free energy for an ideal gas will be derived from statistical thermodynamics and the ideal gas partition function. This expression will then be compared to the expressions derived from classical thermodynamics. While there may not be partition functions in convenient forms for hard disk and sphere fluids and solids, this comparison will allow for the selection of the appropriate classical thermodynamic expression to apply to the equations of state for the

hard disk and sphere reference states.

To begin, reference is made to the Helmholtz free energy in terms of the partition function (Q)[107]

$$A = -kT \ln Q \tag{4.49}$$

The partition function for an ideal gas (Q_{IG}) is[107]

$$Q_{IG} = \frac{1}{N!}\left(\frac{V}{\Lambda^3}\right)^N \tag{4.50}$$

where Λ is the particle thermal de Broglie wavelength, which can be express in terms of kT, Planck's constant (h), and an individual particle's mass (m)[107]

$$\Lambda = \frac{h}{\sqrt{2\pi mkT}} \tag{4.51}$$

Taking the natural log of the ideal gas partition function, and substituting into the definition for the free energy, the following expression is obtained

$$\frac{A_{IG}}{NkT} = -\ln\left[(kT)^{\frac{3}{2}}\frac{V}{N}\right] - \ln\left[\left(\frac{2\pi m}{h^2}\right)^{\frac{3}{2}} e\right] \tag{4.52}$$

where e is the root of the natural logarithm. For a system of identical particles, the second term can be treated as a constant (C_1)

$$\frac{A_{IG}}{NkT} = -\ln\left[(kT)^{\frac{3}{2}}\frac{V}{N}\right] + C_1 \tag{4.53}$$

The ideal gas Helmholtz free energy can also be derived from the internal energy definition (E)[107]

$$\left(\frac{\partial A/T}{\partial 1/T}\right)_{N,V} = E \tag{4.54}$$

The internal energy for an ideal gas is

$$E_{IG} = \frac{3}{2}NkT \tag{4.55}$$

Substituting this internal energy into the energy definition and integrating with respect to T^{-1} at constant N and V, the following expression is obtained

$$A_{IG} = -\ln\left((kT)^{3/2}\right) + C_2\big|_{N,V} \tag{4.56}$$

Comparison of this expression with the statistical mechanical result shows the two to be equivalent within an arbitrary constant, provided N and V are held constant. However, this approach is not suitable for the task at hand because application of the perturbation theory will require evaluating how the Helmholtz free energy changes with volume fraction – a function of both N and V.

Another route to derive the Helmholtz free energy is to rely on the Fundamental Equation[105]

$$dA = -SdT - \Pi dV + \mu dN \tag{4.57}$$

where μ is the chemical potential of the particles. Holding N and T constant, the Fundamental Equation simplifies to

$$dA = -\Pi dV\big|_{N,T} \tag{4.58}$$

Substituting in the ideal gas law and integrating, the result becomes

$$\frac{A_{IG}}{NkT} = -\ln(V) + C_3\big|_{N,T} \tag{4.59}$$

This expression is equivalent within an arbitrary constant to the statistical mechanical expression for constant N and T. While this approach does require that N be held constant, it allows for V to vary. As such, the results of this approach can be recast as functions of volume fraction. Further, while systems of varying temperature may be explored using perturbation theory, different phases will be assumed to be at the same temperature when determining coexistence. Thus, it is concluded that integrating the Fundamental Equation in conjunction with the hard disk and sphere fluid and solid equations of state is an acceptable approach for determining the reference state Helmholtz free energies.

The next item requiring consideration deals with the assumptions inherent in the perturbation theory equations, as deviations from these assumptions by a real-world system will be a source of inaccuracies in the results of the perturbation theory calculations. While the equations encompassing the perturbation theory discussed in this dissertation were originally derived from a series expansion, remarkably similar results can also be obtained using the internal energy definition of the Helmholtz free energy – provided appropriate assumptions are utilized. These are the assumptions that will be of interest to the current discussion. The derivation is begun by returning to the internal energy definition previously mentioned[107]

$$\left(\frac{\partial A/T}{\partial 1/T}\right)_{N,V} = E \tag{4.54}$$

The next task is to come up with an expression for the internal energy. This energy can be broken up into an ideal and an excess portion (E_{EX}), which for a 3-D fluid

takes the following form[107]

$$E_F = \frac{3}{2} NkT + E_{EX} \tag{4.60}$$

where E_{EX} can be expressed as function of interparticle potential, number density, particle separation, and the radial distribution function [$g(r)$][107]

$$E_{EX} = \frac{N}{2} \int_0^\infty u(r) \rho g(r) 4\pi r^2 dr \tag{4.61}$$

While the ideal term in Eq. (4.60) is specific to the gas phase, the excess term as described in Eq. (4.61) is applicable to both 3-D fluids and solids. A similar 2-D excess expression can also be derived by modifying Eq. (4.61) for integration over a 2-D differential ring, rather than a 3-D differential spherical shell. Plugging these expressions into Eq. (4.54), the following equation is obtained

$$\left(\frac{\partial A_F / T}{\partial 1/T} \right)_{N,V} = \frac{3}{2} NkT + \frac{N}{2} \int_0^\infty u(r) \rho g_F(r) 4\pi r^2 dr \tag{4.62}$$

where $g^f(r)$ is the fluid-phase radial distribution function. To solve for the Helmholtz free energy, the equation must be integrated with respect to T^{-1}. But the forms of $u(r)$ and $g(r)$ are unknown at this point. To proceed, two significant assumptions are required: (1) the interparticle potential is not a function of temperature; and (2) the radial distribution function may be approximated by the hard sphere radial distribution function. Incorporating these two assumptions and integrating, an estimate for the Helmholtz free energy is derived

$$\frac{A_F}{NkT} \approx -\frac{3}{2}\ln(T) + \frac{\rho}{2kT}\int_0^{\infty} u(r) g_{F,HS}(r) 4\pi r^2 dr + C_4\big|_{N,V} \tag{4.63}$$

where C_4 is a constant of integration. Because the derivation began with a derivative at constant N and V, the variability of the Helmholtz free energy with respect to volume fraction is buried in C_4. But this fact is not a problem for the current analysis, as both the ideal gas portion and the radial distribution function have been previously defined in terms of volume fraction. As such, the equation becomes

$$\frac{A_F}{NkT} \approx -\ln(V) + \frac{\rho}{2kT}\int_0^{\infty} u(r) g_{F,HS}(r) 4\pi r^2 dr + C_4\big|_{N,T} \tag{4.64}$$

This expression can be further reworked to approach the Baker-Henderson theory by breaking apart the interparticle potential into repulsive and attractive terms, and then combining the repulsive term with the ideal gas term. At this point a third assumption is made: that the particle interactions can be assumed to be hard sphere-like at separations less than the effective diameter as defined by Eq. (4.43). The expression now becomes

$$\frac{A_F}{NkT} \approx \frac{A_{F,HS}}{NkT} + \frac{\rho}{2kT}\int_{d_{eff}}^{\infty} u_A(r) g_{F,HS}(r) 4\pi r^2 dr + C_4\big|_{N,T} \tag{4.65}$$

where parameters such as $A_{F,HS}$ and $g_{F,HS}$ are determined using the effective volume fraction as defined by Eq. (4.43).

Comparing Eq. (4.45) and Eq. (4.65), it can be seen that the current expression resembles the Barker-Henderson theory with the exception of the higher order terms and a constant of integration. It is therefore possible to concluded that the following

assumptions are also embedded in Barker-Henderson theory calculations if the higher order terms that resulted from the series expansion are neglected: (1) the interparticle potential is not a function of temperature; (2) the radial distribution function can be approximated by the hard sphere radial distribution function; and (3) the repulsive component of the interparticle potential can be approximated by treated the particle interactions as hard sphere-like at interparticle center-to-center separations less than the effective diameter as defined by Eq. (4.43). Being aware of these assumptions now makes it possible to predict the situations where use of the Barker-Henderson theory may go awry, as well as propose possible solutions.

The first assumption – the independence of the interparticle potential from temperature – appears unlikely to pose a substantial risk to the use of perturbation theory for estimating phase behavior. The reason is that while it is possible to have interparticle potentials that vary with temperature,[108] a constant temperature is used when comparing different phases to determine which phase is the most thermodynamically stable for a given set of conditions. The third assumption – the reliance on the effective particle diameter to account for the repulsive aspects of the interparticle potential – could potentially impact the results. But as will be documented in a later section of this dissertation, a remarkable correspondence has been observed between phase behaviors calculated using the effective diameter approach and those predicted by NVT Monte Carlo simulations. Perhaps the second assumption – the use of the hard sphere radial distribution function – is the most dangerous. It is not hard to imagine how strong attractive forces could alter the separations sampled by the particles of an attractive

system. As such, care should be exercised when using perturbation theory to calculate the phase diagrams of attractive systems. Further, for strongly attractive systems, it may be possible to obtain more accurate results without repeating the series expansion of the configuration integral by simply using a radial distribution function determined using a potential closer to the potential of interest that the hard sphere potential.

4.3.2 Implementation

The first task that is required to implement perturbation theory is the calculation of the appropriate radial distribution function. Looking at Eq. (4.45), it can be seen that the radial distribution function is multiplied by either the interparticle potential, or the square of the interparticle potential, before integration to calculate the Helmholtz free energy. As a result, it is only necessary to calculate the radial distribution function out to the separation at which the interparticle potential goes to zero. Calculating the hard sphere radial distribution functions by Eqs. (4.9) - (4.20) for the fluid phase, and Eqs. (4.21) - (4.29) for the solid phase, was found to provide accurate results as compared to Monte Carlo simulation results. Unfortunately, this approach proved to be exceedingly computationally intense, especially when the values the Helmholtz free energy were required at multiple volume fractions to allow for determination of the Helmholtz free energy slope, as necessitated by Eq. (4.47).

To improve the amount of time required for calculations, and to allow extension of the procedure to two dimensional systems for which radial distribution function equations were not readily obtainable, the results of Monte Carlo simulations were used for the g(r) calculations. For both the fluid and solid phases, the radial distribution

functions were calculated at volume fraction intervals of 0.01, and radial separation intervals of 0.001 diameters. These data were then loaded into a reference table that the software program then used to calculate the Helmholtz free energies at the different volume fractions by multiplying the values by the appropriate potential value, and then numerically integrating over the range of separations. To allow for an accurate estimation of the slope of the Helmholtz free energy, an n-2 degree polynomial (where n is the number of volume fractions for which the Helmholtz free energy of the given phase had been calculated) was fit to the data. This polynomial was then differentiated for use in Eq. (4.47).

4.3.2.1 Reference State Equations

As previously noted, the differential form of the fundamental equation at constant N and T is used as the basis for deriving the reference state Helmholtz free energies:

$$dA = -\Pi dV\big|_{N,T} \tag{4.58}$$

To cast this equation into a more convenient form, dV is converted into $d\phi$, the osmotic pressure is replaced by the expression for the compressibility, and the equation is integrated:

$$V = \frac{NV_p}{\phi} \tag{4.66}$$

$$dV\big|_{N,T} = \frac{-NV_p}{\phi^2} d\phi \tag{4.67}$$

$$\Pi(\phi) = \frac{\phi}{V_p} NkTZ(\phi) \tag{4.68}$$

$$\frac{A}{NkT} = \int \frac{Z(\phi)}{\phi} d\phi + C \tag{4.69}$$

where C is a constant of integration. Replacing $Z(\phi)$ with the hard sphere fluid and solid equations of state, the hard sphere Helmholtz free energies are obtained:

$$\frac{A_{F,HS}}{NkT} = \ln(\phi) + \frac{2}{1-\phi} + \frac{1}{(1-\phi)^2} + C_{F,HS} \tag{4.70}$$

$$\begin{aligned} \frac{A_{S,HS}}{NkT} &= 2188\ln(\phi) - 3\ln(\phi - \phi_{cp}) - 14848\frac{\phi}{\phi_{cp}} + 20990\left(\frac{\phi}{\phi_{cp}}\right)^2 \\ &- 21071\left(\frac{\phi}{\phi_{cp}}\right)^3 + 13363\left(\frac{\phi}{\phi_{cp}}\right)^4 - 4813\left(\frac{\phi}{\phi_{cp}}\right)^5 + 751\left(\frac{\phi}{\phi_{cp}}\right)^6 + C_{S,HS} \end{aligned} \tag{4.71}$$

Using the hard disk equations of state, the hard disk Helmholtz free energies are derived:

$$\begin{aligned} \frac{A_{F,HD}}{NkT} &= \ln(y) - 5.413\ln(1-y) + \frac{0.438}{(1-y)} - 3.844y \\ &- 1.577y^2 - 0.82y^3 - 0.624y^4 + C_{F,HD} \end{aligned} \tag{4.72}$$

$$\frac{A_{S,HD}}{NkT} = -2\ln(A_P\rho_{HD,CP} - y) + 1.23\ln(y) - \frac{0.67A_P\rho_{HD,CP}}{y} + C_{S,HD} \tag{4.73}$$

To evaluate the constants of integration ($C_{F,HS}$, $C_{S,HS}$, $C_{F,HD}$, and $C_{S,HD}$), the Gibbs free energies for the fluid and solid states are calculated at the freezing and melting volume/area fractions, respectively. (Note that the osmotic pressures at the freezing and melting volume/area fractions should already be equal – if not, an adjustment to one or both values will be required.) Then, the integration constants are adjusted until the fluid

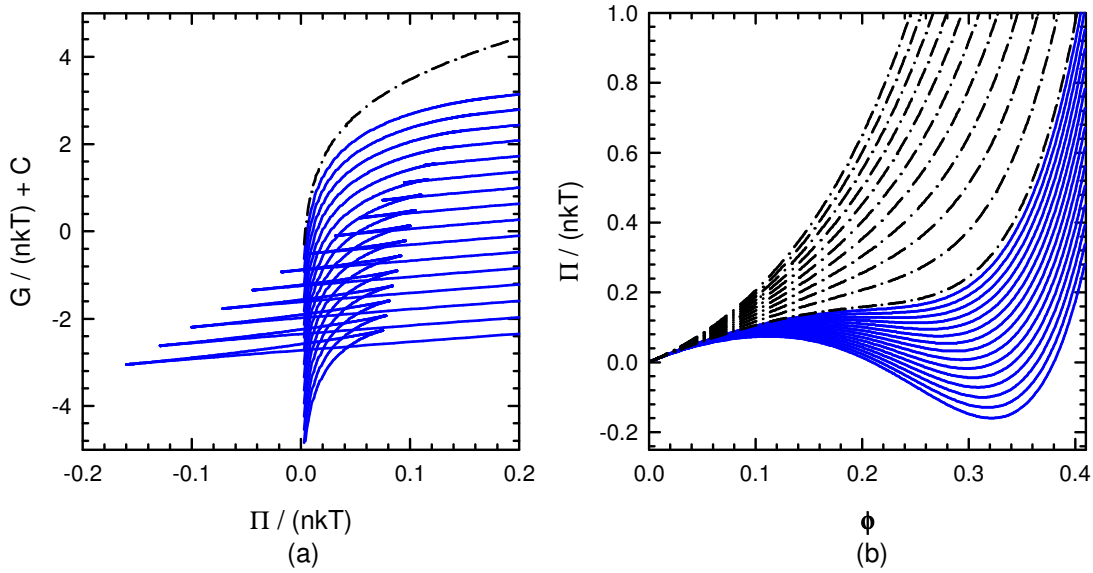

FIG. 4.1. Influence of increasing attraction on perturbation theory results. (a) Gibbs free energy versus osmotic pressure plot for an attractive system illustrating the effects of an increasing well depth from a hard sphere condition (black, dash-dot line) to -1kT to -1.3kT in 0.02kT steps (blue, solid lines) (note: each line has been offset by a constant to improve readability), and (b) Gibbs free energy versus volume fraction plot for the same system for an increasing well depth of hard sphere to -1kT in 0.1 kT steps (black, dash-dot lines) and -1.02kT to -1.3kT in 0.02 kT steps (blue, solid lines).

phase Gibbs free energy at freezing equals the solid phase Gibbs free energy at melting. As the absolute values of the Helmholtz free energies do not affect the calculations, the fluid constants of integration can be set to zero, thereby requiring the adjustment only of the solid constants of integration.

4.3.2.2 Perturbed Calculations

With the plots adjusted to return the appropriate reference state transitions, different potentials can now be evaluated using perturbation theory. As seen in Fig. 4.1, long-range potentials result in a looping of the fluid line, indicating gas/liquid coexistence. On the other hand, short-range potentials impact the solid line. In general, the range of the potential was observed to determine the osmotic pressure of same-phase

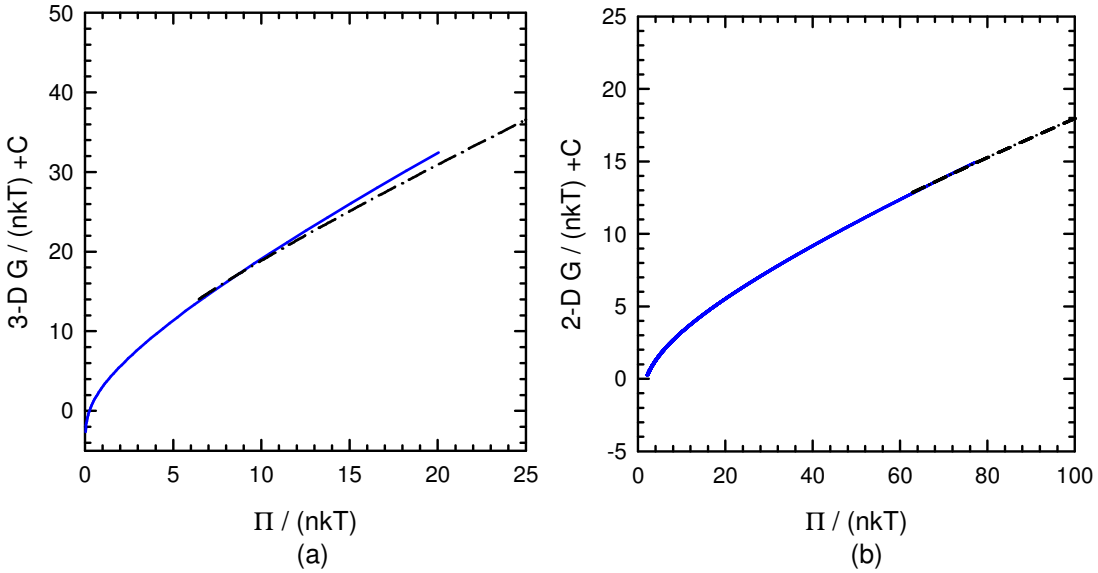

FIG. 4.2. Perturbation theory applied to 2-D and 3-D systems. (a) Gibbs free energy versus osmotic pressure plot for a 3-D hard sphere system illustrating a difference in slope between the fluid line (blue, solid) and the solid line (black, dash-dot), and (b) Gibbs free energy versus osmotic pressure plot for a 2-D hard disk system demonstrating a lack of difference between the fluid (blue, solid) and solid (black, dash-dot) lines.

(fluid/fluid or solid/solid) coexistence, while the depth of the potential controlled the magnitude of the effect.

Using perturbation theory as described in this section, it is possible to reproduce the phase diagrams for a three dimensional attractive system reported in literature[95]. Attempts to extend the use of perturbation theory to 2-D systems were not as successful. While the equations and general approach provided in this section were sufficient to generate fluid and solid hard disk Gibbs free energy versus osmotic pressure plots, the difficultly resided in the slopes of the two plots. As seen in Fig. 4.2, there is much less difference in the two slopes of the hard disk system than in the hard sphere system. This similarity, combined with ambiguity of the hard disk fluid/solid transition, made it difficult to determine the melting and freezing area fractions of a perturbed

system with any confidence. In fact, the behavioral similarity of the fluid and solid plots may be the source of the ambiguity surrounding the hard disk transition. Also, this difficulty may explain the apparent lack of use of perturbation theory for 2-D systems in literature.

4.4 Summary

For a 3-D attractive system, it is possible to reproduce phase diagrams reported in literature[95] using the approach and equations documented in this section. Specifically, the Helmholtz free energy reference states are determined by integration of the differential Helmholtz free energy form of the Fundamental Equation [Eq. (4.58)] at constant N and T, and substituting the osmotic pressure term with the appropriate equation of state. The radial distribution functions can be calculated by the Percus-Yevich equation as modified by the Verlet-Weis equations (fluid phase), and the modified Kincaid and Weis equation (solid phase). However, use of tabular data from Monte Carlo simulations proves to be a more computationally efficient approach. The Gibbs free energy versus osmotic pressure plots calculated from the Helmholtz free energies will need to be adjusted by an arbitrary constant to ensure the proper intersection location. The value of the arbitrary constant can be determined by the location of the hard sphere fluid/solid transition, which is documented in literature.[95]

This work also extended the use of perturbation theory into two dimensional systems, using the hard disk system as the reference state. Equations for the two dimensional fluid and solid radial distribution functions were not located in literature, but the necessary data were obtained by Monte Carlo simulations. The required

equations of state are provided by literature.[101,102] There exists some ambiguity about the freezing and melting volume fractions of the hard disk system.[103,104] This ambiguity, combined with the similarity of the slopes of the fluid and solid Gibbs free energy versus osmotic pressure plots, prevented the determination of phase transitions of perturbed systems to sufficient precision to justify the use of perturbation theory for the calculation of phase diagrams of two dimensional systems.

5. SEDIMENTATION PROFILES*

5.1 Introduction and Literature Review

Colloidal sedimentation equilibrium has been a topic of fundamental scientific interest since the early development of statistical mechanics and verification of the discontinuous nature of matter by Perrin.[109,110] More recently, there is renewed interest in sedimentation equilibrium because of its relevance to assembly of colloidal precursors (e.g. 0.1-10μm particles) into interfacial 3-D microstructured materials.[111,112] Understanding interfacial sedimentation equilibrium is directly relevant to intelligently designing, controlling, and optimizing self assembly of interfacial colloidal microstructures with explicit consideration of relevant interactions between colloids, surfaces, and external fields. Although colloidal assembly processes do not in general occur along, or terminate in, equilibrium states, low Peclet number dynamic processes are highly influenced by equilibrium pathways, and in the case of colloidal crystal assembly, the global free energy minimum configuration (i.e. single perfect crystal) is the desired final state. Now with modern optical microscopy tools significantly more advanced those used by Perrin, it is now possible to confidently measure and manipulate sedimentation equilibrium profiles to create technologically useful interfacial colloidal based microstructures.

For the dilute, bulk colloids fluids like those investigated by Perrin,[109,110] sedimentation equilibrium density profiles, $\rho(z)$, are accurately modeled using

---

* The material presented in this section was originally published in R. E. Beckham and M. A. Bevan, J. Chem. Phys. **127**, 164708 1-13 (2007), copyrighted by the American Institute of Physics (AIP). The abstract permalink is http://link.aip.org/link/?JCPSA6/127/164708/1.

$$\rho(z) = \rho_0 \exp\left[-\varphi_g(z)/kT\right] \tag{5.1}$$

where ρ_0 is the number density at zero elevation, and the gravitational potential, $\varphi_g(z)$, relative to the thermal energy, kT, is given by

$$\varphi_g(z)/kT = z/l_g \tag{5.2}$$

$$l_g = kT/G \tag{5.3}$$

where G is the buoyant colloid weight. The characteristic length scale, l_g, over which $\rho(z)$ is inhomogeneous reflects the relative competition between entropy, which favors uniform distributions, and gravity, which favors increased concentrations at low elevations. Eq. (5.1) is valid for ideal gases at any concentration and for realistic colloids approaching infinite dilution [including colloid-surface interactions in $\varphi(z)$[15,113]]. In realistic colloid dispersions at finite concentration, colloid and surface potentials due to hard core, van der Waals, electrostatic, and macromolecular interactions produce sedimentation equilibrium profiles quite different from Eq. (5.1).

Theoretical and simulation studies have attempted to model realistic sedimentation equilibrium profiles for a broad range of parameters including different particle interactions, shape, size, concentrations, and mixtures. Examples of such investigations include the treatment of sedimentation equilibrium problems involving hard sphere fluids,[114] attractive particles,[115,116] rod shaped particles,[117] binary mixtures,[118] and coexisting phases.[119,120] In addition to including realistic colloidal interactions, several studies have also considered the role of colloid-surface interactions in altering sedimentation equilibrium profiles, particularly in the case of interfacial

crystallization.[121] A number of modeling efforts have also explored possible roles of charge gradients within sedimentation equilibrium profiles consisting of electrostatically stabilized colloids.[122-124] Many theoretical studies compare predictions against density profiles obtained via Monte Carlo or molecular dynamic simulations due to the limited resolution and range of conditions explored in most sedimentation equilibrium measurements.

Measurements of colloidal sedimentation equilibrium profiles include the pioneering optical microscopy measurements of Perrin[109,110] and then others,[125,126] which used dilute samples and avoided wall effects. Other sedimentation equilibrium profile measurements have employed direct physical sampling,[127] light scattering,[128] X-ray based methods,[129] and most recently confocal microscopy.[130] Such experimental studies have been concerned with confirming the hard sphere equations of state,[127-129] quantifying electrostatic colloidal crystal modulii,[131] understanding the behavior of disk shaped particles,[132] and exploring whether an electrostatic sedimentation potential exists for electrostatically stabilized colloids.[128,133,134] More recent microscopy measurements have begun to characterize real-space microstructures on the scale of ~10 particle diameters for micron sized colloids with a focus on interfacial crystallization.[28,146-148] In general, measurements include either macroscopic density profiles of submicron sized colloids or microscopic density profiles of micron sized colloids near surfaces.

This section reports the development of an intensity based confocal scanning laser microscopy (CSLM) method to characterize fluid and coexisting fluid-solid sedimentation equilibrium profiles near underlying planar surfaces. The approach

involves averaging vertical image slices of fluorescent core-shell silica colloids to produce fluorescence emission intensity profiles that are converted to quantitative colloid density profiles by accounting for absorbance, emission efficiency, and single particle intensity profiles. The motivation for the developing this method is to rapidly characterize density profiles over dimensions of ~100σ (σ is colloid diameter), which occurs when $l_g/\sigma \approx 1$. The intensity based CSLM method offers several advantages including capabilities to: (1) quantify profiles without locating colloid centers in large imaging volumes and in the presence of significant Brownian motion, (2) exploit relatively fast profile equilibration times for submicron colloids via their increased self diffusion rates, (3) simultaneously identify real-space microstructures (e.g. fluid, crystal, glass, gel, etc.) and interfaces between phases, and (4) rapidly acquire profiles to enable measurements of transport, fluctuations, and transients.

The results include measured sedimentation equilibrium profiles for: (1) a relatively dilute interfacial fluids, (2) a concentrated interfacial colloidal fluid near interfacial crystallization conditions, (3) and a profile displaying fluid-solid coexistence. In each case, experimental measurements are compared with predictions based on a local density approximation perturbation (LDAP) theory[94,135] and Monte Carlo (MC) simulations.[136] Excellent agreement is obtained between experiment, theory, and simulation for the fluid and fluid-solid coexistence profiles with the exception of the onset of interfacial crystallization in the concentrated fluid case and the exact elevation of the fluid-solid interface in the coexistence case. Our findings demonstrate intensity based CSLM method as a useful approach to characterizing interfacial colloidal

sedimentation equilibrium profiles and suggest its broader utility for measuring 3-D colloidal interactions, dynamics, and structure as a complement to existing particle tracking based microscopy experiments.[24,127,151,152]

5.2 Theory

5.2.1 Colloidal, Surface, and Gravitational Potentials

The net potential energy, $U(r, z)$, for a colloidal particle in a gravitational field near an underlying surface is the sum of pairwise colloidal potentials, $u(r)$, and external potential energy contributions, $\varphi(z)$, given as

$$U(r,z) = \sum u(r) + \varphi(z) \tag{5.4}$$

$$\varphi(z) = \varphi_{pw}(z) + \varphi_g(z) \tag{5.5}$$

where $\varphi_{pw}(z)$ is the colloid-wall pair potential, $\varphi_g(z)$ is potential energy due to gravity in Eq. (5.2), r is center-to-center separation between colloids, and z is the colloid center-to-wall surface separation. For conditions where only DLVO electrostatic interactions are important, the pair potentials are given as[94]

$$u(r) = B_{pp} \exp[-\kappa(r-2a)] \tag{5.6}$$

$$\varphi_{pw}(z) = B_{pw} \exp[-\kappa(z-a)] \tag{5.7}$$

where B_{pp}, B_{pw}, and the inverse Debye length, κ, are given by

$$B_{pp} = 32\pi\varepsilon a\left(\frac{kT}{ze}\right)^2 \tanh\left(\frac{ze\psi_p}{4kT}\right)\tanh\left(\frac{ze\psi_p}{4kT}\right) \tag{5.8}$$

$$B_{pw} = 64\pi\varepsilon a\left(\frac{kT}{ze}\right)^2 \tanh\left(\frac{ze\psi_p}{4kT}\right)\tanh\left(\frac{ze\psi_w}{4kT}\right) \tag{5.9}$$

$$\kappa = \left[\frac{\sum e^2 z_i C_i N_A}{\varepsilon k T} \right]^{1/2} \tag{5.10}$$

where ε is the solvent dielectric permittivity, k is Boltzmann's constant, T is absolute temperature, e is the elemental charge, ψ_p and ψ_w are the colloid and wall Stern potentials, C_i is the bulk electrolyte concentration of species i, z_i is the valence of species i, and N_A is Avogadro's number. The buoyant colloid weight, G, in Eq. (5.2) is given by

$$G = mg = V_p \Delta\rho g = (4/3)\pi a^3 (\rho_p - \rho_f) g \tag{5.11}$$

where V_p is the colloid volume, $\Delta\rho$ is the difference between the particle, ρ_p, and fluid, ρ_f, densities, and g is acceleration due to gravity.

5.2.2 Equilibrium Phase Behavior

The osmotic pressure, $\Pi(\phi)$, for hard sphere colloids depends only on the colloid volume fraction, ϕ, and is given in terms of the compressibility factor, $Z(\phi)$, as[94]

$$\Pi(\phi) = \rho k T Z(\phi) \tag{5.12}$$

$$\rho = N/V \tag{5.13}$$

$$\phi = V_p \rho \tag{5.14}$$

where the hard sphere fluid compressibility factor, $Z_F(\phi)$, for concentrations from infinite dilution up to the freezing transition, ϕ_f=0.494, is given by[96]

$$Z_F(\phi) = \left(1 + \phi + \phi^2 - \phi^3\right) \cdot (1 - \phi)^{-3} \tag{5.15}$$

and the hard sphere, face centered cubic solid compressibility factor, $Z_S(\phi)$, for concentrations from the melting transition, ϕ_m=0.545, up to close packing at ϕ_{cp}=0.74 is

given by[97]

$$Z_S = 2.6 + 0.13\beta + 0.18\beta^2 - 1.1\beta^3 + 2.8\beta^4 - 2.9\beta^5 + 1.1\beta^6 + {(12-3\beta)}/{\beta} \quad (5.16)$$

where β=4(1-ϕ/ϕ_{cp}). These hard sphere expression can be adapted to colloids interacting via the electrostatic repulsion in Eq. (5.6) by computing an effective colloid size, $2a_{eff}$, as[135]

$$2a_{eff} = 2a + \int_{d_p}^{\infty} \left[1 - \exp\left(\frac{-u_R(r)}{kT}\right)\right] dr \quad (5.17)$$

and an effective volume fraction, ϕ_{eff}, as

$$\phi_{eff} = \phi\left(\frac{a_{eff}}{a}\right)^3 \quad (5.18)$$

which can be used in Eqs. (5.12) - (5.16).[94]

5.2.3 Colloidal Sedimentation Equilibrium

For isothermal equilibrium conditions, the differential change in Π with differential change in elevation, z, is given as

$$\frac{\partial \Pi}{\partial z} = -G\rho(z) \quad (5.19)$$

where the chain rule can be used to twice to give

$$\frac{\partial \Pi}{\partial z} = \frac{\partial \Pi}{\partial \phi}\frac{\partial \phi}{\partial z} = \left(\frac{\partial \Pi}{\partial \rho}\frac{\partial \rho}{\partial \phi}\right)\frac{\partial \phi}{\partial z} \quad (5.20)$$

which can be rearranged with substitutions from Eqs. (5.14) and (5.19) as

$$\frac{\partial \phi}{\partial z} = -\left(\chi / l_g\right)\phi(z) \quad (5.21)$$

where the reduced osmotic compressibility, χ, is given by

$$\chi = kT\left(\frac{\partial \Pi}{\partial \rho}\right)^{-1} \tag{5.22}$$

Eq. (5.12) can then be integrated to relate z and ϕ as

$$z(\phi) = z_0 - l_g \int_{\phi_0}^{\phi} (\chi\phi)^{-1} d\phi \tag{5.23}$$

where z_0 and ϕ_0 are a reference elevation and concentration, and χ can be obtained for effective hard sphere fluids and solids using Eqs. (5.12) - (5.18) and (5.22). For coexisting fluid and solid phases, Eq.(5.23) is modified using the fluid, χ_F, and solid, χ_S, reduced osmotic compressibilities as

$$z(\phi) = z_0 - l_g \left[\int_{\phi_0}^{\phi_m} (\chi_S \phi)^{-1} d\phi + \int_{\phi_f}^{\phi} (\chi_F \phi)^{-1} d\phi \right] \tag{5.24}$$

where Eqs. (5.23) and (5.24) can both easily be plotted as $\phi(z)$ curves.

5.2.4 Density and Intensity Profiles

Particle concentration profiles, $\phi(z)$, can be obtained from CSLM measured intensity profiles, $I(z)$, by exploiting the proportionality between fluorescence emission intensity, $I_{em}(z)$, and local fluorophore concentration as

$$I_{em}(z) = \Omega\phi(z) I_{exc}(z) + I_b \tag{5.25}$$

where Ω is the fluorophore quantum yield per colloid volume fraction, I_b is a constant background intensity, and $I_{exc}(z)$ is the excitation laser intensity, which is attenuated at a given elevation due to intervening fluorophore as given in the differential form of Beer's

law as

$$dI_{exc} / dz = -\alpha\phi I_{exc} \tag{5.26}$$

which can be integrated including the inhomogeneous sedimentation equilibrium profile to give

$$I_{exc}(z) = I_0 \exp\left[-\alpha \int_{z_0}^{z} \phi(z) dz \right] \tag{5.27}$$

where I_0 is the incident laser intensity, and α is the absorbance per colloid volume fraction. Instrument specific spatial resolution limitations (including effects of the diffraction limit and confocal optics captured in the point spread function) also influence the shape of $I(z)$, which can be accounted for by convoluting with the single colloid intensity profile, $I_{sp}(z)$, as

$$I(z) = \int I_{sp}(\zeta) I_{em}(z - \zeta) d\zeta \tag{5.28}$$

5.3 Materials and Methods

5.3.1 Fluorescent Colloid Preparation

Toluene, potassium hydroxide, 18M sulfuric acid, 29.35% ammonium hydroxide, calcium oxide, and calcium carbonate were purchased from Fisher Scientific. Tetraethyl orthosilicate (TEOS), N,N-dimethylformamide (DMF), (3-aminopropyl)triethoxysilane (APS), and H_2O_2 (35%) were purchased from Sigma-Aldrich. Ethanol (200 proof) was purchased from Aaper Alocohol, and succinimidyl 6-(*N*-(7-nitrobenz-2-oxa-1,3-diazol-4-yl)amino) hexanoate (NBD-X SE) was purchased from Molecular Probes. All chemicals were used as supplied without further purification, except for TEOS, which

was treated with the calcium oxide, vacuum distilled in the presence of calcium carbonate, and refrigerated under nitrogen.

Fluorescent SiO_2 colloids were prepared using the Stöber method to prepare nominal 400nm SiO_2 cores,[21] followed by incorporation of NBD-X SE fluorophore into an organosilica layer,[24] and capping with a nominal 160nm non-fluorescent SiO_2 shell.[22] Following synthesis, fluorescent SiO_2 colloids were washed by repeated sedimentation, supernatant replacement, and redispersion first in ethanol and then DMF. The colloid diameter was characterized as $2a$=719±5nm from dynamic light scattering in ethanol (Brookhaven Instrument Corp., Holtsville, NY) and from the location of the first peak in a 2-D radial distribution function for a dried, crystalline monolayer. After redispersion in DMF, fluorescent SiO_2 colloids were index matched via toluene addition and turbidity minimization at 633nm[51] beyond the NBD-X SE fluorophore excitation maximum (λ_{exc}=470nm, λ_{em}=540). The final DMF to toluene ratio was 1:1.58 on a volumetric basis (assuming ideal mixing). The index matched solvent media density was measured directly on a microbalance for known volumes as 0.92g/cm^3 in excellent agreement with literature measurements.[137] The solvent mixture refractive index, n, and dielectric permittivity were determined via the Clausius-Mossotti mixing rule as (with $x=n^2$ or $x=\varepsilon$)

$$\frac{x_{12}-1}{x_{12}+2}=\phi_1\frac{x_1-1}{x_1+2}+\phi_2\frac{x_2-1}{x_2+2} \tag{5.29}$$

5.3.2 Sedimentation Experiments

Sedimentation cells were assembled using a 18mm x 18mm x 175μm coverslip as a substrate, a 450μm silicon wafer with up to four ~1mm holes as separate cells, and a

standard 25mm x 75mm x 1mm microscopes slides that functioned as a cover with drilled injection ports. Each of these layers was held together by polydimethylsiloxane cured in an oven at 60C for 12hrs. During sedimentation equilibrium experiments, fluorescent SiO_2 colloidal dispersions were injected into each cell and injection ports were covered with an 18mm x 18mm x 175μm coverslip sealed at its edges with vacuum grease. Sedimentation cells were leveled on a three point stage and equilibrated in a constant temperature closet for at least 24 hours, which was conservatively longer than the ~6 hour period required for equilibration in temporal control experiments. Equilibrated samples were re-leveled on the microscope stage and re-equilibrated at constant temperature for one to two hours prior to confocal microscopy measurements.

5.3.3 Confocal Microscopy

Confocal scanning laser microscopy (CSLM) experiments used a Zeiss LMS 5 PASCAL scanner on an Axiovert 200M inverted microscope. The objective was a Zeiss a 100× (NA=1.4) oil-immersion objective. The confocal pinhole was set to 1 Airy unit for all images. The excitation source was a 488nm line on a 500 mW Argon ion laser. Vertical scan images were collected in a fast mode (~2sec to scan 100μm) at 2048 x 2000 pixels with pixel dimensions of 45nm x 45nm and a pixel scan time of 0.64μs. Horizontal scan images were collected at 2048 x 2048 pixels with pixel dimensions of 9.0nm x 9.0nm and a pixel scan time of 0.64 μs. The CSLM instrument and condition specific $I_{sp}(z)$ [for use in Eq. (5.28)] was averaged over many single fluorescent colloids dried onto a quartz coverslip and backfilled with same DMF-toluene index matching solvent media used in all experiments.

Approximately 30 CSLM images obtained at different times and locations in sedimentation cell were averaged over 2048 vertical intensity curves per image to obtain intensity profiles for analysis as density profiles. This approach was used to confirm equilibration of density profiles via the equivalence of temporal and spatial averages. Constant background intensities, I_B, were subtracted from each intensity curve before aligning all curves via an rms error minimization algorithm and then averaging pixel intensities at the same elevations. CSLM horizontal scans of the sediment immediately adjacent to the wall were performed following vertical measurements since structural information from such images did not rely on quantitative intensity information that could be influenced by photobleaching during CSLM vertical scans. Radial distribution functions were generated from colloid centers located in CSLM horizontal scans using a low pass Fourier transform noise filter followed by standard intensity centroid identification algorithms coded in Fortran.[85]

5.3.4 Intensity and Density Profiles

Experimental and theoretical $I(z)$ and $\phi(z)$ curves were compared by (1) predicting $\phi(z)$ using the LDAP theory in Eqs. (5.4) - (5.24), (2) convoluting $\phi(z)$ using Eqs. (5.25) - (5.28) to obtain a predicted $I(z)$, (3) iterating predictions of $\phi(z)$ to minimize the root mean square difference between the experimental and theoretical $I(z)$ curves. All parameters in Eqs. (5.4) - (5.24) were fixed based on independent measurements reported in Table 5.1 with the exception of ρ_p, κ, and ϕ_0. Initial values were chosen for (1) ρ_p as 2000kg/m^3 based on the density of standard Stober silica without added fluorophore,[21] (2) κ^{-1} as 20% of the colloid surface separations from projected 2-D radial

Table 5.1. Parameters used in LDAP theoretical fits and MC simulations to CSLM measured intensity and density profiles. Adjustable parameters are shown in bold. All other parameters were fixed from independent measurements described in the footnotes.

	Eq.	Fig. 5.2	Fig. 5.3	Fig. 5.4
$\alpha(\mathrm{mm}^{-1})$[a]	(5.27)	87	87	87
$\Omega(10^{-3})$[a]	(5.25)	17.6	17.6	17.6
n[b]	· · ·	1.47	1.47	1.47
ε[b]	(5.8) - (5.10)	4.67	4.67	4.67
$-\psi_p(\mathrm{mV})$[c]	(5.8), (5.9)	40.0	40.0	40.0
$-\psi_w(\mathrm{mV})$[c]	· · ·	40.0	40.0	40.0
$\kappa^{-1}(\mathrm{nm})$	(5.6), (5.7)	**17.9**	**17.9**	**28.9**
$C(\mu\mathrm{M})$[d]	(5.10)	17.0	17.0	6.6
$\rho_f(\mathrm{g/cm}^3)$[e]	· · ·	0.92	0.92	0.92
$\rho_p(\mathrm{g/cm}^3)$	(5.11)	**1.75**	**1.75**	**1.75**
ϕ_0[f]	(5.23), (5.24)	**0.28**	**0.43**	**0.40**
$2a_{eff}(\mathrm{nm})$[g]	(5.17)	790	790	840
$\phi_{0,eff}$[h]	(5.18)	0.37	0.57	0.63
$\phi_{A,0}$[i]	· · ·	0.53	0.56	0.62
$\phi_{A,0,eff}$[j]	· · ·	0.64	0.68	0.84

[a]Control measurements of homogeneous crystals in deep sediments.
[b]Clausius-Mossitti mixing rule and literature results.[137]
[c]Zeta potential measurements.
[d]1:1 electrolyte concentration inferred from fit Debye lengths.
[e]Density measurements and literature results.[137]
[f]Core colloid volume fraction at bottom wall.
[g]Effective particle diameter.
[h]Effective colloid volume fraction at bottom wall.
[i]Core colloid area fraction at bottom wall.
[j]Effective colloid area fraction at bottom wall.

distribution function, $g(r)$, for the first fluid layer (within $2a$ of the surface), and (3) ϕ_0 (core colloid volume fraction) based on the core colloid radius, a_{core}, the location of the first peak in $g(r)$ at $r=R$, and the relationship,

$$\phi_{core} = \left(\pi/3\sqrt{2}\right)\left(a_{core}/R\right)^3 \tag{5.30}$$

which converts the 2-D colloid spacing to a 3-D volume fraction based on spacing in the 111 plane of an FCC crystal (which was used whether crystals were present or not as an initial guess).

Interconversion of $I(z)$ and $\phi(z)$ curves using Eqs. (5.25) - (5.28) required independent control experiments to determine the absorbance, α, per colloid concentration and pathlength and an effective Ω that incorporates the fluorophore quantum yield, amount of fluorophore per colloid, finite depth of field, and a renormalization to give $I(z)=1$ for $\phi(z)=0.74$. Measurements were performed on a homogeneous, single domain crystal compressed under a ~1mm deep sediment.[131] By measuring R=823nm from the first layer $g(r)$, the core colloid volume fraction, ϕ_{core}, was computed using Eq. (5.30) as $\phi_{core}=0.49=(0.74)(719\text{nm}/823\text{nm})^3$. Table 5.1 reports values of α and Ω used to analyze all data in this work based on their common preparation from the same particle batch. Photobleaching was minimized by reducing the excitation laser power until normalized intensity profiles were independent of their lateral location within a sample to indicate a constant Ω value.

5.3.5 Monte Carlo Simulations

Allen and Tildesley's canonical (NVT) Monte Carlo (MC) code was used for all

simulations.[136] Simulation boxes were infinitely high in the direction of gravity and normal to an underlying wall surface. Periodic boundary conditions were used in the direction parallel to the underlying surface with two box sizes of either 13.9*a* x 13.9*a* (5μm x 5μm) or 19.1*a* x 16.6*a* (13.8μm x 11.9μm). The number of colloids per wall surface area, *N*/*A*, in each MC simulation was determined integrating the experimental density profiles as

$$N/A = \int_0^\infty \rho(z)dz \tag{5.31}$$

which was multiplied by the simulation box area to determine the absolute number of colloids in a given MC simulation. The number of particles in the small and large boxes was 526 and 863 for the dilute fluid case, 1820 and 2987 for the concentrated fluid case, and 2510 and 4120 for the fluid-solid coexistence case. Equilibration was achieved in all MC simulations using a procedure where an expanded FCC lattice of approximately the same total elevation as the density profile of interest was first allowed to melt in the absence of gravity and was then allowed to equilibrate for 0.5g and then finally 1g.[138] Density profiles were average over 10^4 independent MC configurations following equilibration. MC generated configurations were rendered using POV-Ray.

5.3.6 Bond Order Parameter

A local 2-D bond orientational order parameter, ψ_6, was computed for each colloid in MC simulated density profiles based on the configuration of adjacent particles within layers parallel to the underlying wall surface using

$$\psi_6 = \left| \frac{1}{6} \sum_k \exp(6i\theta_k) \right| \tag{5.32}$$

where k is an index over colloids within the first coordination shell around each colloid, and θ_k is angle between the colloid of interest and neighboring colloids relative to an arbitrary reference angle.[139] Because local bond order parameters are somewhat insensitive, Eq. (5.32) was only applied to colloids with 6 neighboring colloids within $2.72a_{eff}$ in the radial direction parallel to the underlying wall surface and $\pm a_{eff}$ in the normal direction. The use of a 2-D order parameter is not intended to imply that 2-D order necessarily precedes 3-D crystallization,[140] but rather a 2-D parameter is expected to be sufficient to detect the onset or order within 111 layers parallel to the substrate that arise from coupled lateral packing, vertical consolidation, and layer registration. A 3-D parameter would be required to monitor crystallization in planes oriented in directions other than parallel to the substrate. A continuous 8bit green-blue scale was used in MC renderings to capture the ψ_6 value for each particle with green corresponding to ψ_6=0 and blue corresponding to ψ_6=1.

5.4 Results and Discussion

5.4.1 Interfacial Intensity and Density Profiles

Fig. 5.1 shows real space CSLM measurements and MC simulations of interfacial colloidal sedimentation equilibrium profiles of 720nm fluorescent silica colloids in index matching DMF/toluene solvent media. Because the gravitational length scale ($l_g \approx 2.6\mu m$) is somewhat greater than the particle dimensions ($\sigma = 2a = 720nm$) but of a similar magnitude, the inhomogeneous sedimentation equilibrium

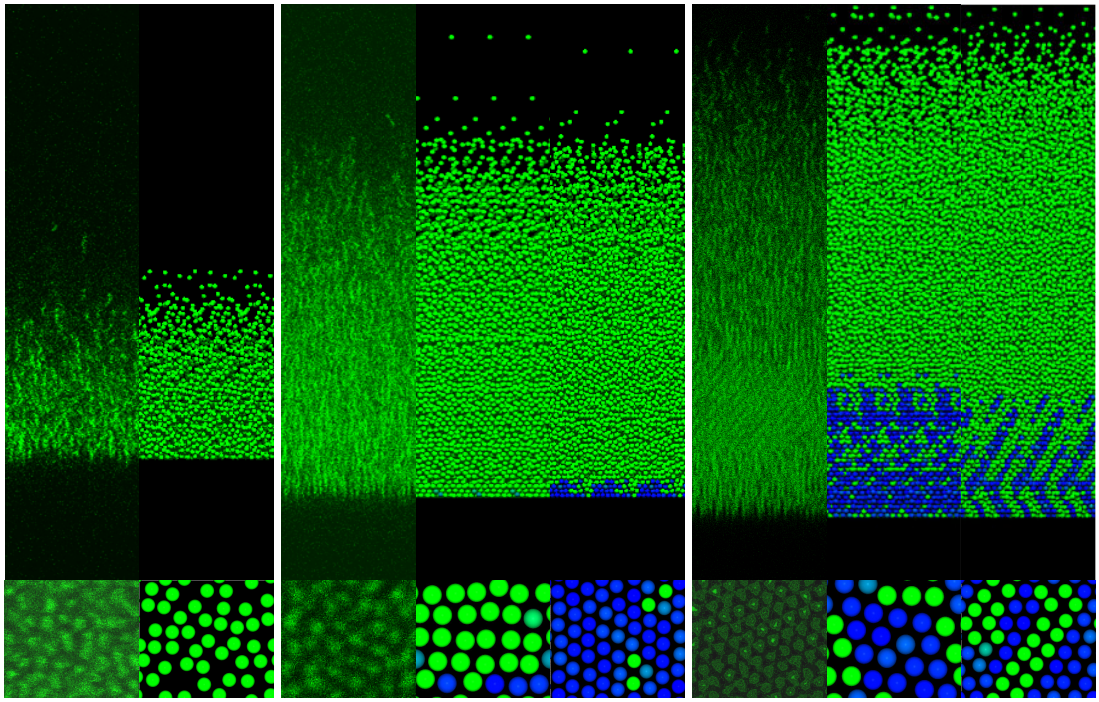

FIG. 5.1. Sedimentation CLSM and simulation results. CLSM bottom (XY) and side (XZ) view images of interfacial sedimentation equilibrium of 720nm fluorescent core-shell silica colloids over 90μm x 20μm (height x width) and rendered configurations from MC simulations for: (a) a dilute single phase fluid, (b) a concentrated fluid near "precrystallization" conditions, and (c) coexisting fluid and solid. Rendered colloids are color coded based on a local, 2-D bond orientational order parameter [Eq. (5.32)] using a continuous blue-green scale (green for ψ_6=0, blue for ψ_6=1). Two simulation renderings are shown in (b) and (c) for small and large system sizes.

microstructures vary significantly on the particle scale in between the trivial limits of homogeneous crystalline multilayers consolidated at low elevations when gravity dominates (l_g/σ<<1) and homogeneous fluid dispersions at all elevations when entropy dominates (l_g/σ>>1). Fig. 5.1 shows sedimentation equilibrium microstructures for three different interfacial concentrations that produce a dilute inhomogeneous fluid, a concentrated inhomogeneous fluid on the verge of interfacial crystallizing, and a concentrated case resulting in coexistence of an inhomogeneous fluid and inhomogeneous solid. The MC simulated microstructures in Fig. 5.1 were generated

using potentials (parameters in Table 5.1) obtained from fitting the LDAP theory [Eqs. (5.4) - (5.24)] to the CSLM measured profiles.

As described in *Theory* and *Methods* sections, the analysis of the CSLM images in Fig. 5.1 is based on the relative colloid fluorescence intensity at different elevations rather than directly locating colloid centers via image analysis algorithms. The rationale for this approach is based on the fast rate of colloid Brownian motion compared to the time required to obtain high resolution images of colloid centers over profile dimensions on the order of 100μm. Such an approach enables fast acquisition of quantitative density profiles and real space visualization of microstructure without the need for rapidly locating prohibitively large numbers of colloid centers before any rearrangements occur within a given configuration. To implement such an approach, spatial variations in fluorescence emission are accounted for by considering the combined effects of emission efficiency, excitation attenuation, and the instrument point spread function as described by Eqs. (5.25) - (5.28). In addition, photobleaching was minimized to avoid undesirable temporal or spatial variations in the emission intensity.

5.4.2 Dilute Interfacial Colloidal Fluid

To demonstrate the use of intensity based CSLM for measuring interfacial sedimentation equilibrium profiles, we first establish quantitative connections between intensity, density, and interactions potentials for the dilute single-phase colloidal fluid in Fig. 5.1(a) with $\phi(z)$ and $I(z)$ curves shown in Fig. 5.2. A single phase fluid is expected for the electrostatic repulsive interactions in this study since attractive interactions are required for liquid-gas coexistence and formation of a gas-liquid interface.[118,119,141] Fig.

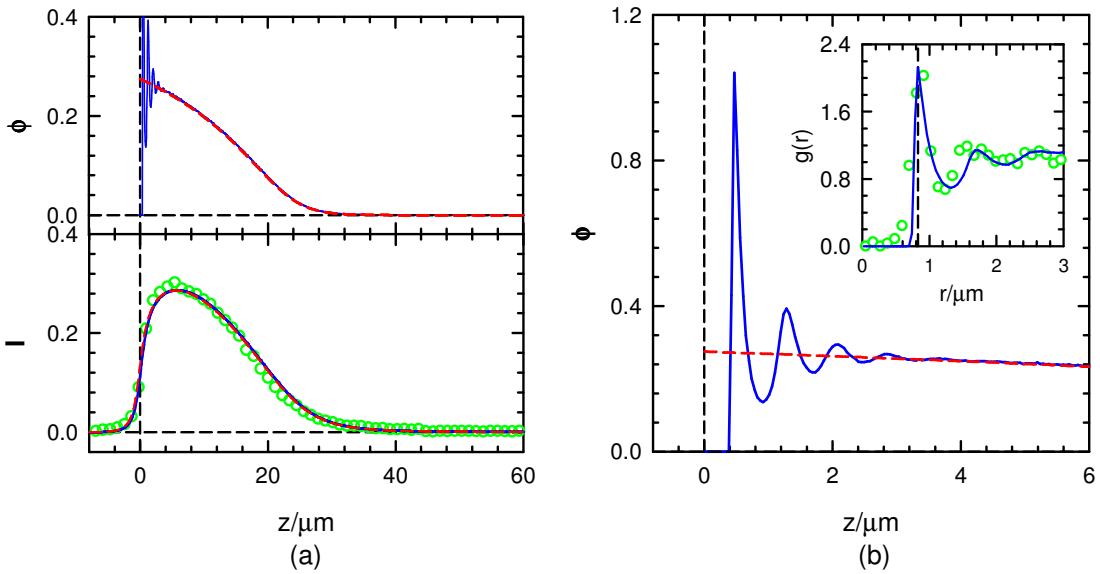

FIG. 5.2. Dilute fluid sedimentation data. Intensity and density profiles for dilute interfacial fluid sedimentation equilibrium with CSLM data (green circles), convoluted effective hard sphere LDA curve (red line), and convoluted, large system size MC simulated data (blue line). Plots include (a) measured and convoluted intensity profiles (bottom), and density profiles (top); also (b) magnified interfacial region of density profile, and (inset) 2-D radial distribution functions for first layer of sediment.

5.2(a) shows the measured $I(z)$ curve obtained from spatial and temporal averaging of multiple CSLM scans and a $\phi(z)$ curve obtained from a fit to the measured $I(z)$ data using the LDAP theory. Fig. 5.2(a) also shows a MC simulated $\phi(z)$ curve using the potentials obtained from the LDAP fit and a $I(z)$ curve generated by convoluting the MC $\phi(z)$ curve using Eqs. (5.25) - (5.28). Fig. 5.2(b) is an expanded plot of the interfacial region of $\phi(z)$ and an inset of the projected 2-D radial distribution function, $g(r)$, for the first fluid layer within 2a of the surface for colloid centers identified in CSLM 2-D images and MC configurations.

Although colloid number density, $\rho(z)$, is the usual way of reporting sedimentation equilibrium profiles and more generally inhomogeneous fluid density

profiles, $\phi(z)$ curves are reported in this work so that the average local volume fraction can be compared directly with the elevation dependent effective hard sphere phase behavior that depends only on effective volume fraction.[129] Local spatial density variations on the scale of the colloid dimension captured in MC simulations can still be analyzed as $\rho(z)$ via a simple conversion using Eq. (5.14).

All parameters used to fit the LDAP theory and in MC simulations are reported in Table 5.1. The only parameters adjusted in the fitting process were ρ_p, κ, and ϕ_0. The relative colloid and solvent density determine the contribution of gravity to the inhomogeneous $\phi(z)$ profile far from the surface. Although ρ_p and the other parameters were obtained by minimizing error in the LDAP fit to the $\phi(z)$ profile at all elevations, the density can also be obtained via fitting Eq. (5.1) in the dilute region where the sedimentation equilibrium profile vanishes and colloidal interactions are unimportant. The colloid density was found to be ρ_p=1.75g/cm^3, which is within the 1.5-2.0g/cm^3 range for organically modified Stober silica.[23] Given the reasonable value for ρ_p (and the remainder of the fit parameters), we find no obvious evidence of expanded $\phi(z)$ profiles due to temperature gradients[125,126] or charge gradient mediated electric fields,[128,133] which is similar to findings of another recent CSLM investigation employing non-aqueous media.[130]

The most probable interparticle spacing of 830nm from the $g(r)$ in Fig. 5.2 indicates 110nm surface spacing between the 720 core colloids that is indicative of electrostatic repulsion, particularly since no macromolecular stabilizers are present. Although the origin of surface and medium charge in the nonaqueous media charge is

not precisely known, some dissociation may occur in the DMF which has a relatively high permittivity (ε=36.7) and/or residual water, ethanol, or ionic impurities remaining from the colloid synthesis could help support charge dissociation.[142]

When using the LDAP theory, the value of κ and ψ_p together determine the effective colloid size in Eq. (5.17) and volume fraction in Eq. (5.18) via the electrostatic repulsion given by Eq. (5.6). Because the integrated electrostatic repulsive potential in Eq. (5.17) determines the effective hard sphere colloid size, an infinite number of κ and ψ_p within limiting bounding values could produce the same effective size and sedimentation equilibrium profile. This coupled interplay in the effective size determined via Eq. (5.17) is also an issue for other methods of determining the effective hard sphere size by equating soft and hard sphere second virial coefficients or more rigorous approaches.[143] To obtain a unique estimate of κ, we specified ψ_p=40mV by equating it with the zeta potential, ζ, obtained in independent electrokinetic measurements (ε determined via Claussius-Mosotti mixing rule in Eq. (5.29), viscosity of 0.700cp from literature[137]), which was found to be in good agreement with other measurements of silica colloid ζ in non-aqueous media.[144] Using ψ_p=40mV, the Debye length in the non-aqueous media was determined to be κ^{-1}=18nm. Although ψ_p and ζ are not in general equivalent, equating the two results produces a value of κ and an estimate of the solution ionic strength [1:1 electrolyte concentration of 17μM using Eq. (5.10)] comparable to other studies of electrostatic interactions in non-aqueous media (without added electrolyte and using non-dried solvents).[145]

The core colloid volume fraction immediately adjacent to the glass microscope slide was ϕ_0=0.28 from the LDAP fit, and the core colloid area fraction was $\phi_{A,0}$=0.53 from the 2-D CSLM image of the first layer. The effective colloid diameter was $2a_{eff}$=790nm [Eq. (5.17)], the effective colloid volume faction at the surface was $\phi_{0,eff}$=0.37 [Eq. (5.18)], and the effective core colloid area fraction was $\phi_{A,0,eff}=\phi_{A,0}(a_{eff}/a)^2$=0.64. These core and effective sizes, volume fractions, and area fractions are consistent with the concentrated 2-D and 3-D fluid microstructure observed parallel to the surface in Fig. 5.1(a) and observations of Brownian motion during dynamic CSLM imaging.

The $\phi(z)$ and $g(r)$ data in Fig. 5.2 display agreement between the intensity based CSLM measurements, the LDAP theory, and MC simulations. Quantitative agreement is observed between CSLM and LDAP generated $\phi(z)$ and $I(z)$ curves. The comparison between the CSLM measurements and LDAP theory is straightforward since profiles from both approaches do not resolve colloid scale spatial variations in density profiles. In contrast, MC simulated $\phi(z)$ were obtained at sufficiently high resolution to capture structure on colloidal dimensions. In principle, deconvoluting $I(z)$ curves with $I_{sp}(z)$ could yield $\phi(z)$ profiles with colloid scale variations, but in practice this is numerically difficult exercise, particularly in the presence of noise. As a result, MC simulated $\phi(z)$ curves in Fig. 5.2(a) were either convoluted using Eqs. (5.25) - (5.28) to generate $I(z)$ curves in agreement with CSLM $I(z)$ curves or re-binned at lower resolution to also display agreement with LDAP $\phi(z)$ curves. Because the 2-D $g(r)$ in Fig. 5.2(b) was constructed directly from colloid centers, it displays agreement with the MC simulated

$g(r)$ on the colloid scale within limitation on spatial resolution and finding 2-D centers in the presence fast self-diffusion rates.

The agreement between CSLM, LDAP, and MC results in Fig. 5.2 demonstrates the general validity and consistency for using these experimental, analytical, and simulation tools together to investigate inhomogeneous, single-phase fluid, colloidal sedimentation equilibrium profiles near surfaces. In contrast to other CSLM sedimentation equilibrium studies that can take ~30s to image a 3-D volume in the presence of many equilibrium rearrangements,[130] this approach acquires single XZ images over distances of ~50σ and ~2sec before any appreciable relaxation occurs in a given configuration.

5.4.3 Concentrated Interfacial Colloidal Fluid

After establishing the intensity based CSLM measurement method for the dilute interfacial colloidal fluid in Fig. 5.2, we now investigate microstructure in more dense fluids, particularly for conditions where crystallization is about to occur in the layers immediately adjacent to the wall surface. Using the same fitting procedure and similar plot formats as in Fig. 5.2, results are shown in Fig. 5.3 for an interfacial sedimentation equilibrium profiles with a colloid volume fraction at the bottom wall surface of ϕ_0=0.43 ($\phi_{0,\mathrm{eff}}$=0.57) and an interfacial core colloid area fraction of $\phi_{A,0}$=0.56 ($\phi_{A,0,\mathrm{eff}}$=0.68). The values of ρ_p and κ were fixed at the same values used for the fit to the dilute fluid in Fig. 5.2 since both samples were prepared in an identical fashion from the same batch at the same time.

Agreement was obtained between the CSLM and LDAP generated $I(z)$ curves

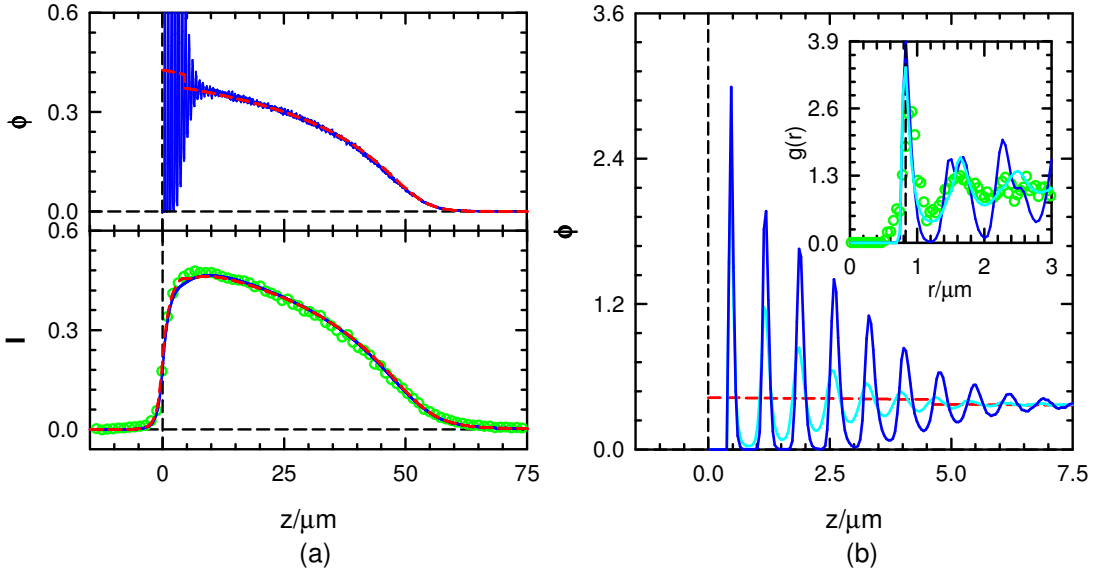

FIG. 5.3. Concentrated fluid sedimentation data. Intensity and density profiles for concentrated interfacial fluid sedimentation equilibrium with CSLM data (green circles), convoluted effective hard sphere LDA curve (red line), and convoluted, large system size MC simulated data for a larger system (blue line) and a smaller system (cyan line). Plots include (a) measured and convoluted intensity profiles (bottom), and density profiles (top); also (b) magnified interfacial region of density profile, and (inset) 2-D radial distribution functions for first layer of sediment.

with a level of correspondence similar to that observed in Fig. 5.2. Convoluting the MC $\phi(z)$ data also produce excellent agreement between $I(z)$ curves from each of the CSLM, LDAP, and MC results. However, the LDAP $\phi(z)$ curve indicates that the first ~6 interfacial layers should be crystalline, whereas the CSLM 2-D image of the first layer and the $g(r)$ of the sediment parallel to the wall clearly indicate a laterally fluid structure (2nd peak has no shoulder or split[146]). In addition, observation of tracer colloid dynamics indicates 3-D long-time self-diffusion characteristic of a fluid rather than 2-D localization within layers or 0D localization on crystal lattice positions. These dynamic CSLM observations also remove any concerns about dynamic arrest in the first layer that could have otherwise been an explanation for an amorphous microstructure at $\phi_{0,\text{eff}}$=0.57

($>\phi_m$) and $\phi_{A,0,eff}$=0.68 ($\approx\phi_{A,f}$[147]).

The MC $\phi(z)$ curves on the colloid scale also reveal different microstructures for different simulation box sizes as shown in Figs. 5.1 and 5.3 (no system size dependence was observed in the dilute fluid case in Fig. 5.2) even though they both produce nearly the same LDA $\phi(z)$ curves when re-binned at lower resolution. In particular, results for the smaller simulation box size (13.9 x 13.9 radii) do not indicate any localization within layers near the surface or any six fold order, whereas, results for the larger box size (19.1 x 16.6 radii) indicate complete localization of colloids within the first 4 layers (0 density between peaks) and significant 2-D six fold order within the first 3 layers. To summarize, the CSLM 2-D image in Fig. 5.1(b) and the small MC system size show fluid characteristics adjacent to the wall surface, whereas the LDAP theoretical fit and the larger MC system size show the onset of interfacial crystallization.

There are a number of issues in the MC simulation method that make it difficult to conclude whether the small or large system size results are more "correct". For example, small simulation box sizes with periodic boundary conditions are known to bias the formation of ordered structures, which is particularly the case for the NVT ensmeble.[147,148] This appears to be the opposite behavior from what is observed in Fig. 5.3 where more order is observed in the larger system size. Another issue to consider is that the larger rectangular simulation box has a greater degree of commensurability with the observed hexagonal lattice at the surface compared to the smaller simulation box. In addition, the non-monotonic, inhomogeneous nature of the interfacial density profile in combination with ensemble and simulation box size/shape effects[147,148] could critically

influence whether interfacial crystallization occurs, particularly because precrystallization is known to occur via a 3-D mechanism rather than stepwise 2-D layer formation.[121,140] A more thorough examination of these MC simulation issues is beyond the scope of the present work, but is an interesting topic worthy of further investigation.

Other issues could also influence whether interfacial crystallization is observed in the CSLM measurements and LDAP theory. The finite polydispersity in the CSLM experiments that is not present in the LDAP theory or MC simulations could critically suppress nucleation and growth in a sedimentation equilibrium profile near interfacial crystallization conditions.[149,150] Because the success of the LDAP theory depends entirely on the determination of the effective colloid size and volume fraction via Eqs. (5.17) and (5.18), the mixed agreement could arise from sensitivity to the parameters in the electrostatic potential in Eq. (5.6) or might require evaluation of the effective size using a more rigorous approach.[143]

Beyond the subtle differences in the first couple of layers in the sedimentation equilibrium profiles in Fig. 5.3, the majority of the dense fluid profile is accurately captured by the measurements, theory, and simulations. The results in Fig. 5.3 also suggest that the intensity based CSLM method in combination with real-space particle tracking approaches might be a useful tool for investigating mechanisms associated with wall-induced precrytsallization of inhomogeneous interfacial colloidal fluids in the presence of a consolidating forces like gravity.[121,140,151] Many of the issues identified in relation to interfacial crystallization are also important for the fluid-solid interface, which is discussed for coexisting fluid and solid phases in the next section.

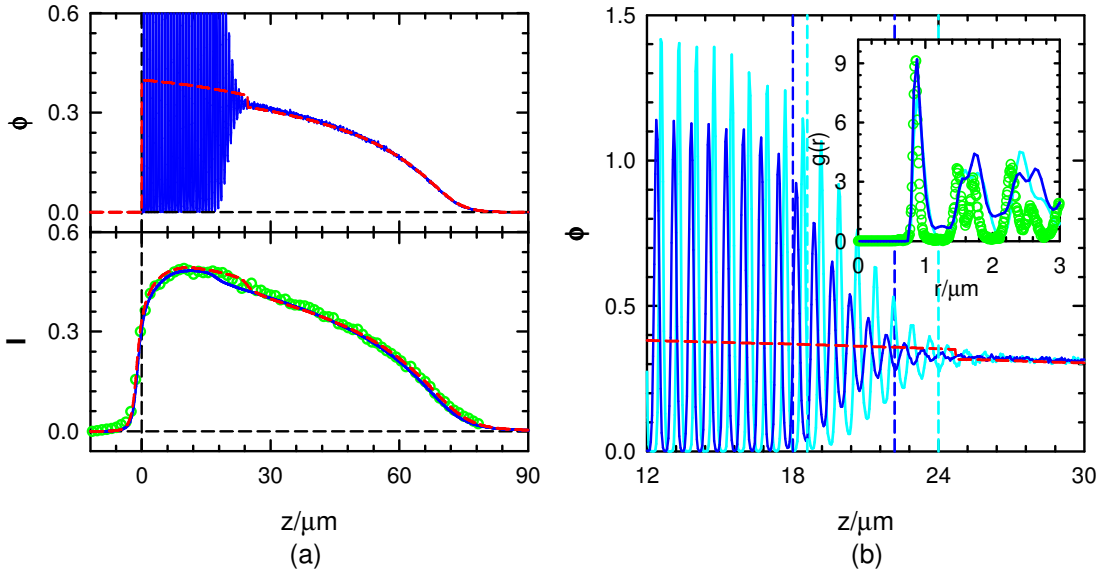

FIG. 5.4. Fluid/solid sedimentation data. Intensity and density profiles for concentrated interfacial fluid/solid sedimentation equilibrium with CSLM data (green circles), convoluted effective hard sphere LDA curve (red line), and convoluted, large system size MC simulated data for a larger system (blue line) and a smaller system (cyan line). Plots include (a) measured and convoluted intensity profiles (bottom), and density profiles (top); also (b) magnified interfacial region of density profile where vertical dashed lines indicate 90-10 width of fluid-solid interface for two MC systems sizes, and (inset) 2-D radial distribution functions for first layer of sediment.

5.4.4 Interfacial Colloid Fluid-Solid Coexistence

After investigating two interfacial fluids cases, we now investigate the use of intensity based CSLM to measure interfacial sedimentation profiles that include fluid-solid coexistence. For the results in Fig. 5.1(c) and Fig. 5.4, a greater number of colloids per area is used so that an increased concentration and osmotic pressure near the wall surface produce interfacial colloidal crystals in equilibrium with colloidal fluids. In fact, the sedimentation equilibrium profiles consists of an inhomogeneous solid phase having elevation dependent density with a transition over a narrow range of elevations to an inhomogeneous fluid density profile at higher elevations similar to those observed in Figs. 5.2 and 5.3. Results in Fig. 5.4 have the same format as Figs. 5.2 and 5.3 with fit

values reported in Table 5.1. Results for two MC system sizes are reported in Fig. 5.4 as in Fig. 5.3.

We begin with several qualitative observations concerning the real space image in Fig. 5.1(c) as they pertain to proceeding with a more quantitative analysis of the coexisting solid an fluid phases in Fig. 5.4. In particular, the real-space CSLM image in Fig. 5.1(c) clearly shows hexagonal interference patterns indicative of a crystalline microstructure beginning at the bottom glass interface and rising up to an elevation of ~25μm (single particles can be made out in higher resolution images since tracking is not a problem in the crystal). The morphology of crystals formed by sedimentation consists of hexagonal 111 crystal planes parallel with the container bottom and mostly stacked on top of each in a random hexagonal close packed configurations,[152,153] although we do not characterize stacking faults in this study.

The top portion of the image in Fig. 5.1(c) clearly resembles the inhomogeneous fluids in Figs. 5.2 and 5.3. Although the 2-D $g(r)$ in Fig. 5.4 is also indicative of the crystallinity at the bottom of the density profile, the somewhat low resolution on the particle centers and polycrystallinity together do not indicate the degree of order as clearly as the simple real-space image of the bottom layer as in Fig. 5.1(c). Dynamic imaging also clearly shows individual colloids localized on lattice sites in the lower depths of the sediment whereas 3-D long-time self-diffusion is apparent in all portions of the inhomogeneous fluid phase similar to Figs. 5.2 and 5.3. As in the concentrated fluid case in Fig. 5.3, there is no evidence of dynamic arrest that would limit the applicability of an equilibrium analysis.

Based on this qualitative real-space information, we can fit the LDAP theory to the CSLM intensity based curves with confidence that fluid-solid phases are indeed present without exclusive reliance on the optical relationship between $\phi(z)$ and $I(z)$ in Eqs. (5.25) - (5.28). The approach to fitting the LDAP theoretical $\phi(z)$ curve to the CSLM measured $I(z)$ curve in Fig. 5.4 followed the same procedure for the fluid only cases in Fig. 5.2 and 5.3 except that Eqs. (5.16) and (5.24) were used to specify the solid phase osmotic pressure until $\phi_{eff}(z)>\phi_m=0.545$ at which point the effective volume fraction was constrained to $\phi_{eff}(z)\leq\phi_f=0.494$ and the fluid osmotic pressure in Eq. (5.15) was used in Eq. (5.24). In the fitting process in Fig. 5.4, the colloid density was again fixed to $\rho_p=1.75 g/cm^3$ since the sample was prepared from the same batch of particles used in Fig. 5.2 and 5.3. However, the sample was index matched and the actual sedimentation equilibrium experiment was performed at later time so that the Debye length was allowed as an adjustable parameter with a fit value of $\kappa^{-1}=28.9$. The core colloid volume fraction at the bottom wall surface was fit as $\phi_0=0.40$, and image analysis of the first layer indicated an interfacial core colloid area fraction of $\phi_{A,0}=0.62$. These interfacial concentrations correspond to effective volume ($\phi_{0,eff}=0.63$) and area ($\phi_{A,0,eff}=0.84$) fractions well above freezing and melting concentrations and are therefore consistent with the observe 3-D and 2-D solid phases.

Within the resolution of the CSLM and LDAP results, the $\phi(z)$ and $I(z)$ curves are in excellent agreement, and the LDA resolved MC curves are essentially indistinguishable from each other and the CSLM and LDAP results. In particular, the

agreement is excellent between all LDA curves within the inhomogeneous solid down to the wall surface and in the inhomogeneous fluid beyond the fluid-solid interface region up to elevations where $\phi(z)$ and $I(z)$ vanish. The intensity based CSLM method captures the density profiles in both fluid and solid phases with a level agreement comparable to the fluid cases in Figs. 5.2 and 5.3.

Locating the fluid-solid interface in each inhomogeneous sedimentation equilibrium density profile is a less trivial matter. The LDAP curve indicates a discrete transition at an elevation of 24.7μm, which in no way indicates that a truly discrete interface exists, but is specified as a precise value based on the limited resolution of LDAP and the nature of the fitting procedure that enforces a discrete transition. Such an approach to fitting a discrete interface has been used to analyze fluid-solid coexistence in macroscopic sedimentation equilibrium profiles, where it is probably more appropriate since the interface between phases is not resolved experimentally on the scale of the colloids.[129] In the case of the $\phi(z)$ curves on the particle scale in Fig. 5.4, the interface is not expected to be discrete as suggested by LDAP curve, but it does provide one estimate of the interface for comparison with the CSLM and MC curves.

To locate the fluid-solid interface elevation in the MC particle scale $\phi(z)$ curves, it is necessary to first estimate the width of the interface using a variant of the so-called 90-10 width.[154] The 90-10 width for the purpose of analyzing coexisting, inhomogeneous fluid and solid phases is based on extrapolation of lines from the solid and fluid phases on either side of the interface region. The width is defined as the distance from which the density falls from 90% of the difference between these two lines

on the high density side to 10% of the difference between these two lines on the low density side of the interface region. Using this criterion, the interface widths are 5.4μm ($12.9a_{eff}$=$6.4\sigma_{eff}$, ~7 layers) for the small system size and 4.2μm ($10.0a_{eff}$=$5.0\sigma_{eff}$, ~6 layers) for the large system size. Interface widths from both MC system sizes are similar to molecular dynamics simulations of the 111 hard sphere fluid-solid interface of 5.9σ[154] and estimates for electrostatic colloidal crystal interfaces of ~5-10 layers.[155]

The elevation of the fluid-solid interfaces in the two MC simulation system sizes is estimated to occur at half of the 90-10 interface width, which gives ~22μm for the small system size and ~20μm for the large system size. In addition to these estimates, isolated particles with 2-D ψ_6>0.8 were identified at elevations up to ~22μm in the small system and up to ~20μm in the large system, which also indicated the termination of crystalline layer characteristics at elevations nearly identical to the interface half-width height. Other established methods for determining the presence of solid and liquid phases based on non-local, ensemble average static (i.e. Hansen-Verlet[156]) or dynamic (i.e. Lindemann[157]) criteria in homogeneous 2-D and 3-D systems[158] are not directly applicable to the inhomogeneous one-dimensional (1-D) interface in Fig. 5.4, although recently reported test-particle dynamic criteria may be useful in future investigations.[159] In any case, both MC $\phi(z)$ curves have fluid-solid interface elevations slightly below the LDAP value with a slight system size dependence.

As in the nearly crystallizing fluid case in Fig. 5.3, a number of issues do not permit a definitive conclusion to be made as to whether the LDAP theory or the MC simulation results provide the better estimate of the fluid-solid interface elevation. The

finite experimental polydispersity and limitations of Eq. (5.17) for determining effective colloid size[135] could influence both the LDAP and MC estimates of the fluid-solid interface elevation in different ways. As described in the analysis of interfacial crystallization in Fig. 5.3, the choice of MC ensemble, system size, and simulation box shape can influence the thermodynamic conditions for fluid-solid coexistence (i.e. hard sphere ϕ) as shown in homogeneous systems.[147,148] These effects may be compounded by NVT boundary conditions do not easily allow an inhomogeneous solid density to decrease isotropically with increasing elevation. For example, in NVT MC simulations, inhomogeneous solids with increasing lattice spacing vs. increasing elevation will be commensurate within a uniform cross section simulation box to varying degrees to promote/suppress crystallization as a non-monotonic function of height.[138] Such an effect could be critically influential to something as sensitive as the precise fluid-solid interface elevation in sedimentation equilibrium profiles with coexisting phases.

The 3-D nature of inhomogeneous solid phases within sedimentation equilibrium profiles appears to be an interesting topic that requires more systematic investigation to asses the best simulation approaches for capturing the inhomogeneous and possibly anisotropic fluid-solid interface. Such MC simulations might require the implementation of a suitable Grand Canonical (NPT) ensemble, very large system sizes, and periodic simulation boxes with varying shapes.[148] In any case, the CSLM, LDAP, and MC results are in excellent agreement with one another at the LDA resolution, and promise to be a useful combination of tools for studying the static and dynamic fluid-solid interface in future sedimentation equilibrium studies.

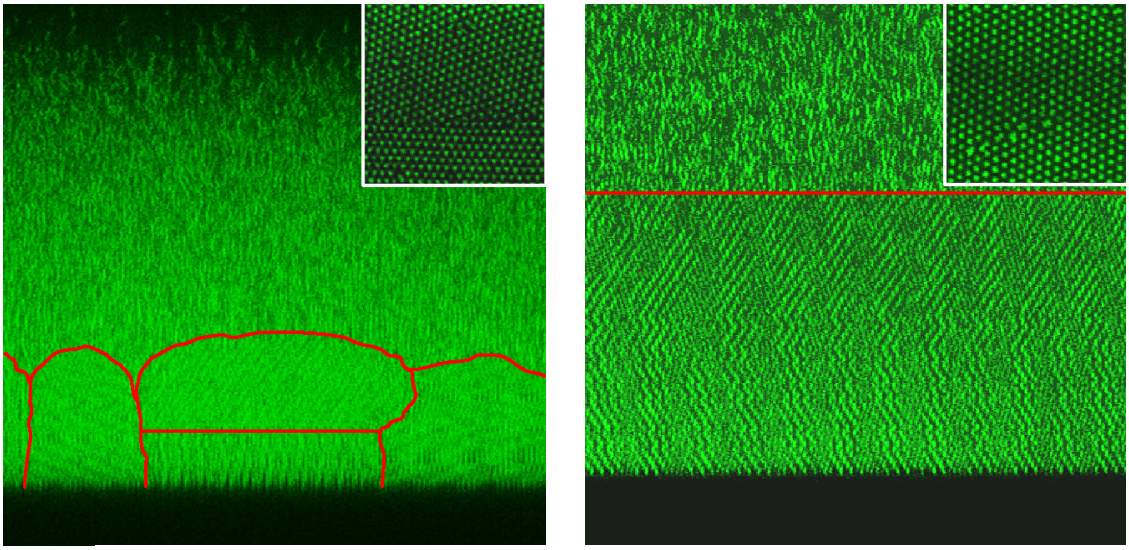

FIG. 5.5. Morphology of colloidal crystals. CSLM side (XZ) view images of coexisting fluid-solid phases showing different crystal and interface morphologies for (left-to-right): (a) polycrystalline solid phase with uneven interface on each domain (red lines), and (b) large single domain solid phase with uniform fluid-solid interface.

5.4.5 Inhomogeneous Fluid-Solid Interface Morphology

The results in Fig. 5.4 focus on understanding the fluid-solid interface in colloidal sedimentation equilibrium profiles based solely on 1-D $\phi(z)$ and $I(z)$ curves. However, it is possible to gain some additional insights into the measured sedimentation equilibrium profiles based on the real-space morphology observable in 2-D cross sectional images in Fig. 5.5 without locating colloid centers. The image in Fig. 5.5(a) shows a polycrystalline structure prepared in a small sedimentation cell (1mm diam. x 0.45mm high; corresponds to $I(z)$ curve in Fig. 5.4), whereas the image in Fig. 5.5(b) shows a larger single domain crystal region prepared in a relatively macroscopic sedimentation cell (1cm diam. x 1cm high). The difference in the two microstructures is believed to arise from differences in convective transients during sedimentation and

crystal growth kinetics that favored larger domains in the larger sedimentation cell.[160,161]

The primary difference between the two microstructures in Fig. 5.5 is that the polycrystalline structure in Fig. 5.5(a) has a 3-D fluid-solid interface with local morphological variations on top of each domain, whereas the large single domain in Fig. 5.5(b) has a distinct interface parallel to the underlying wall surface. While the case in 5b may be reasonably treated by a 1-D density profile, the 3-D morphology of the interface in Fig. 5.5(a) has regions of fluid and solid over a ~10μm elevation range (from 20-30μm) between bounding elevations where only solid and fluid phases are observed. Based on the real-space information in Fig. 5.5, it is apparent that the fluid-solid interface cannot always be treated as crystal planes parallel to the substrate, and in some cases, a 2-D or 3-D model may be required to capture local interface morphology due to polycrystalline domains. For the case of the large single crystal domain in Fig. 5.5(b), a 1-D model with a distinct interface may be appropriate, but realistic experiments will generally involve measurements of polycrystalline domains.

The reason for the various crystal morphologies at the fluid-solid interfaces in Fig. 5.5(a) may arise due to effects not unlike the boundary condition effects discussed in relation to the NVT MC simulations in Fig. 5.4. The finite size of polycrystalline domains in Fig. 5.5(a) have some resemblance to a small NVT simulation box in that an inhomogeneous solid with decreasing density vs. increasing elevation may be unable to expand isotropically within a small polycrystalline domain, which could produce elevation dependent stresses. The rendered MC results in Fig. 5.1(c) indeed show polycrystalline domains at different elevations, and domain boundaries are not

perpendicular to the substrate perhaps indicating some sort of elevation dependence. Elevation dependent internal stresses balanced against fluid-solid interfacial tension[154] could cause polycrystalline domain interfaces to terminate as hemispherical, pyramidal, or other morphologies not unlike those observed in atomic epitaxy[162] (although the origin of internal stress is different in the two cases). This observation is consistent with at least one previous colloidal epitaxy studies in which pyramidal morphologies were observed, although the interfacial crystallization likely occurred via a highly non-equilibrium pathway in this study.[112]

The results in Figs. 5.3 - 5.5 suggest that assembling large, single-domain, equilibrium colloidal crystals on surfaces may require consideration of the formation of inhomogeneous and possibly anisotropic crystalline lattices in the presence of gravity, at least when the characteristic gravitational length and particle dimensions are comparable ($l_g/\sigma \approx 1$). Extending this reasoning, it is also possible that the global free energy minimum microstructure and morphology of sedimented interfacial colloidal crystals could also have a non-trivial dependence on the relative balance of colloidal, surface, and gravitational potentials. For example, attractive or repulsive colloid-surface interactions can be expected to control wetting of the wall surface,[140,163] whereas attractive or repulsive colloidal pair interactions will produce different internal stresses within inhomogeneous/anisotropic crystals and different interfacial tensions for different crystal faces.[154,164] Ultimately, the two cases in Fig. 5.5 suggest how crystal microstructure, polycrystallinity, and morphology obtained via different kinetic pathways might be influenced by the global free energy minimum sedimentation

equilibrium profile as well as relative rates of nucleation, growth, diffusion,[155] sedimentation,[165,166] and convection.[161] Understanding how each of these issues contributes to interfacial colloidal crystal structure on the *kT* scale is essential to engineering (designing, controlling, optimizing) equilibrium self-assembly of ordered materials of colloidal precursors on planar substrates.

5.5 Summary

The results presented in this study demonstrate ability of intensity based CSLM to quantitatively measure 1-D sedimentation equilibrium profiles in agreement with theoretical predictions and simulation results. The CSLM measured profiles were shown to display excellent agreement with LDAP theory and MC simulations for dilute and concentrated interfacial fluids and for fluid-solid coexistence within the LDA limit. Colloid scale density profiles generated in MC simulations also agreed well with fluid and solid phases but displayed some discrepancies in relation to the onset of interfacial crystallization and the elevation of the fluid-solid interface. Factors leading to these discrepancies may include finite polydispersity unaccounted for in the analysis, limitations on estimates of the effective colloid size, and specifically in MC simulations, effect related to ensemble choice, system size, simulation box shape, and modeling inhomogeneous solids. In fluid-solid coexistence case, real-space images also suggest how elevation dependent internal and interfacial stresses might lead to polycrystalline 3-D interface morphologies rather than 111 planes oriented parallel to the substrate. Ultimately, the present study demonstrates the successful implementation of a new approach to measuring interfacial sedimentation equilibrium profiles that benefits from

not having to locate colloid centers but still retains the advantages of real-space imaging of microstructures on the colloid scale.

6. DEPLETION CRYSTALS

6.1 Introduction

This section presents the research directed towards the 3-D imaging of attractive depletion crystals formed by sedimenting colloidal dispersions. To accomplish this task, this work has focused on functionalizing large (> 1 μm) silica particles that will exhibit depletion interactions with smaller particles or a dissolved polymer when dispersed in a refractive index-matching non-aqueous media. As will be documented in the next subsection, a number of other researchers have explored depletion systems. But their work tends to be concentrated on either the 2-D structure of the crystals formed on a surface, or the formation of gel networks in the bulk. The work addressed in this section has been carried out to allow for profile and 3-D imaging and analysis of depletion attractive sediments in a refractive index-matched media, using the same methods developed in Section 5 for electrostatic repulsive systems. Such imaging and analysis would improve our understanding of how the 3-D depletion crystal microstructure is influenced by osmotic pressure (a function of sediment depth) and the strength of attraction.

The work described in this section is ongoing, largely due to the difficulties that have been encountered in obtaining depletion crystals in a refractive index-matching media. As was addressed in Section 5, the preferred experimental system consists of fluorescent core/shell silica particles dispersed in a DMF/toluene mixture. Recent attempts at grafting silica particles with a sterically stabilizing layer of poly(isobutylene) are promising. The particles are stable when dispersed in toluene, and do not appear to

exhibit electrostatic repulsion that would prevent the expression of depletion attraction. Still, additional effort is required. Specifically, the particles – while stable with respect to other particles – have been observed to stick to the sedimentation cell's wall in preliminary experiments. It is believed that this behavior is due to an incomplete coating of the cell wall with poly(isobutylene), but more experiments are needed before Van der Waals interactions with the cell wall can be ruled out. After the stability issues with the wall have been resolved, it will be necessary to demonstrate that depletion crystals can be formed from the poly(isobutylene) coated silica particles.

Other strategies where explored before the experiments with poly(isobutylene) coated silica particles include the use of: (1) bare silica; (2) silica coated with octadecyl chains; and (3) silica coated with an external layer of quantum dots via a peptide bond. Attempts to use bare silica with this system – as was used for the experiments in Section 5 – were unsuccessful due to the presence of electrostatic repulsion that prevented the particles from getting close enough to experience depletion-induced attraction. The particles coated with octadecyl chains dispersed readily in a DMF/toluene mixture, but proved to be unstable on the sedimentation cell's wall due to the presence of van der Waals forces. The particles coated with an external layer of quantum dots dispersed readily in a DMF/toluene mixture, were stable on the cell's wall, easily formed depletion crystals in the presence of smaller (< 100 nm) silica particles coated with octadecyl chains, but readily melted when exposed to the confocal microscope's laser.

The results with the quantum dot-coated particles have provided an interesting avenue for research. Further investigation revealed that only the regions scanned by the

confocal microscope's laser were melted. Also, the melted regions were observed by optical microscopy to readily recrystallize. In a recent proof of concept experiment, these two observations were exploited to selectively melt targeted crystal grains, which resulted in an increase in the size of the surrounding crystal grains after recrystallization. This experiment demonstrates the potential for zone refining of colloidal crystals.

6.2 Literature Review

A number of different systems have been used to investigation depletion-induced attractive interactions in colloidal dispersions. One of the more popular polymer latex systems is charged stabilized polystyrene spheres dispersed in an aqueous media,[108,167-171] frequently with the addition of 0.01 molar sodium chloride.[172-178] Another common system is PMMA particles dispersed in a non-aqueous media to achieve refractive index or density matching, and sterically stabilized by a coating of grafted polymers,[163,179-181]

Silica particles have also been used in the study of depletion interactions. The systems based on non-aqueous media (including refractive index-matched systems) tend to rely on smaller silica particles (< 300 nm) that have been coated with 1-octadecanol, and use a polymer such as PDMS to induce depletion attraction.[182-194] The use of larger silica particles appears to be limited to aqueous systems.[195-198]

The annealing of colloidal crystals can be accomplished by a number of methods. One approach, which has been applied to depletion crystals, is to adjust the temperature of the entire sample. In one example, the variation of sample temperature affected the micelles used to induce depletion attraction in polystyrene particles in water, thereby allowing the attractive force to be tuned and the sample to be melted and

recrystallized.[108] The other methods rely on the use of shear or optical tweezers, and have been applied to electrostatic stable or hard sphere systems. The shear systems include hard sphere PMMA particles in a non-aqueous media sheared between two plates,[199] and electrostatically stablized polystyrene particles in water sheared by oscillatory flow.[200] The use of optical tweezers to accomplish localized annealing relies on a focused laser creating an optical gradient force that will dislocate individual particles from their lattice sites.[201,202] This approach has been successfully applied to electrostatic crystals of polystyrene particles in water.[201,202]

6.3 Theory

To interpret the results presented in this section, it is helpful to understand van der Waals forces, electrostatic stabilization, steric stabilization, entropic depletion forces, and optical gradient forces. Detailed equations exist to describe these phenomena, but these equations will not be needed for the interpretation of the experimental results.

Van der Waals forces arise through the polarization of one set of molecules inducing polarization in a second set via electromagnetic waves,[94] and are attractive for the systems described in this work. When attractive, these forces can cause colloidal particles to aggregate, or to stick to surfaces.[94] The range and magnitude of van der Waals forces increase with increasing particle size, but decrease as the refractive index of the medium approaches that of the particles.[94] To avoid colloidal particle aggregation, it is necessary to keep particles separated from surfaces and from each other.[94] This separation is frequently accomplished through electrostatic or steric stabilization.[94] In both cases, the goal is to achieve particle-particle and particle-wall

separations that are too great for the van der Waals forces to overcome the thermal energy of the particles.[94] Electrostatic stabilization is accomplished by the presence of charged species on the surface of the particles and the walls.[94] Some colloidal particles, such as silica, will possess a native charge that is sufficient for stabilization under appropriate conditions.[94] The electrostatic repulsion can be screened by adding ions to the media in which the particles are dispersed.[94] The magnitude of the repulsion is also dependent on the dielectric constant of the media.[94] Steric stabilization is accomplished by attaching polymers to the surfaces of particles and the wall.[94] For entropic reasons, the polymer brush layers on different surfaces will avoid entangling, thereby keeping the surfaces separated.[94]

Attractive entropic depletion forces can be longer-ranged forces than van der Waals forces.[94] Depletion forces arise when smaller particles (including colloidal particles, dissolved polymer, and surfactant micelles) are mixed with larger particles.[94] As shown in Fig. 6.1, there will exist a volume around the larger particles and surfaces from which the centers of the smaller particles are excluded due to boundary contact.[94] An overlap in these excluded volumes will increase the total system volume available to the smaller particles.[94] Conversely, any separation of overlapping excluded volumes decreases the amount of the system volume available to the small particles.[94] As a result, once excluded volumes overlap, the large particles will have to overcome the osmotic pressure of the smaller particles if excluded volumes are to separate again – thereby creating an apparent attraction between the larger particles or the large particles

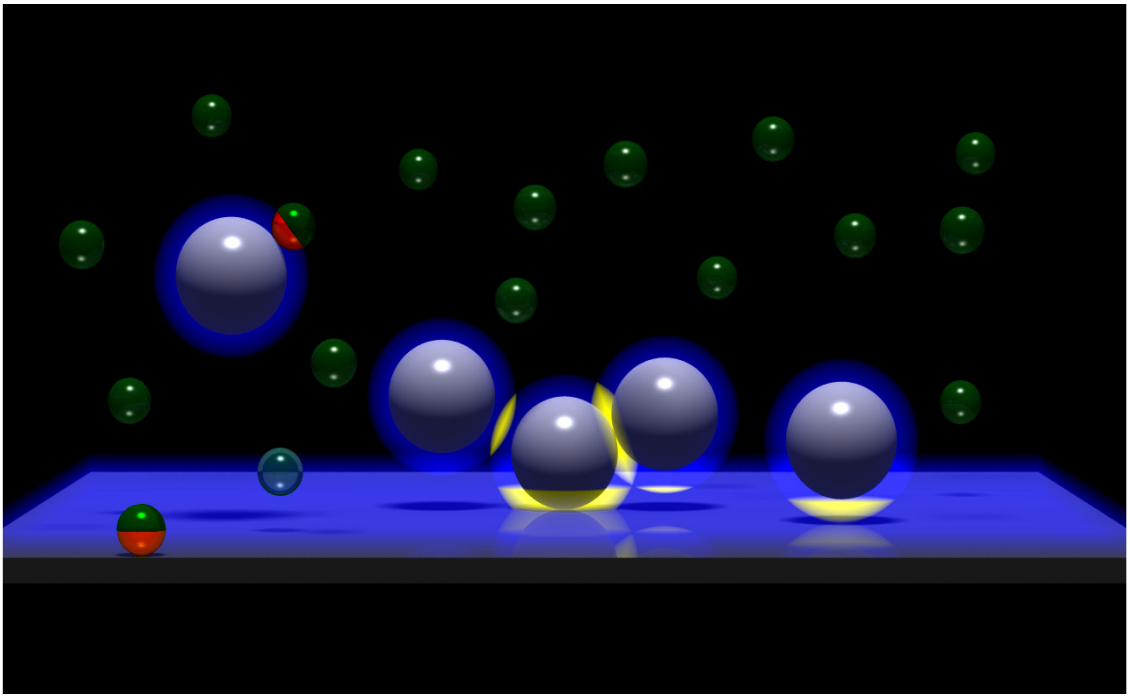

FIG. 6.1. Rendering illustrating some of the concepts behind entropic depletion forces. Around each large particle and surface (grey), there exists an excluded volume (blue glow) in which the centers of the smaller particles (green) are excluded by contact between the surfaces and the outer boundaries of the smaller particles. Overlap of the excluded volumes (yellow glow) increases the amount of the total system volume available to the small particles.

and the surface.[94]

Optical gradient forces arise when an object with a different refractive index than the surrounding media is illuminated by a light gradient.[87] The particle will refract the light, and by refracting photons experience a change in momentum.[87] The effect is that the particle will migrate towards the region of higher light intensity.[87] In the case of an excited gas laser beam, this region would be in the center of the beam.[87]

6.4 Experimental, Results, and Discussion

6.4.1 Bare Silica

To begin the research covered by this section, depletion crystals were grown

from 2.34-μm silica particles (purchased from Bangs Lags) dispersed in water, using sodium dodecylsulfate as the depletion agent. The crystals were first grown in confined cells composed of a glass coverslip sealed by epoxy to a microscope slide; and then in a sedimentation cell as described in Section 5, with the only difference being that the cell sidewalls were formed using a 145-μm thick coverslip, rather than a silicon wafer. Following this success, the system was extended to 2.34-μm silica particles dispersed in a DMF/toluene mixture (using the same ratio as described in Section 5). Both dissolved polystyrene and 70-nm silica particles were attempted as the depletion agent. Due to the use of organic solvents incompatible with epoxy, only the sedimentation cell was used. Depletion crystals were not obtained in the DMF/toluene mixture. In fact, the presence of any depletion attraction was not observed.

It is unlikely that the attempted concentrations of the depletion agent in the DMF/toluene system were not high enough. If fact, the concentration of the 70 nm silica particles was so high in some experiments, that the larger particles ceased diffusing or exhibiting any visible Brownian motion. Rather, it is suspected that the difficulty resides in the electrostatic stabilization of the large silica particles. Because SDS is an ionic surfactant, the electrostatic charge on the surface of the silica particles is screened as the concentration of the SDS is increased. On the other had, both dissolved polystyrene and the 70 nm silica particles are not expected to appreciably increase the ionic strength of the DMF/toluene mixture. As such, it appears that the electrostatic repulsion of the large silica particles was large enough to prevent the excluded volumes from overlapping.

In an attempt to overcome this difficulty, lithium nitrate salt was dissolved into

the DMF/toluene mixture. Several concentrations were attempted, ranging from 2.2 to 0.036 millimolar. Unfortunately, the optimum concentration could not be indentified – either the particles destabilized (sticking to the wall and each other), or they failed to exhibit any noticeable depletion attraction. As a result, it was concluded that there was only a narrow range of salt concentrations that would allow the particles to be stable, but to also exhibit depletion attraction. Because such a range would proved difficult to reproduce experimentally, it was decided that functionalization of the silica surface should be attempted.

6.4.2 Octadecyl Functionalized Silica

2.34-μm silica particles were coated with both 1-octadecanol and OTMS according to the procedures provided in Section 2. Glass coverslips used for the sedimentation cell bottoms were functionalized with OTMS. The functionalized particles were observed to readily disperse in toluene, and to also remain stable in the bulk. However, on sedimentation the particles would stick to the wall and to each other, even in the absence of a depleting agent. The outcome is that the particles were not able to diffuse horizontally on the coverslip, and therefore could not come together to form crystals. It is suspected that the van der Waals forces between the 2.34 mm particles and the wall were too great to be stabilized by an octadecyl carbon chain grafted to the surface. This may explain why other researches using octadecanol-coated particles have limited their particle sizes to less than 300 nm.[182-194] Given that an increase in the polymer size also increases the magnitude of the steric stability,[53] it was decided to attempt to graft poly(isobutylene) with a molecular weight of 1,300 to the surface of the

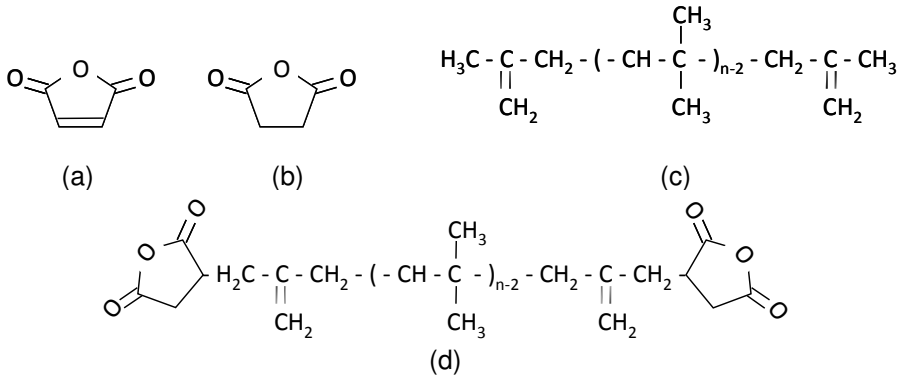

FIG. 6.2. Reagents used for steric stabilization of silica particles. (a) maleic anhydride, (b) succinic anhydride, (c) poly(isobutylene), and (d) poly(isobutenyl) succinic anhydride

silica.

6.4.3 Poly(isobutylene) Functionalized Silica

Initially, it was attempted to functionalize 2.34-μm silica particles with poly(isobutylene) according to the literature method.[53,62,63] Maleic anhydride will react with a carbon-hydrogen bond that is activated by a nearby carbon-carbon bond to form a succinic anhydride group attached to an alkene.[203] Poly(isobutylene), which is formed from the free radical polymerization of isobutylene, possesses the necessary activated carbon-hydrogen bond at the ends of the polymer.[204] As a result, the reaction with maleic anhydride adds the succinic anhydride groups to the ends of the polymer chain,[204] resulting in poly(isobutenyl) succinic anhydride (Fig. 6.2). This compound is filtered and then reacted with tetraethylpentamine to amine-functionalize the succinic anhydride groups.[53,62,63] The reaction carried out in refluxing toluene, reportedly to remove the water that is formed by the reaction with the amine.[53,62,63] The compound, after further purification, is then reacted with the silica.[53,62,63]

The coating of 2.34-μm silica particles was unsuccessful (Fig. 6.3). When

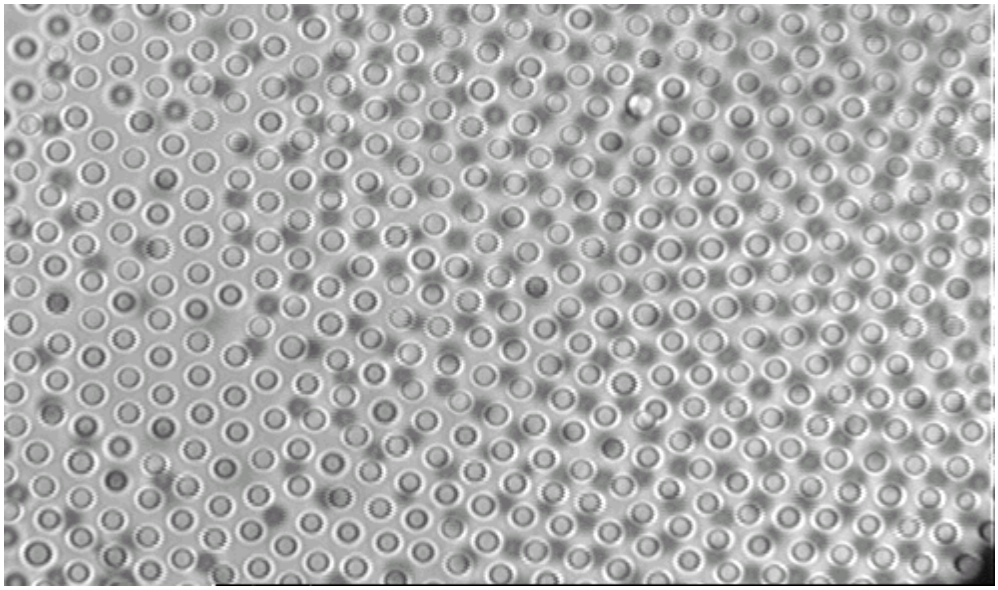

FIG. 6.3. Silica particles in toluene. 2.34 μm silica particles dispersed in toluene after an attempted coating with amine-functionalized poly(isobutenyl) succinic anhydride.

distributed in toluene, the particles exhibited long-range electrostatic repulsion with particle-particle surface separations of about one particle diameter. However, particles coated with poly(isobutylene) should be uncharged.[53] While most of the steps are well defined in the literature, the reaction time between the amine-functionalized poly(isobutenyl) succinic anhydride and the silica particles is not specified. Because the other steps behaved as described in the literature (appropriate color changes and reaction byproducts), it is suspected that the breakdown occurred with the grafting step.

As can be seen in Section 2, silanes are frequently used to attach molecules to the surface of silica. The use of an amine to react with the silica surface is unusual. As such, it was recently decided to attempt another route to attach poly(isobutylene) to the silica particles: the surface of the silica particle was amine-functionalized using APMS, and those particles were then mixed with poly(isobutenyl) succinic anhydride in

tetrahydrofuran at room temperature. Glass coverslips were functionalized in the same manner. Preliminary results are encouraging, but more work is needed. The particles are stable with respect to each other and exhibit no obvious electrostatic repulsion. However, the particles continue to stick to the slide. It may be that the coverslips were not completely silanized. Or, perhaps the functionalized slides need to be heated after the addition of the poly(isobutenyl) succinic anhydride. The literature method states that the heating during the amine reaction is to drive off the water that is produced as a byproduct, but it may also serve to drive the reaction.

6.4.4 Quantum Dot Functionalized Silica

1.1-μm amine-functionalized silica particles were coated with a layer of DHLA-functionalized CdSe-ZnS quantum dots by the method described in Section 2. It was hoped that the quantum dot layer would lower the electrostatic interactions between the particles. These particles were then dispersed in toluene and mixed with various concentrations of 1-octadecanol-coated 70-nm silica particles. Depletion crystals were readily obtained from this system, but attempts to image the crystals with the confocal microscope invariably led to localized melting of the crystals.

While 3-D imaging of this system was not possible, the results pointed to a potential method for zone refining of colloidal depletion crystals. As a proof of concept experiment, a large depletion crystal grain was selected and centered in the middle of the field of view (Fig. 6.4). The targeted crystal grain was then melted by scanning the center portion of the screen with the 488-nm line of the confocal microscope's argon ion laser (Fig. 6.5). The edges of the surrounding crystal grains

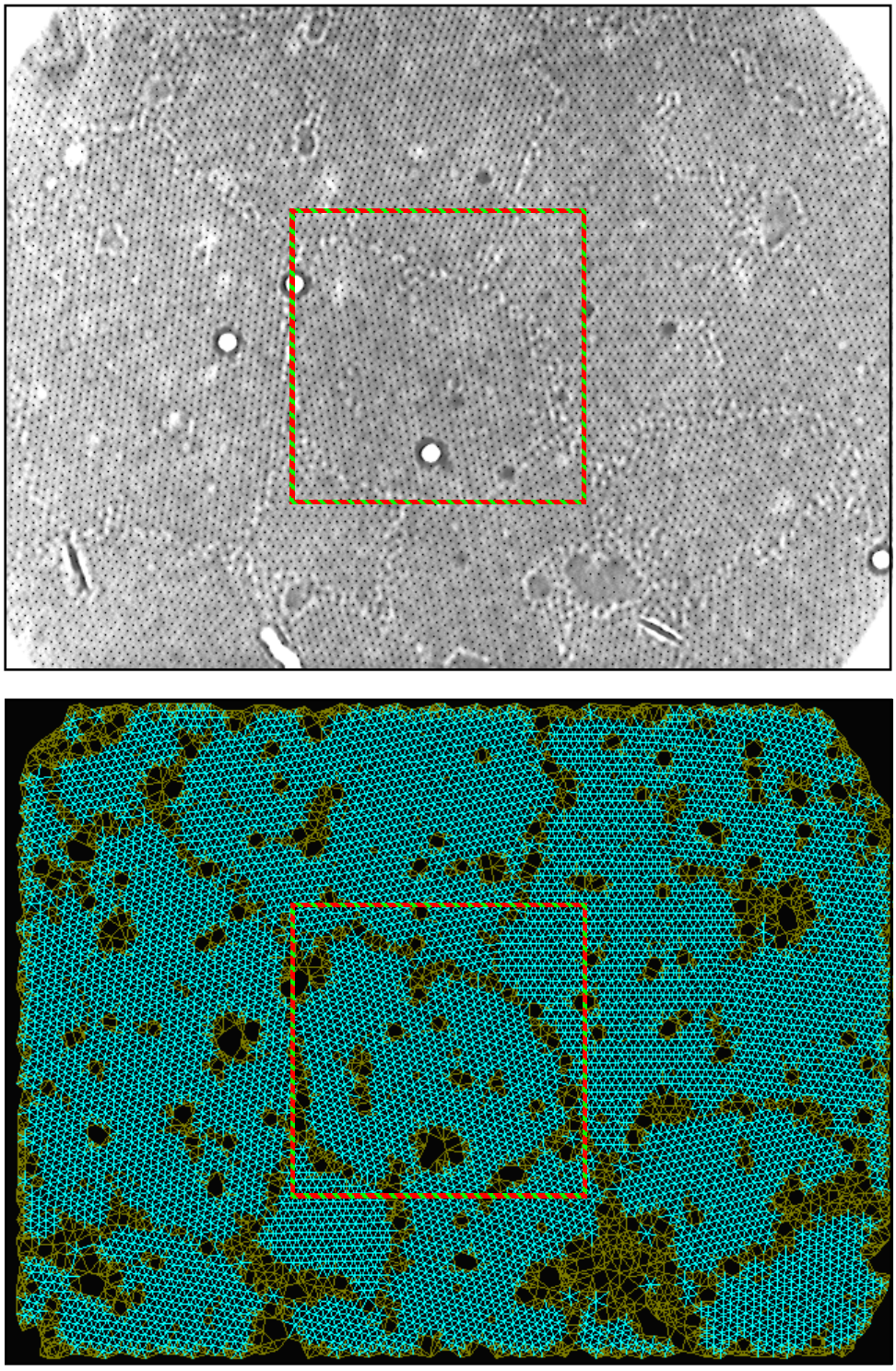

FIG. 6.4. Laser annealing: before irradiation. Crystal before melting as imaged (top) and after processing with triangulation software (bottom). Hatched boxes indicate the region that will be exposed to laser radiation.

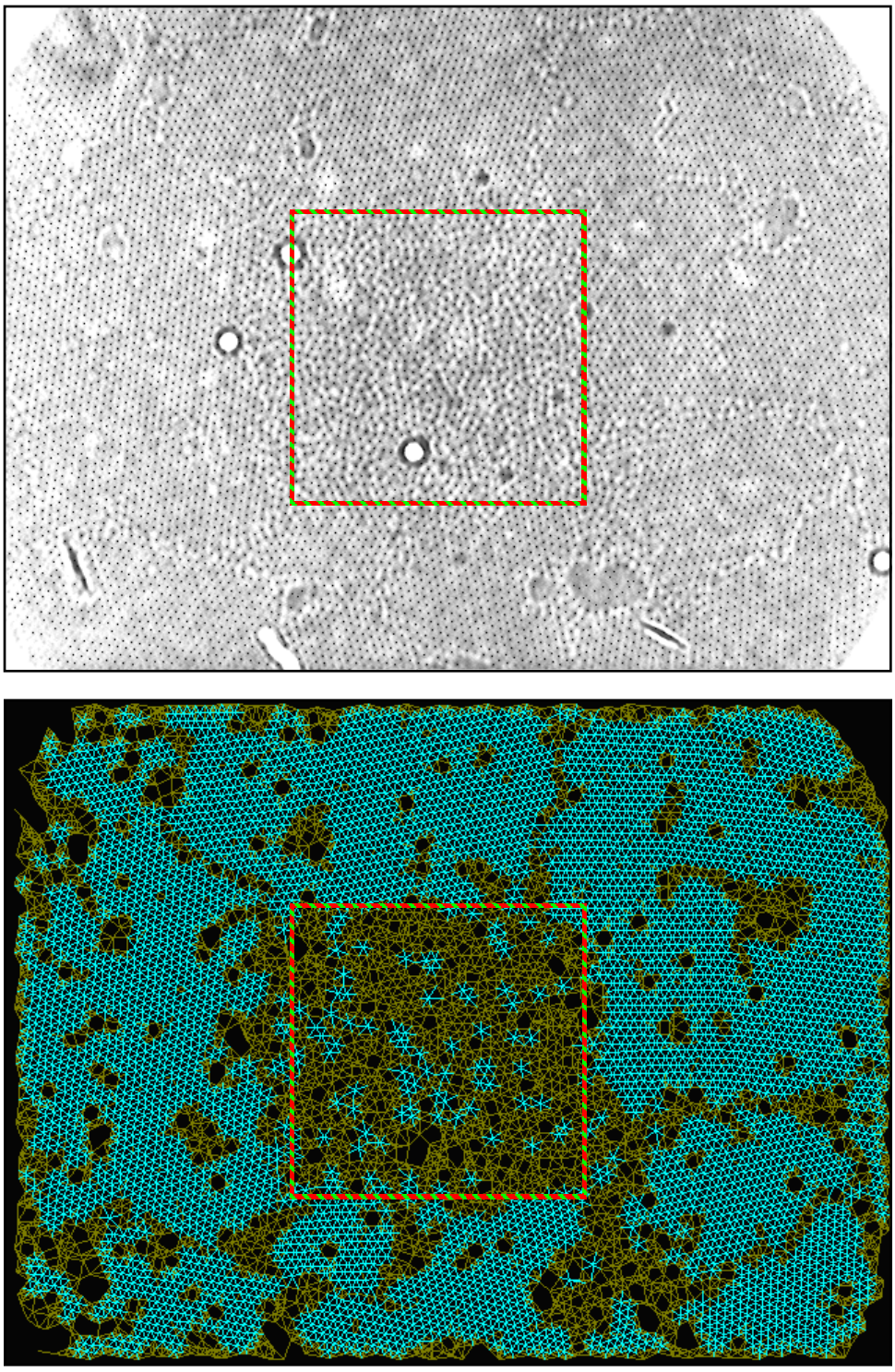

FIG. 6.5. Laser annealing: shortly after irradiation. Crystal after melting as imaged (top) and after processing with triangulation software (bottom). Hatched boxes indicate the region that has been exposed to laser radiation.

were observed to begin growing into the melted region before nucleation occurred. While a new grain did nucleate in the melted region (Fig. 6.6), it was not able to grow as large as the original grain due to the prior growth of the surrounding grains (Fig. 6.7).

Optical gradient forces are not considered to be the cause of the crystal melting. The optical gradient force annealing experiments described in literature relied on a focused 532 nm laser rated at 100 mW to serve as the optical tweezers.[201] Further, the literature notes that lower power lasers only served to strain particles' neighbors, but did not cause them to leave their lattice positions.[201] In this case, however, the crystal was observed to melt when using the 488 nm line on a 200 mW argon ion laser at settings as low as 0.1%. Further, the optical gradient approach relies on using the laser to disrupt the position of particles in an electrostatic crystal, either removing them from their lattice position or staining their neighbors.[201] It seems improbably that this approach would work with tightly-bound depletion crystals. It is also not the case of the laser acting solely on the depleting agent, as the same behavior was observed in electrostatic crystals of quantum dot coated silica particles.

The mechanism appears to be the laser heating the quantum dot layer on the particles, which in heats the surrounding solvent and particles. As the solvent and particles heat, the osmotic pressure of the particles increases, allowing them to overcome the osmotic pressure of the depleting agent (in the case of depletion crystals) and the surrounding particles (in the case of both depletion and electrostatic crystals). Observations supporting this mechanism include:

- The effect is not instantaneous, as might be expected from an optical tweezer

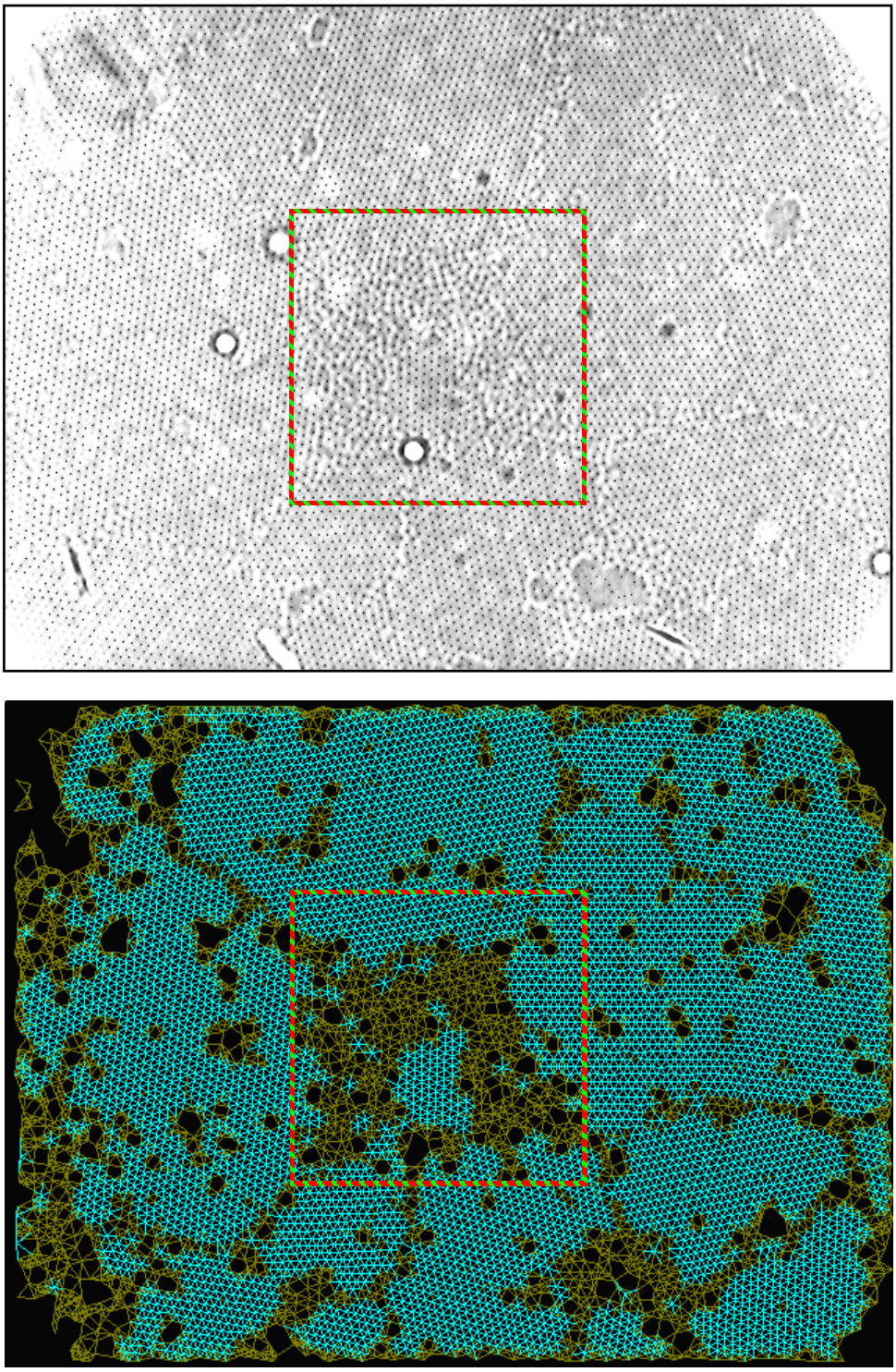

FIG. 6.6. Laser annealing: after irradiation. Crystal after melting and during regrowth as imaged (top) and after processing with triangulation software (bottom). Hatched boxes indicate the region that has been exposed to laser radiation.

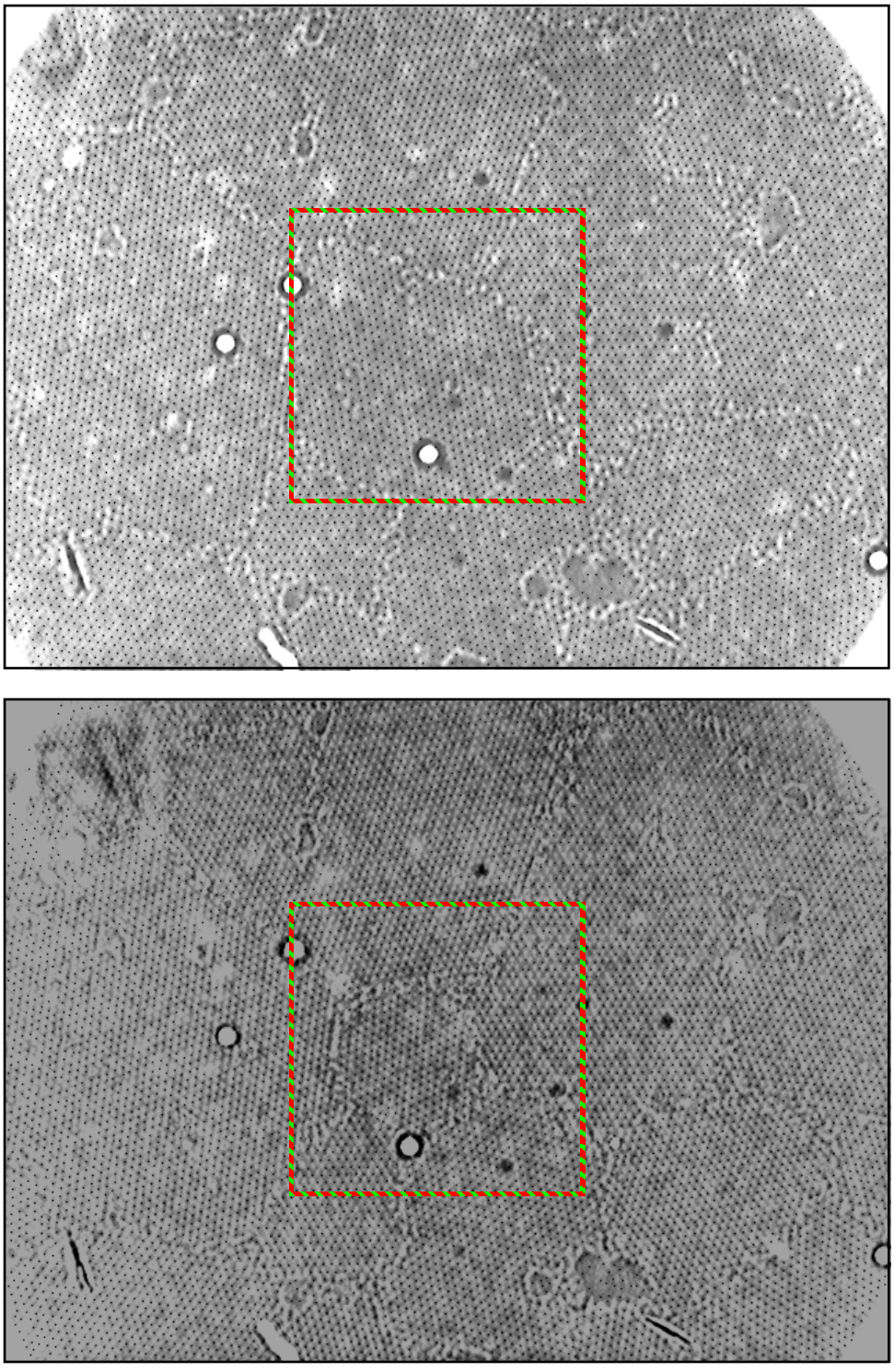

FIG. 6.7. Laser annealing: comparison of before and after. Crystal before melting (top) and after regrowth (bottom) as imaged showing an increase in the size of the surrounding grains. Hatched boxes indicate the region of laser radiation exposure.

mechanism, but occurs gradually: first the crystal lattice in the scan region expands, then the Brownian motion of the affected particles increase until long-range order is lost;

- The rate at which the lattice expands and melts varies with the laser intensity, and decreases as the quantum dots are photobleached;
- In thick cells, convection currents are set up, as indicated by the continual migration of particles to the center of the scan region during scanning;
- In thin cells, no migration of the particles is observed;
- This behavior has not been observed in particles coated with a molecular fluorophore; and
- The laser excitation appears to have no effect on the position or motion of particles in a dilute system.

6.5 Summary and Future Work

This section addressed the portion of this work that explored the formation of depletion crystals in a refractive index-matched medium. It is concluded that the formation of depletion crystals with bare silica particles in a DMF/toluene mixture will be difficult due to electrostatic interactions preventing the overlap of the excluded volumes. Also, coating the silica particles with 1-octadecanol will not resolve all issues because, for the size particles required for imaging of the microstructure, 1-octadecanol does not appear to provide sufficient stability to overcome the effects of van der Waals forces. Steric stabilization with a larger polymer, such as poly(isobutylene) with a molecular weight of 1300 or greater stands out as the most promising route to achieve

depletion crystals of large silica particles in a non-aqueous medium. It is also concluded that excitation of quantum dot-coated silica particles hold potential for the zone refining of colloidal depletion crystals.

Future work includes perfecting the coating of silica with poly(isobutylene). It would appear that, after modifying the procedure in literature, we are able to coat silica particles. But the necessary coating of the glass coverslip remains to be achieved. Once large silica particles have been steric stabilized in non-aqueous media, the next step will be to form depletion crystals. This will allow for the 3-D microstructure of such crystals formed from a dilute gas to be elucidated. Following, it would be worthwhile to apply the intensity-based techniques described in Section 5 to sediments of attractive colloids to understand how the 3-D microstructure varies with increasing attraction.

There is also the potential for future work in crystal annealing. The most immediate priority is to determine if the quantum dots must be on the surface of the particles, or if core/shell silica particles will exhibit the same behavior. The outcome will have implications for both the annealing of colloidal crystals and the imaging of sediments by confocal microscopy using quantum dot labeled particles. Also, it would be interesting to see if the same behavior is observed in silica particles coated with gold nanoparticles, as this route may address the issue of not being able to anneal the crystals after the quantum dots have photobleached. Finally, it should be determined if four-fold ordering that is induced by a small pattern can be retained beyond the limits of the pattern if zone refining is utilized to enlarge a grain that has formed on the pattern.

7. CONCLUSIONS

The work in this dissertation explores the use of confocal microscopy to study colloidal sediments and crystals. As part of this work, many of the tools and techniques had to be either developed from scratch or implemented from incomplete procedures described in literature, including: the synthesis of custom particles; the development of novel data processing algorithms; the implementation of perturbation theory for both two- and 3-D systems; the development of a novel intensity-based method to quantify the equilibrium behavior of colloidal sediments; and methods for stabilizing large silica particles dispersed in non-aqueous solvents. Those efforts are described in detail in this dissertation. Also, this dissertation presents the results that were obtained from investigations into the sediments and crystal microstructure of repulsive colloidal particles. Work into sediments of attractive colloidal sediments is ongoing, and the progress to date is covered.

Each of the previous sections contains a detailed summary of the research finding applicable to their respective aspects of this work. The significant conclusions that have arisen as a result of this study of the application of confocal microscopy to colloidal sediments and crystals are:

- When synthesizing silica particles by the Stöber reaction, it is vital to first vacuum distill the alkyl orthosilicate;
- Large silica shells can be quickly grown on small cores by using a limited number of cores, and adding the shells under slow growth conditions such as reduced temperature;

- Quantum dot-labeled silica particles are best obtained by reacting DHLA-functionalized quantum dots with amine-functionalized silica particles;
- Calculation of the RMS error between a pattern and an image will locate particle centers with great accuracy then intensity-based approaches;
- It is possible to deconvolute a data curve while retaining the latent curve's shape if knowledge of the curve's behavior is used to suppress the effects of random noise, rather than seeking a continuous solution;
- When performing perturbation theory calculations, it is suitable to use integration of the Fundamental Equation, along with the appropriate equation of state, to calculation the Helmholtz free energy of the reference state;
- The implementation of perturbation theory to 2-D colloidal systems may not be practical do to the similarity in slopes of the fluid and solid Gibbs free energy vs. osmotic pressure curves;
- It is possible to correlate the fluorescent intensity to the volume fraction in a sediment of fluorescent colloidal particles in a refractive index-matched system, thereby allowing for the quantification of thermodynamic behavior without the need to locate individual particle centers throughout the sediment;
- Sedimentation conditions, such as the presence or absence of convection currents, can have a significant impact on the microstructure of the resulting crystals;
- Growing depletion crystals from large (> 300 nm) silica particles dispersed in a non-aqueous medium will require the grafting of polymers such as poly(isobutylene) to the surface of the particles and cell bottom; and

- It is possible to zone refine electrostatic and depletion colloidal crystals formed from quantum dot coated silica particles by scanning regions of the crystal with a focused laser at a wavelength that excites the quantum dots.

REFERENCES

[1] J. A. Lewis, J. Am. Ceram. Soc. **83**, 2341-2359 (2000).

[2] B. Balzer, M. K. M. Hruschka, and L. J. Gauckler, J. Colloid Interf. Sci. **216**, 379-386 (1999).

[3] M. Cloitre, R. Borrega, F. Monti, and L. Leibler, Phys. Rev. Lett. **90**, 068303 1-4 (2003).

[4] A. F. Routh and W. B. Russel, Langmuir **15**, 7762-7773 (1999).

[5] B. J. Ash, L. S. Schadler, and R. W. Siegel, Mater. Lett. **55**, 83-87 (2002).

[6] C. F. Zukoski, Chem. Eng. Sci. **50**, 4073-4079 (1995).

[7] A. M. Kulkarni and C. F. Zukoski, Langmuir **18**, 3090-3099 (2002).

[8] S. Yamamuro, D. F. Farrell, and S. A. Majetich, Phys. Rev. B **65**, 224431 1-9 (2002).

[9] J. H. Holtz and S. A. Asher, Nature (London) **389**, 829-832 (1997).

[10] G. S. Pan, R. Kesavamoorthy, and S. A. Asher, Phys. Rev. Lett. **78**, 3860-3863 (1997).

[11] Y. A. Vlasov, X. Z. Bo, J. C. Sturm, and D. J. Norris, Nature (London) **414**, 289-293 (2001).

[12] P. Jiang, J. F. Bertone, K. S. Hwang, and V. L. Colvin, Chem. Mater. **11**, 2132-2140 (1999).

[13] A. P. Gast and W. B. Russel, Phys. Today **51**, 24-30 (1998).

[14] R. Piazza, T. Bellini, and V. Degiorgio, Phys. Rev. Lett. **71**, 4267-4270 (1993).

[15] H. J. Wu, T. O. Pangburn, R. E. Beckham, and M. A. Bevan, Langmuir **21**, 9879-9888 (2005).

[16] S. Hachisu and K. Takano, Adv. Colloid Interface Sci. **16**, 233-252 (1982).

[17] A. V. Petukhov, I. P. Dolbnya, D. G. A. L. Aarts, and G. J. Vroege, Phys. Rev. E **69**, 031405 1-10 (2004).

[18] B. J. Ackerson, S. E. Paulin, and B. Johnson, Phys. Rev. E **59**, 6903-6913 (1999).

[19] C. P. Royall, R. v. Roij, and A. v. Blaaderen, J. Phys.: Condens. Matter **17**, 2315-2326 (2005).

[20] T. Biben and J. P. Hansen, J. Phys.: Condens. Matter **6**, A345-A349 (1994).

[21] W. Stöber, A. Fink, and E. Bohn, J. Colloid Interf. Sci. **26**, 62-69 (1968).

[22] G. H. Bogush, M. A. Tracy, and C. F. Zukoski, J. Non-cryst. Solids **104**, 95-106 (1988).

[23] A. v. Blaaderen and A. Vrij, J. Colloid Interf. Sci. **156**, 1-18 (1993).

[24] A. v. Blaaderen and A. Vrij, Langmuir **8**, 2921-2931 (1992).

[25] A. W. Dearing and E. E. Reid, J. Am. Chem. Soc. **50**, 3058-3062 (1928).

[26] H. Giesche, J. Eur. Ceram. Soc. **14**, 205-214 (1994).

[27] L. L. Hench and J. K. West, Chem. Rev. **90**, 33-72 (1990).

[28] H. Giesche, J. Eur. Ceram. Soc. **14**, 189-204 (1994).

[29] E. J. A. Pope and J. D. Mackenzie, J. Non-cryst. Solids **87**, 185-198 (1986).

[30] K. A. Vorotilov, E. V. Orlova, and V. I. Petrovsky, Thin Solid Films **209**, 188-194 (1992).

[31] B. Karmakar, G. De, D. Kundu, and D. Ganguli, J. Non-cryst. Solids **135**, 29-36 (1991).

[32] H. J. Quenzer, C. Dell, and B. Wagner, Proc. IEEE Micr. Elect. **9**, 272-276 (1996).

[33] M. J. A. d. Dood, B. Berkhout, C. M. v. Kats, A. Polman, and A. v. Blaaderen, Chem. Mater. **14**, 2849-2853 (2002).

[34] G. De, B. Karmakar, and D. Ganguli, J. Mater. Chem. **10**, 2289-2293 (2000).

[35] L. M. Qi, J. M. Ma, H. M. Cheng, and Z. G. Zhao, Chem. Mater. **10**, 1623-1626 (1998).

[36] K. Lee, J. L. Look, M. T. Harris, and A. V. McCormick, J. Colloid Interf. Sci. **194**, 78-88 (1997).

[37] S. A. Khan, A. Gunther, M. A. Schmidt, and K. F. Jensen, Langmuir **20**, 8604-8611 (2004).

[38] C. Graf, D. L. J. Vossen, A. Imhof, and A. v. Blaaderen, Langmuir **19**, 6693-6700 (2003).

[39] R. Lindberg, J. Sjoblom, and G. Sundholm, Colloid. Surface. A **99**, 79-88 (1995).

[40] C. G. Tan, B. D. Bowen, and N. Epstein, J. Colloid Interf. Sci. **118**, 290-293 (1987).

[41] A. v. Blaaderen, J. v. Geest, and A. Vrij, J. Colloid Interf. Sci. **154**, 481-501 (1992).

[42] M. H. Lee, F. L. Beyer, and E. M. Furst, J. Colloid Interf. Sci. **288**, 114-123 (2005).

[43] H. Nishimori, M. Tatsumisago, and T. Minami, J. Sol-Gel Sci. Techn. **9**, 25-31 (1997).

[44] H. J. Zhang, J. Wu, L. P. Zhou, D. Y. Zhang, and L. M. Qi, Langmuir **23**, 1107-1113 (2007).

[45] C. Oh, Y. G. Lee, J. H. Park, and S. G. Oh, Colloid. Surface. A **269**, 112-118 (2005).

[46] J. Esquena, R. Pons, N. Azemar, and J. Caelles, Colloid. Surface. A **123**, 575-586 (1997).

[47] J. H. Park, C. Oh, S. I. Shin, S. K. Moon, and S. G. Oh, J. Colloid Interf. Sci. **266**, 107-114 (2003).

[48] C. Oh, S. C. Chung, S. I. Shin, Y. C. Kim, S. S. Im, and S. G. Oh, J. Colloid Interf. Sci. **254**, 79-86 (2002).

[49] L. M. Rossi, L. F. Shi, F. H. Quina, and Z. Rosenzweig, Langmuir **21**, 4277-4280 (2005).

[50] N. A. M. Verhaegh and A. v. Blaaderen, Langmuir **10**, 1427-1438 (1994).

[51] A. P. Philipse, C. Smits, and A. Vrij, J. Colloid Interf. Sci. **129**, 335-352 (1989).

[52] A. K. v. Helden, J. W. Jansen, and A. Vrij, J. Colloid Interf. Sci. **81**, 354-368 (1981).

[53] C. Smits, J. S. Vanduijneveldt, J. K. G. Dhont, H. N. W. Lekkerkerker, and W. J. Briels, Phase Transit. **21**, 157-170 (1990).

[54] A. P. Philipse and A. Vrij, J. Colloid Interf. Sci. **128**, 121-136 (1989).

[55] H. Choi and I. W. Chen, J. Colloid Interf. Sci. **258**, 435-437 (2003).

[56] R. D. Badley, W. T. Ford, F. J. McEnroe, and R. A. Assink, Langmuir **6**, 792-801 (1990).

[57] H. A. Ketelson, M. A. Brook, and R. H. Pelton, Polym. Advan. Technol. **6**, 335-344 (1995).

[58] C. Pathmamanoharan, Colloid. Surface. **50**, 1-6 (1990).

[59] K. Yoshinaga, K. Fujiwara, E. Mouri, M. Ishii, and H. Nakamura, Langmuir **21**, 4471-4477 (2005).

[60] J. R. Weeks, J. S. v. Duijneveldt, and B. Vincent, J. Phys.: Condens. Matter **12**, 9599-9606 (2000).

[61] J. M. McMahon and S. R. Emory, Langmuir **23**, 1414-1418 (2007).

[62] H. Dehek and A. Vrij, J. Colloid Interf. Sci. **79**, 289-294 (1981).

[63] C. Pathmamanoharan, Colloid. Surface. **34**, 81-88 (1988).

[64] W. N. Everett, R. E. Beckham, K. Meissner, and M. A. Bevan, Langmuir **23**, 8950-8956 (2007).

[65] C. Graf, S. Dembski, A. Hofmann, and E. Ruhl, Langmuir **22**, 5604-5610 (2006).

[66] Y. Chan, J. P. Zimmer, M. Stroh, J. S. Steckel, R. K. Jain, and M. G. Bawendi, Adv. Mater. **16**, 2092-2097 (2004).

[67] W. C. W. Chan and S. M. Nie, Science **281**, 2016-2018 (1998).

[68] A. R. Clapp, E. R. Goldman, and H. Mattoussi, Nature Protocols **1**, 1258-1266 (2006).

[69] M. Zhou and I. Ghosh, Peptide Sci. **88**, 325-339 (2006).

[70] S. Roux, B. Garcia, J. Bridot, M. Salome, C. Marquette, L. Lemelle, P. Gillet, L. Blum, P. Perriat, and O. Tillement, Langmuir **21**, 2526-2536 (2005).

[71] S. Jaffar, K. T. Nam, A. Khademhosseini, J. Xing, R. S. Langer, and A. M. Belcher, Nano Lett. **4**, 1421-1425 (2004).

[72] Y. S. Liu, Y. H. Sun, P. T. Vernier, C. H. Liang, S. Y. C. Chong, and M. A. Gundersen, J. Phys. Chem. C **111**, 2872-2878 (2007).

[73] M. Bradley, N. Bruno, and B. Vincent, Langmuir **21**, 2750-2753 (2005).

[74] N. Joumaa, M. Lansalot, A. Theretz, and A. Elaissari, Langmuir **22**, 1810-1816 (2006).

[75] X. Gao and S. Nie, J. Phys. Chem. B **107**, 11575-11578 (2003).

[76] Invitrogen, *online catalog > product details succinimidyl 6-(N-(7-nitrobenz-2-oxa-1,3-diazol-4-yl)amino)hexanoate (NBD-X, SE) Catalog Number - S-1167*, https://catalog.invitrogen.com/index.cfm?fuseaction=viewCatalog.viewProductDetails&productDescription=3368 (2007)

[77] A. D. McFarland, C. L. Haynes, R. P. Mirkin, R. P. v. Duyne, and H. A. Godwing, J. Chem. Educ. **81**, 544A-544B (2004).

[78] Z. A. Peng and X. G. Peng, J. Am. Chem. Soc. **123**, 183-184 (2001).

[79] D. V. Talapin, A. L. Rogach, A. Kornowski, M. Haase, and H. Weller, Nano Letters **1**, 207-211 (2001).

[80] B. Alberts, A. Johnson, J. Lewis, M. Raff, K. Roberts, and P. Walter, *Molecular Biology of the Cell* (Garland Science, New York, 2002).

[81] S. Coenen and C. G. Dekruif, J. Colloid Interf. Sci. **124**, 104-110 (1988).

[82] D. D. Perrin, *Dissociation Constants of Organic Bases in Aqueous Solution* (Butterworths, London, 1965).

[83] K. Masaki, H. Ayako, and H. Hideki, J. Adhes. Soc. Jpn. **41**, 54-59 (2005).

[84] S. T. Selvan, C. Bullen, M. Ashokkumar, and P. Mulvaney, Adv. Mater. **13**, 985-988 (2001).

[85] J. C. Crocker and D. G. Grier, J. Colloid Interf. Sci. **179**, 298-310 (1996).

[86] M. C. Jenkins and S. U. Egelhaaf, Adv. Colloid Interface Sci. **136**, 65-92 (2008).

[87] J. B. Pawley, *Handbook of Biological Confocal Microscopy* (Springer Science+Business Media, LLC, Singapore, 2006).

[88] M. K. Cheezum, W. F. Walker, and W. H. Guildford, Biophys. J. **81**, 2378-2388 (2001).

[89] J. P. Hoogenboom, P. Vergeer, and A. v. Blaaderen, J. Chem. Phys. **119**, 3371-3383 (2003).

[90] M. S. Nixon and A. S. Aquado, *Feature Extraction and Image Processing* (Newnes, Woburn, MA, 2002).

[91] R. C. Gonzalez and R. E. Woods, *Digital Image Processing* (Prentice-Hall, Upper Saddle River, NJ, 2007).

[92] E. Kreyszig, *Advanced Engineering Mathematics* (John Wiley & Sons, Inc., New York, 1999).

[93] W. H. Press, S. A. Teukolsky, W. T. Vetterling, and B. P. Flannery, *Numerical Recipes in FORTRAN 77: The Art of Scientific Computing* (Press Syndicate of the University of Cambridge, Cambridge, UK, 2001).

[94] W. B. Russel, D. A. Saville, and W. R. Schowalter, *Colloidal Dispersions* (Cambridge University Press, New York, 1989).

[95] A. P. Gast, C. K. Hall, and W. B. Russel, J. Colloid Interf. Sci. **96**, 251-267 (1983).

[96] N. F. Carnahan and K. E. Starling, J. Chem. Phys. **51**, 635-636 (1969).

[97] K. R. Hall, J. Chem. Phys. **57**, 2252-2254 (1972).

[98] L. Verlet and J. J. Weis, Phys. Rev. A **5**, 939-952 (1972).

[99] J. M. Kincaid and J. J. Weis, Mol. Phys. **34**, 931-938 (1977).

[100] N. F. Carnahan and K. E. Starling, J. Chem. Phys. **53**, 600-603 (1970).

[101] D. Henderson, Mol. Phys. **34**, 301-315 (1977).

[102] C. McBride and C. Vega, J. Chem. Phys. **116**, 1757-1759 (2002).

[103] A. Huerta, D. Henderson, and A. Trokhymchuk, Phys. Rev. E **74**, 061106 1-4 (2006).

[104] A. C. Mitus, H. Weber, and D. Marx, Phys. Rev. E **55**, 6855-6859 (1997).

[105] J. W. Tester and M. Modell, *Thermodynamics and Its Applications* (Prentice Hall PTR, Upper Saddle River, NJ, 1996).

[106] D. A. McQuarrie, *Statistical Mechanics* (University Science Books, Sausalito, CA, 2000).

[107] T. L. Hill, *An Introduction to Statistical Thermodynamics* (Addison-Wesley, Reading, MA, 1962).

[108] J. R. Savage, D. W. Blair, A. J. Levine, R. A. Guyer, and A. D. Dinsmore, Science **314**, 795-798 (2006).

[109] J. Perrin, J. Phys. (Paris) **9**, 5-39 (1910).

[110] J. Perrin, *Atoms* (D. van Nostrand Company, New York, 1916).

[111] A. v. Blaaderen, R. Ruel, and P. Wiltzius, Nature (London) **385**, 321-324 (1997).

[112] W. Lee, A. Chan, M. A. Bevan, J. A. Lewis, and P. V. Braun, Langmuir **20**, 5262-5270 (2004).

[113] H. J. Wu and M. A. Bevan, Langmuir **21**, 1244-1254 (2005).

[114] A. Vrij, J. Chem. Phys. **72**, 3735-3739 (1980).

[115] A. Jamnik, J. Chem. Phys. **109**, 11085-11093 (1998).

[116] N. Choudhury and S. K. Ghosh, J. Chem. Phys. **116**, 384-391 (2002).

[117] S. V. Savenko and M. Dijkstra, Phys. Rev. E **70**, 051401 1-7 (2004).

[118] T. Biben, J. P. Hansen, and J. L. Barrat, J. Chem. Phys. **98**, 7330-7344 (1993).

[119] M. Schmidt, M. Dijkstra, and J. P. Hansen, J. Phys.: Condens. Matter **16**, S4185-S4194 (2004).

[120] R. S. Saksena and L. V. Woodcock, J. Chem. Phys. **122**, 164501 1-9 (2005).

[121] T. Biben, R. Ohnesorge, and H. Lowen, Europhys. Lett. **28**, 665-670 (1994).

[122] T. Biben and J. P. Hansen, J. Phys.: Condens. Matter **6**, A345-A349 (1994).

[123] L. Belloni, J. Chem. Phys. **123**, 204705 1-12 (2005).

[124] A. Torres, A. Cuetos, M. Dijkstra, and R. v. Roij, Phys. Rev. E **75**, 041405 1-8 (2007).

[125] N. Johnston and L. G. Howell, Phys. Rev. **35**, 274-282 (1930).

[126] C. M. McDowell and F. L. Usher, Proc. R. Soc. London A **138**, 133-146 (1932).

[127] S. Hachisu and K. Takano, Adv. Colloid Interfac. **16**, 233-252 (1982).

[128] R. Piazza, T. Bellini, and V. Degiorgio, Phys. Rev. Lett. **71**, 4267-4270 (1993).

[129] M. A. Rutgers, J. H. Dunsmuir, J. Z. Xue, W. B. Russel, and P. M. Chaikin, Phys. Rev. B **53**, 5043-5046 (1996).

[130] C. P. Royall, R. v. Roij, and A. v. Blaaderen, J. Phys.: Condens. Matter **17**, 2315-2326 (2005).

[131] R. S. Crandall and R. Williams, Science **198**, 293-295 (1977).

[132] D. v. d. Beek, T. Schilling, and H. N. W. Lekkerkerker, J. Chem. Phys. **121**, 5423-5426 (2004).

[133] A. P. Philipse and G. H. Koenderink, Adv. Colloid Interfac. **100**, 613-639 (2003).

[134] M. Rasa and A. P. Philipse, Nature **429**, 857-860 (2004).

[135] J. A. Barker and D. Henderson, J. Chem. Phys. **47**, 4714-4721 (1967).

[136] M. P. Allen and D. J. Tildesley, *Computer Simulation of Liquids* (Oxford Science, New York, 1987).

[137] P. S. Nikam and S. J. Kharat, J. Chem. Eng. Data **50**, 455-459 (2005).

[138] A. Mori, S. Yanagiya, Y. Suzuki, T. Sawada, and K. Ito, J. Chem. Phys. **124**, 174507 1-10 (2006).

[139] B. I. Halperin and D. R. Nelson, Phys. Rev. Lett. **41**, 121-124 (1978).

[140] D. J. Courtemanche and F. v. Swol, Phys. Rev. Lett. **69**, 2078-2081 (1992).

[141] D. G. A. L. Aarts, M. Schmidt, and H. N. W. Lekkerkerker, Science **304**, 847-850 (2004).

[142] I. D. Morrison, Coll. Surf. A **71**, 1-37 (1993).

[143] H. C. Andersen, J. D. Weeks, and D. Chandler, Phys. Rev. A **4**, 1597-1607 (1971).

[144] S. G. J. M. Kluijtmans, E. H. A. d. Hoog, and A. P. Philipse, J. Chem. Phys. **108**, 7469-7477 (1998).

[145] W. H. Briscoe and R. G. Horn, Lagmuir **18**, 3945-3956 (2002).

[146] T. M. Truskett, S. Torquato, S. Sastry, P. G. Debenedetti, and F. H. Stillinger, Phys. Rev. E **58**, 3083-3088 (1998).

[147] A. C. Mitus, H. Weber, and D. Marx, Phys. Rev. E **55**, 6855-6859 (1997).

[148] M. Parrinello and A. Rahman, Phys. Rev. Lett. **45**, 1196-1199 (1980).

[149] S. E. Phan, W. B. Russel, J. Zhu, and P. M. Chaikin, J. Chem. Phys. **108**, 9789-9795 (1998).

[150] S. Auer and D. Frenkel, Nature **413**, 711-713 (2001).

[151] D. H. v. Winkle and C. A. Murray, J. Chem. Phys. **89**, 3885-3891 (1988).

[152] N. A. M. Verhaegh, J. S. v. Duijneveldt, A. v. Blaaderen, and H. N. W. Lekkerkerker, J. Chem. Phys. **102**, 1416-1421 (1995).

[153] J. P. Hoogenboom, D. Derks, P. Vergeer, and A. v. Blaaderen, J. Chem. Phys. **117**, 11320-11328 (2002).

[154] R. L. Davidchack and B. B. Laird, J. Chem. Phys. **108**, 9452-9462 (1998).

[155] A. P. Gast and Y. Monovoukas, Nature **351**, 553-555 (1991).

[156] J. P. Hansen and L. Verlet, Phys. Rev. **184**, 151-161 (1969).

[157] F. A. Lindemann, Z. Phys **11**, 609-612 (1910).

[158] T. V. Ramakrishnan and M. Yussouff, Phys. Rev. B **19**, 2775-2794 (1979).

[159] C. Chakravartya, P. G. Debenedetti, and F. H. Stillinger, J. Chem. Phys. **126**, 204508 1-10 (2007).

[160] M. A. Bevan, J. A. Lewis, P. V. Braun, and P. Wiltzius, Langmuir **20**, 7045-7052 (2004).

[161] W. K. Kegel and J. K. G. Dhont, J. Chem. Phys. **112**, 3431-3436 (2000).

[162] G. Medeiros-Ribeiro, A. M. Bratkovski, T. I. Kamins, D. A. A. Ohlberg, and R. S. Williams, Science **279**, 353-355 (1998).

[163] K. H. Lin, J. C. Crocker, V. Prasad, A. Schofield, D. A. Weitz, T. C. Lubensky, and A. G. Yodh, Phys. Rev. Lett. **85**, 1770-1773 (2000).

[164] D. W. M. Marr and A. P. Gast, Phys. Rev. E **53**, 4058-4062 (1995).

[165] K. E. Davis, W. B. Russel, and W. J. Glantschnig, Science **245**, 507-510 (1989).

[166] J. Zhu, M. Li, R. Rogers, W. Meyer, R. H. Ottewill, S. S. Crew, W. B. Russel, and P. M. Chaikin, Nature **387**, 883-885 (1997).

[167] A. D. Dinsmore and A. G. Yodh, Langmuir **15**, 314-316 (1999).

[168] A. D. Dinsmore, A. G. Yodh, and D. J. Pine, Phys. Rev. E **52**, 4045-4047 (1995).

[169] P. D. Kaplan, J. L. Rouke, and A. G. Yodh, Phys. Rev. Lett. **72**, 582-585 (1994).

[170] W. J. Hunt and C. F. Zukoski, J. Colloid Interf. Sci. **210**, 332-342 (1999).

[171] W. J. Hunt and C. F. Zukoski, J. Colloid Interf. Sci. **210**, 343-351 (1999).

[172] E. K. Hobbie, Phys. Rev. E **55**, 6281-6284 (1997).

[173] E. K. Hobbie, Phys. Rev. Lett. **81**, 3996-3999 (1998).

[174] E. K. Hobbie, Langmuir **15**, 8807-8812 (1999).

[175] E. K. Hobbie and M. J. Holter, J. Chem. Phys. **108**, 2618-2621 (1998).

[176] E. K. Hobbie and A. D. Stewart, Phys. Rev. E **61**, 5540-5544 (2000).

[177] A. D. Dinsmore, P. B. Warren, W. C. K. Poon, and A. G. Yodh, Europhys. Lett. **40**, 337-342 (1997).

[178] A. D. Dinsmore, A. G. Yodh, and D. J. Pine, Nature (London) **383**, 239-242 (1996).

[179] V. J. Anderson, E. H. A. d. Hoog, and H. N. W. Lekkerkerker, Phys. Rev. E **65**, 011403 1-8 (2001).

[180] E. H. A. de Hoog, W. K. Kegel, A. v. Blaaderen, and H. N. W. Lekkerkerker, Phys. Rev. E **64**, 021407 1-9 (2001).

[181] P. N. Pusey, A. D. Pirie, and W. C. K. Poon, Physica A **201**, 322-331 (1993).

[182] N. A. M. Verhaegh, D. Asnaghi, and H. N. W. Lekkerkerker, Physica A **264**, 64-74 (1999).

[183] X. Xian, A. V. Petukhov, M. M. E. Snel, I. P. Dolbnya, D. G. A. L. Aarts, G. J. Vroege, and H. N. W. Lekkerkerker, J. Appl. Crystallogr. **36**, 597-601 (2003).

[184] D. G. A. L. Aarts, R. Tuinier, and H. N. W. Lekkerkerker, J. Phys.: Condens. Matter **14**, 7551-7561 (2002).

[185] E. H. A. d. Hoog, L. I. D. J. V. Steensel, M. M. E. Snel, J. P. J. M. v. d. Eerden, and H. N. W. Lekkerkerker, Langmuir **17**, 5486-5490 (2001).

[186] C. Smits, B. v. d. Most, J. K. G. Dhont, and H. N. W. Lekkerkerker, Adv. Colloid Interface Sci. **42**, 33-40 (1992).

[187] N. A. M. Verhaegh, D. Asnaghi, H. N. W. Lekkerkerker, M. Giglio, and L. Cipelletti, Physica A **242**, 104-118 (1997).

[188] S. A. Shah, Y. L. Chen, S. Ramakrishnan, K. S. Schweizer, and C. F. Zukoski, J. Phys.: Condens. Matter **15**, 4751-4778 (2003).

[189] V. Gopalakrishnan, K. S. Schweizer, and C. F. Zukoski, J. Phys.: Condens. Matter **18**, 11531-11550 (2006).

[190] V. Gopalakrishnan, S. A. Shah, and C. F. Zukoski, J. Rheol. **49**, 383-400 (2005).

[191] V. Gopalakrishnan and C. F. Zukoski, J. Rheol. **48**, 1321-1344 (2004).

[192] S. A. Shah, S. Ramakrishnan, I. W. Chen, K. S. Schweizer, and C. F. Zukoski, Langmuir **19**, 5128-5136 (2003).

[193] S. A. Shah, Y. L. Chen, K. S. Schweizer, and C. F. Zukoski, J. Chem. Phys. **118**, 3350-3361 (2003).

[194] S. Ramakrishnan, M. Fuchs, K. S. Schweizer, and C. F. Zukoski, Langmuir **18**, 1082-1090 (2002).

[195] B. Cui, B. Lin, D. Frydel, and S. A. Rice, Phys. Rev. E **72**, 021402 1-7 (2005).

[196] B. Cui, B. Lin, and S. A. Rice, J. Chem. Phys. **119**, 2386-2398 (2003).

[197] H. M. Ho, B. Cui, S. Repel, B. Lin, and S. A. Rice, J. Chem. Phys. **121**, 8627-8634 (2004).

[198] B. X. Cui, B. H. Lin, and S. A. Rice, J. Chem. Phys. **114**, 9142-9155 (2001).

[199] R. M. Amos, J. G. Rarity, P. R. Tapster, T. J. Shepherd, and S. C. Kitson, Phys. Rev. E **61**, 2929-2935 (2000).

[200] O. Vickreva, O. Kalinina, and E. Kumacheva, Adv. Mater. **12**, 110-112 (2000).

[201] P. T. Korda and D. G. Grier, J. Chem. Phys. **114**, 7570-7573 (2001).

[202] M. Harada, M. Ishii, and H. Nakamura, Colloid. Surface. B **56**, 220-223 (2007).

[203] A. Seidel, *Kirk-Othmer Encyclopedia of Chemical Technology, Vol. 15* (John Wiley & Sons, Inc., Hoboken, NJ, 2007).

[204] T. H. Kim and C. H. Jeong, J. Korean Ind. Eng. Chem. **8**, 425-429 (1997).

VITA

Name:	Richard Edward Beckham
Address:	Los Alamos National Laboratory Hydrology, Geochemistry, and Geology Group, EES-6 Mail Stop J514 Los Alamos, NM 87545, USA
Email Address:	richard.beckham@chemail.tamu.edu
Education:	B.S., Chemical Engineering, North Carolina State University, 1997 M.S., Chemical Engineering, Northeastern University, 2003